NASA Contractor Report 4066

Aerodynamic Analysis for Aircraft With Nacelles, Pylons, and Winglets at Transonic Speeds

Charles W. Boppe

CONTRACT NAS1-14732
APRIL 1987

NASA Contractor Report 4066

Aerodynamic Analysis for Aircraft With Nacelles, Pylons, and Winglets at Transonic Speeds

Charles W. Boppe
Grumman Aerospace Corporation
Bethpage, New York

Prepared for
Langley Research Center
under Contract NAS1-14732

National Aeronautics
and Space Administration

**Scientific and Technical
Information Branch**

1987

CONTENTS

ILLUSTRATIONS

ILLUSTRATIONS (cont'd.)

ILLUSTRATIONS (cont'd.)

SUMMARY

A computational method has been developed to provide an analysis for complex realistic aircraft configurations at transonic speeds. Wing-fuselage configurations with various combinations of pods, pylons, nacelles, and winglets can be analyzed along with simpler shapes such as airfoils, isolated wings, and isolated bodies. The flexibility required for the treatment of such diverse geometries is obtained by using a multiple nested grid approach in the finite difference relaxation scheme. Aircraft components (and their grid systems) can be added or removed as required. As a result, the computational method can be used in the same manner as a wind tunnel to study high-speed aerodynamic interference effects. The multiple grid approach also provides high boundary point density/cost ratio. High resolution pressure distributions can be obtained. Computed results are correlated with wind tunnel and flight data using four different transport configurations. Experimental/computational component interference effects are included for cases where data is available. The computer code used for these comparisons is described in the appendixes of this report.

INTRODUCTION

There has been a dramatic growth in the development of transonic computational methods during the past ten year period. This growth is stimulated by the important role that high-speed non-linear methods now play in the detailed aircraft aerodynamic design process. Many advances have been related to improvements in computing efficiency. In addition, the ability to treat complex geometric shapes has steadily improved. Murman and Cole[1], Bailey and Steger[2], Keller and South[3], and Jameson and Caughey[4] have made important contributions to this evolutionary process. The primary goal of these efforts is the development of tools for solving practical aircraft design and analysis problems.

The first analysis schemes were applied to simple 2-D airfoil shapes and axisymmetric bodies (see Fig. 1). Soon after this, isolated wing methods evolved. Computations were performed on simple wing-body shapes during the mid-1970's period. By 1980, aircraft configurations with various combinations of nacelles, pylons, and winglets[5] could be analyzed.

Two different approaches have been implemented in the past. The first, and simplest, employs a small disturbance-type flow equation coupled with mean-surface boundary conditions. In time, it was noted that the classical transonic small disturbance equation was not well suited to the analysis of swept wing flows. The proper shock strength and the velocity at which the flow equation changes type is not inherent in the equation when shock waves have appreciable sweep. For this reason, today's small disturbance formulations typically incorporate a modified or extended small disturbance flow equation. The second, and more sophisticated approach, employs the full potential equation (or Euler's equations) coupled with surface-conforming boundary conditions. This approach is complicated, not so much by the use of the more complete flow equation, but rather by the difficulties associated with the

application of exact boundary conditions. As configurations become more complex, it becomes difficult to construct a suitable coordinate system. As a result, the availability of full potential equation methods has lagged that of the small disturbance methods by several years.

Until recently, small disturbance and full potential equation methods were constructed about a single continuous grid system. This approach provides a smooth transition from the near to the far field regions when proper stretching functions are used, but for a case as simple as a wing-body combination, where axial grid point resolution must be high for the body and spanwise resolution must be high for the wing, problems arise. Problems are caused by time and core storage restrictions of current computers and inefficiency of the combined axial/spanwise grid system which stretches into the far field where it is not required. Transonic wing-body analysis codes with single continuous grid systems exhibit poor resolution on either the body or the wing because these surfaces are not aligned. These difficulties can be overcome by not implementing the traditional single grid approach.

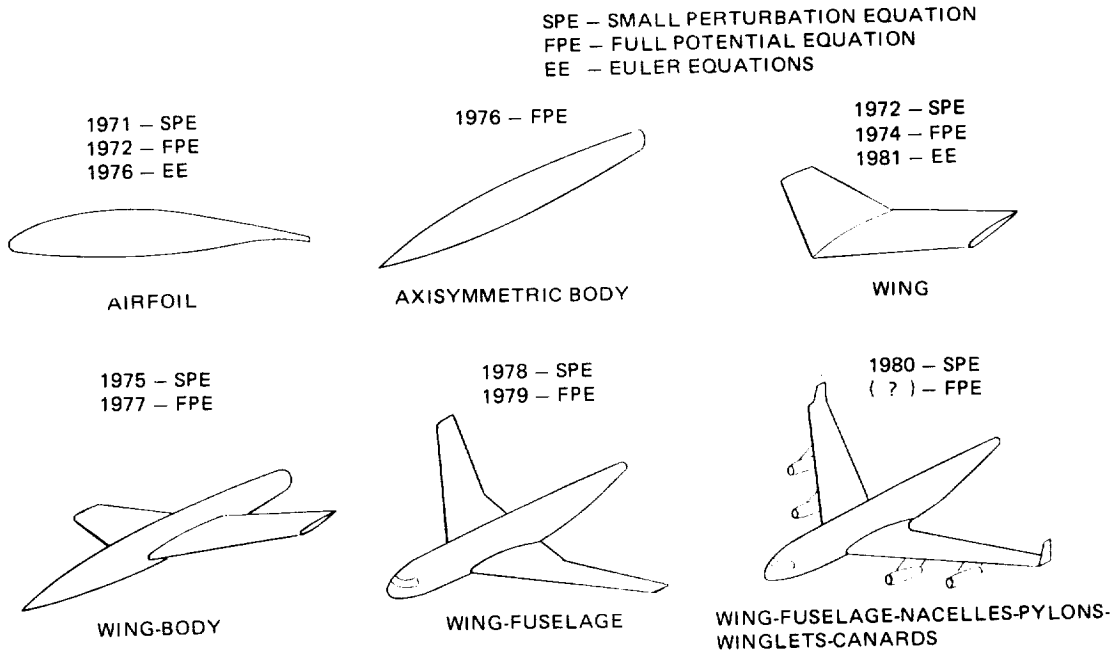

Figure 1 Growth in Geometric Complexity for Transonic Flow Simulations

Grid orthogonality presents another problem for "exact" boundary condition formulations. Boundary/grid orthogonality is easy to achieve for simple 2-D and 3-D shapes, but for complex shapes such as a wing-nacelle-pylon arrangement, it may be physically impossible to achieve an orthogonal grid for all surfaces simultaneously. This often results in a lack of orthogonality at the critical pylon-nacelle station. This could, depending on the severity of the flow condition and the geometric shape, produce a jump in the metric across the pylon-nacelle span line. The resulting "numerical" interference effect might be interpreted as an "aerodynamic" interference effect during applications. This also suggests, then, a re-evaluation the conventional single grid approach.

When configurations are examined by wind tunnel testing, various components such as pods, pylons and winglets are removed and reattached to evaluate aerodynamic interference effects. If a three-dimensional computational method is developed using the single grid approach, it will be necessary to find a different coordinate mapping for each configuration modification. Perhaps a separate computer code would be required for each geometric shape involved. The configurations boundary points, mesh resolution, and ultimately, the computed flow field would vary with each change to the coordinate system. This problem is minimized if multiple grid systems are used. A single computer code can be used for the analysis of isolated bodies, isolated wings, and wing-fuselage configurations with nacelles and additional lifting surfaces. Boundary surfaces, along with their embedded mesh systems, can be added or removed for analysis much in the same manner as wind tunnel model parts during experimentation.

A simple multiple nested grid approach was described in NASA CR-3243 (Reference 6). The simplicity of the grid embedding scheme is stressed because the probability of successfully simulating a transonic flow about a complex configuration will be increased if the methodology is simple. This report describes the extension of the Reference 6 method to include the simultaneous treatment of multiple wing and body surfaces. In particular, the provisions that have been made for the analysis of pods, nacelles, pylons and winglets

are noted. The small disturbance character of the original wing-body method is retained. The mean surface approximation permits the extensive use of rectangular coordinate arrays. This plays an important role in keeping the method simple.

The basic transonic WIng-Body COde (WIBCO) was described in Reference 6. As a result of this effort, a new computer code has evolved (WIBCO-PPW) which in addition to the wing, body and wing-body capabilities of WIBCO, includes the new pod, pylon and winglet analysis capabilities. This report should be used along with Reference 6 since certain elements of the two codes which are common are not repeated herein (i.e., wing viscous effects, arbitrary fuselage modeling, wing, body, wing-body flow simulations).

The WIBCO-PPW Code has been developed for both IBM and CDC type computers.* Comments on usage and features of the NASA CDC version of the code have been included as Appendix B.

* The author would like to thank Dr. Perry Newman for many valuable discussions during this code development effort. In addition, Mrs. Kara Haigler made significant contributions by refining and verifying the NASA CDC version of the code.

NOMENCLATURE

SYMBOLS

b	Wing or winglet span
C,c	Wing or winglet chord
C_D,C_d	Drag coefficient
C_F,C_f	Friction drag coefficient
C_L,C_ℓ	Lift coefficient
C_M,C_m	Moment coefficient
C_p	Pressure coefficient
f	Surface shape function
g	Acceleration due to gravity
L	Pod or nacelle length
M.A.C.	Mean aerodynamic chord of wing
M	Mach number
MFR	Nacelle inlet mass flow ratio
NPR	Nacelle nozzle pressure ratio
N,n	Surface normal
P	Pressure
R,r	Nacelle/pod radius
R	Gas constant
T	Absolute temperature
u,v,w	Velocity components
V	Velocity
X,Y,Z	Cartesian coordinate axes
α	Angle-of-attack
β	Angle-of-yaw
Γ	Circulation
γ	Specific heat ratio (c_p/c_v)
ΔX, ΔY, ΔZ	Mesh spacing in X, Y, and Z directions
$\Delta\xi$, $\Delta\eta$, $\Delta\zeta$	Mesh spacing in ξ, η, and ζ directions
$\Delta\phi$	Change in perturbation potential between iteration cycles
δ^*	Boundary layer displacement thickness
η	Wing or winglet span position (2 y/b)
ξ,η,ζ	Wing skewed coordinate axes
ϕ	Perturbation potential

ψ	Winglet toe-out angle, measured from symmetry plane
Ω	Winglet cant angle, measured from wing plane

Subscripts:

av,AV	Average
Body,B	Body
c	Computational
cold	Cold jet
D	Dummy value
e	Exhaust
FIELD	Field
FRICTION	Friction
g	Geometric
hot	Hot jet
I	Induced
i	Inlet
ib	Inboard
i,j,k	Mesh indices
J	Jet
loc, LOC	Local
MAX	Maximum
O	Total
ob	Outboard
pod,POD	Pod
pyl	Pylon
REF	Reference
S	Static
WAVE	Wave
WING,W	Wing
x,y,z	Partial derivatives with respect to x,y,z
ξ,η,ζ	Partial derivatives with respect to ξ,η,ζ
∞	Infinity

COMPUTATIONAL METHOD

Flow Equation

The classical transonic small-disturbance flow equation written in terms of the disturbance velocity potential has been extended by retaining additional terms found in the full potential equation. These terms make it possible to resolve shock waves with appreciable sweep on wings in the X-Y (wing) plane. The global flow equation is:

$$\left[1 - M_\infty^2 - (\gamma + 1)M_\infty^2 \phi_x - \frac{\gamma + 1}{2} M_\infty^2 \phi_x^2\right]\phi_{xx} - 2M_\infty^2 \phi_y \phi_{xy}$$

$$+ \left[1 - (\gamma - 1)M_\infty^2 \phi_x\right]\phi_{yy} + \phi_{zz} = 0 \qquad (1)$$

This equation is also used in each component embedded grid system. The only exception is the winglet embedded fine mesh system. Wing-tip-mounted vertical winglets may, at certain conditions, exhibit shock waves, swept in the X-Z (winglet) plane. To improve the ability to capture this type of shock wave, the following flow equation is used:

$$\left[1 - M_\infty^2 - (\gamma + 1)M_\infty^2 \phi_x - \frac{\gamma + 1}{2} M_\infty^2 \phi_x^2\right]\phi_{xx} - 2M_\infty^2 \phi_z \phi_{xz}$$

$$+ \left[1 - (\gamma - 1)M_\infty^2 \phi_x\right]\phi_{zz} + \phi_{yy} = 0 \qquad (2)$$

In Equation (2), the X-Y cross-flow terms have been replaced by equivalent X-Z cross-flow terms.

Pylon-type surfaces, in general, are not highly loaded. Shock waves are expected to propagate normally off neighboring components. Since swept pylon shock waves are not expected in most applications, special provisions involving the flow equation have not been made.

Computational Grid Approach

The feature which distinguishes this approach from that of other methods is the use of multiple embedded grid systems. Conventional schemes employ a single continuous computing grid system. The multiple grid approach provides many advantages, if the analysis of complex shapes is the primary concern. Figure 2 illustrates a transport configuration with the aircraft component grid system boundaries included. The entire arrangement is positioned in the center of a global Cartesian coordinate system. The global grid is stretched so that boundaries represent infinity. This grid also serves a second purpose; it provides a means for interactions between the component embedded grid systems. Crude and fine grid systems interact or communicate by using an overlap region wherein the flow is computed twice for each iteration. This procedure is described in Reference 6.

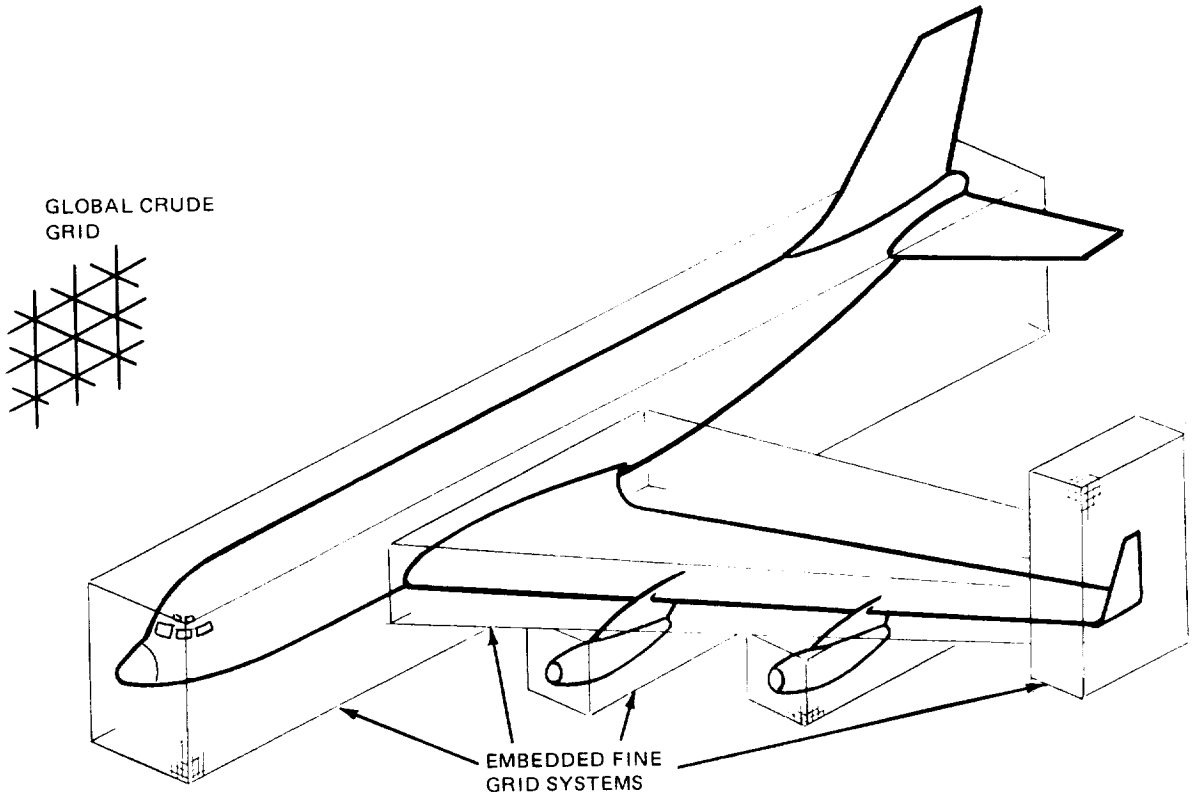

R84-1137-002D

Figure 2 Multiple Grid Approach for Complex Aircraft Flow Simulations

The embedded grid systems provide computational resolution that is much more detailed than that of the surrounding global crude mesh. A detailed analysis is performed only in a region close to the configuration where gradients are high. Ideally, three-dimensional methods should permit grid densities that are higher than two-dimensional and axisymmetric counterparts. This need is generated by the increased complexity of a flow field which has an additional dimension. The present method fulfills this requirement. There are 100 evenly spaced mesh points available in the streamwise direction along fuselage, nacelle and pod surfaces. In addition, wing, pylon and winglet chords are modeled using 100 streamwise points.

Discretization errors at the crude/fine grid interface are a function of both mesh spacing and flow gradient. Fine grid boundaries are positioned sufficiently far from the boundary surface to insure that these errors are small. Numerical experiments were used to "set" grid interface boundaries.

Pod and Engine Nacelle Surfaces

The conventional technique generally applied to body or fuselage shapes was initially used for simulating pod and nacelle surfaces. This required that a computational surface representing the nacelle extend from upstream to downstream infinity. Nacelle boundary conditions were applied along the length of tube starting at the inlet face and ending at the exhaust exit. Computations indicated that this approach would not be satisfactory. It is suspected that the problem is related to the difference between the physical and computational streamtube surfaces (Figure 3). The difficulty is compounded since these streamtubes typically pass very close to wing or body surfaces. Physical streamtubes are deflected by wing upwash/downwash fields. In addition, they are contoured by inlet mass flow ratio and exhaust pressure ratio effects. The computational streamtube is constrained to lie along existing grid lines. These tubes may be contoured by appropriate slope-type boundary conditions, but the physical position at which the boundary condition is applied is still constrained to lie on the computational grid surface. This erroneous streamtube interference problem increases as wing-nacelle separation decreases. As might

be expected, the problem is more severe when streamtubes pass over a lifting wing at transonic conditions than it is when streamtubes pass below the wing.

Exact position of inlet and exhaust streamtubes is difficult to determine. If position was known, or if it could be calculated with confidence, it could not be modeled easily. The best solution to this problem might be to eliminate the streamtube completely. Appropriate flow field potentials can be assigned to inlet and exhaust surfaces based on the inlet mass flow ratio and nozzle pressure ratio. The flow will then develop naturally in front of and behind the nacelle. This scheme should then also be suitable for modeling a pod or closed store which does not generate inlet or exhaust streamtubes.

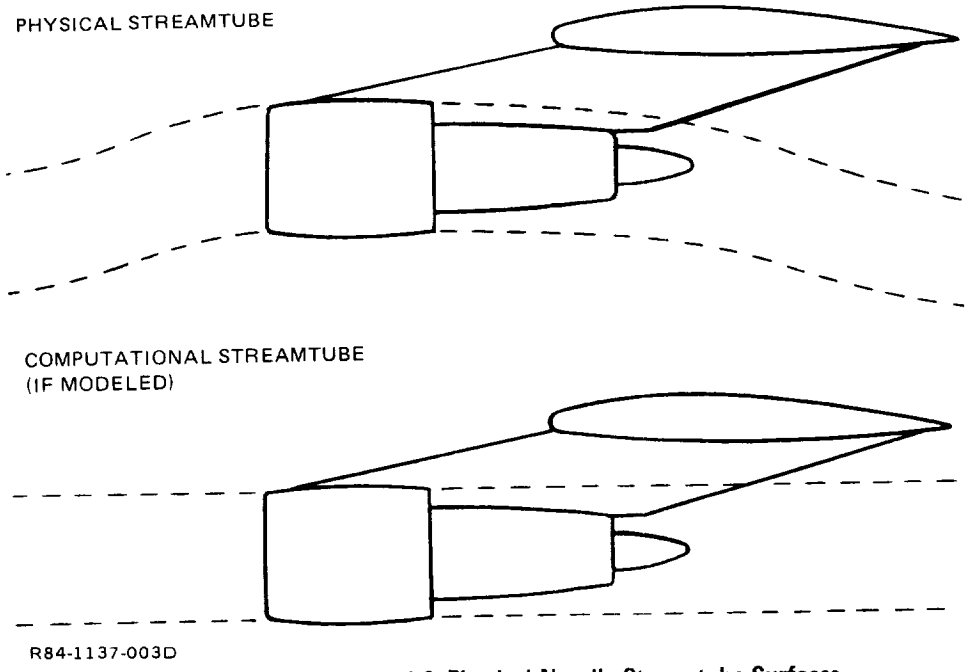

Figure 3 Computational & Physical Nacelle Streamtube Surfaces

Figure 4 illustrates crude and embedded fine grid arrangement for a typical nacelle or pod surface. Two operational modes are available: if nacelle or pod interference or nearby wing and fuselage surfaces is the primary concern, the crude grid representation is sufficient; if details of pressures on the nacelle surface are required, the fine grid solution can be obtained.

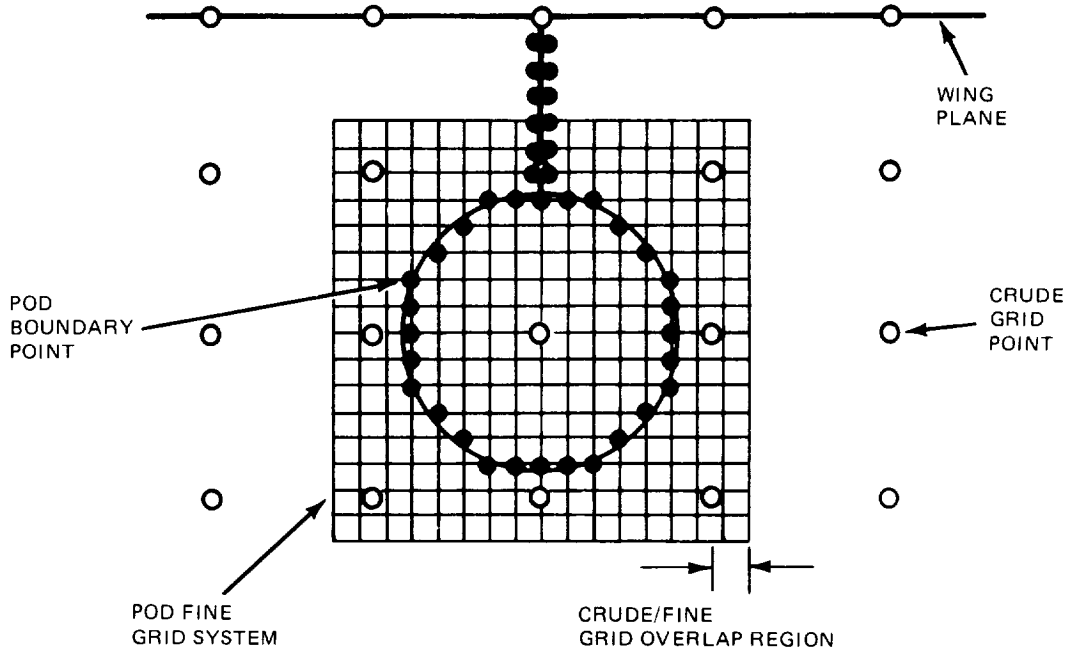

Figure 4 Crude/Fine Grid Arrangement for Pods & Nacelles

Computations indicate that a four-point diamond pattern provides the best approximation of the pod surface in the crude grid system. Grid points above and below and to the left and right of the pod center point make up this pattern. Note that this "best" flow simulation pattern may not be the same for other computational methods, because it depends on both the Y and Z mesh spacing used and the typical size of aircraft nacelles. Approximately 10 to 20 mesh points fall along the nacelle in the axial direction. The actual number depends on the length of the nacelle relative to other aircraft dimensions.

Approximately 28 mesh points represent the nacelle at each axial station if the embedded grid system is used. One hundred evenly spaced points fall between inlet and exhaust surfaces. The embedded fine grid interacts with the global crude grid in the same manner as the wing and fuselage grid systems. This requires a grid overlap region (Figure 4). Crude grid flow field potentials are interpolated (linearly) to determine fine grid boundary potentials around the fine grid perimeter. Note that this perimeter also represents the outer boundary of the overlap region. The fine grid system is then relaxed to

determine the detailed flow between the outer boundary and nacelle surface. Resulting fine grid field potentials are interpolated to update crude grid points which make up the inner boundary of the overlap region. The global crude grid system is then relaxed and the cycle is repeated. The solution process continues by alternately sweeping the fine and crude grid systems until both are satisfactorily converged. Detailed pressure distributions are obtained by differencing fine grid nacelle boundary potentials.

Figure 5 illustrates a typical nacelle boundary point along with field points required for determining boundary potential values. For a nacelle shape defined by:

$$f(X,Y,Z) = 0 \tag{3}$$

the small disturbance boundary condition is:

$$f_x + f_y \phi_y + f_z \phi_z = 0 \tag{4}$$

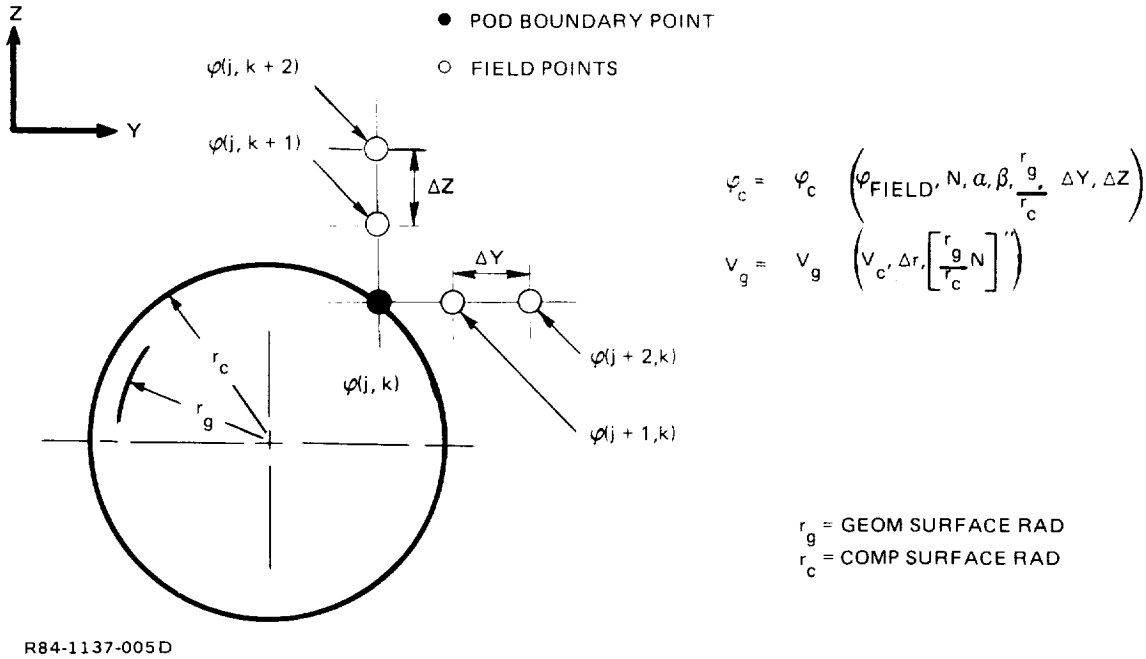

Figure 5 Nacelle & Pod Side Boundary Points

Three-point extrapolated differences are substituted for the velocities in Equation (4). The boundary surface representing the nacelle is constrained to lie along Cartesian grid lines. As a result, there are regions along the nacelle where the computational nacelle surface and the geometric or physical nacelle surface do not coincide. Slender body theory is used to provide a boundary condition correction for both lifting and non-lifting displacement effects (Reference 6, page 28). The thickness correction is proportional to the ratio of the geometric and computational nacelle radii. The correction due to flow incidence is proportional to the ratio of the two cross-sectional areas. The nacelle boundary potential value is:

$$\Phi_c(j,k) = A/B \tag{5}$$

where

$$A = N_x\left(\frac{r_g}{r_c}\right) + N_y\left[\frac{4\Phi(j+1,k) - \Phi(j+2,k)}{2\Delta Y} + \beta_{pod}\left(\frac{r_g}{r_c}\right)^2\right] + N_z\left[\frac{4\Phi(j,k+1) - \Phi(j,k+2)}{2\Delta Z} + (\alpha + \alpha_{pod})\left(\frac{r_g}{r_c}\right)^2\right] \tag{5.1}$$

and

$$B = \frac{3}{2}\left|\frac{N_y}{\Delta Y} + \frac{N_z}{\Delta Z}\right| \tag{5.2}$$

When the solution process is complete, computational surface velocity distributions must be converted to provide velocity distributions on the true nacelle surface. Once again, slender body theory provides the required correction:

$$V_g = V_c + (r_g - r_c)\frac{d}{dx}\left|\frac{r_g}{r_c}\left(\frac{\partial\Phi}{\partial n}\right)_{pod}\right| \tag{6}$$

Since inlet and exhaust streamtubes are not used in the present approach, it is necessary to develop boundary conditions for inlet and exhaust surfaces. An effort has been made to minimize the number of variables required for specification of fore and aft flow conditions.

First, consider the exhaust surface. By using the energy equation, an expression can be written for exit velocity (Reference 7):

$$V_J = \sqrt{\frac{2g\gamma_J R T_0}{\gamma_J - 1}\left[1 - \left(\frac{P_{J_S}}{P_{J_0}}\right)^{\frac{\gamma_J - 1}{\gamma_J}}\right]} \tag{7}$$

A similar expression can be written for the freestream velocity at infinity. The following expression evolves for the jet to freestream velocity ratio:

$$\frac{V_J}{V_\infty} = \sqrt{\frac{\frac{\gamma_J}{(\gamma_J - 1)}}{\frac{\gamma_\infty}{(\gamma_\infty - 1)}}\left(\frac{T_J}{T_\infty}\right)_0\left[\frac{1 - \left(P_{J_S}/P_{J_0}\right)^{\frac{\gamma_J - 1}{\gamma_J}}}{1 - \left(P_{\infty_S}/P_{\infty_0}\right)^{\frac{\gamma_\infty - 1}{\gamma_\infty}}}\right]} \tag{8}$$

Note that if system entropy losses are assumed to be small, jet and freestream static pressure are approximately equal; i.e.,

$$P_{J_S} \approx P_{\infty_S} \tag{9}$$

and nozzle pressure ratio is defined by:

$$NPR = P_{J_0}/P_{\infty_S} \tag{10}$$

In addition, Reference 8 provides an expression for freestream static to total pressure ratio:

$$\frac{P_{\infty_S}}{P_{\infty_0}} = \left(1 + \frac{\gamma_\infty - 1}{2} M_\infty^2\right)^{-\frac{\gamma_\infty}{\gamma_\infty - 1}} \tag{11}$$

For a freestream velocity that is equal to unity, the expression for jet exit velocity becomes:

$$V_J = \sqrt{\frac{\frac{\gamma_J}{(\gamma_J - 1)}}{\frac{\gamma_\infty}{(\gamma_\infty - 1)}} \left(\frac{T_J}{T_\infty}\right) 0 \left[\frac{1 - (1/NPR)^{\frac{\gamma_J - 1}{\gamma_J}}}{1 - 1/\left(1 + \frac{\gamma_\infty - 1}{2} M_\infty^2\right)}\right]} \qquad (12)$$

For simulating exhaust effects typically found in experimental data, the jet exhaust is cold and the following relations can be assumed:

$$\gamma_J = \gamma_\infty = 1.4 \qquad (13.1)$$

$$T_J = T_\infty \qquad (13.2)$$

Equation (12) reduces to:

$$V_{J_{cold}} = \sqrt{\frac{1 - (1/NPR)^{0.2857}}{1 - \left(1/\left(1 + 0.2M_\infty^2\right)\right)}} \qquad (14)$$

For simulating flight test exhaust effects which typically involve hot jets, the following assumptions are made:

$$T_J = 1500^0F + 460^0F \qquad (15.1)$$

$$T_\infty = 70^0F + 460^0F \qquad (15.2)$$

$$\gamma_J = 1.33 \qquad (15.3)$$

Equation (12) reduces to:

$$V_{J_{hot}} = 2.0636 \sqrt{\frac{1 - (1/NPR)^{0.2481}}{1 - \left(1/\left(1 + 0.2M_\infty^2\right)\right)}} \qquad (16)$$

Figure 6 illustrates an engine nacelle with grid points that are involved in computing inlet and exhaust face boundary potentials. By using a three-point extrapolated difference operator, an expression for exhaust velocity can be written:

$$V_e = 1 + \phi_x = 1 + \frac{1}{2\Delta X}\left(4\Phi_{(I_e+1)} - 3\phi_{(I_e)} - \phi_{(I_e+2)}\right) \qquad (17)$$

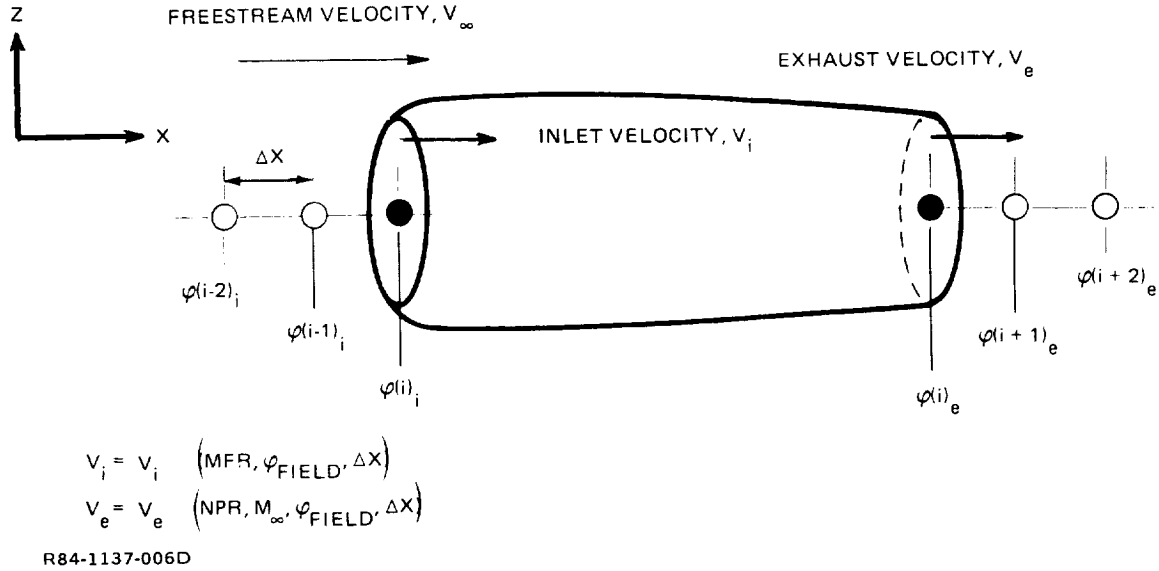

Figure 6 Nacelle Inlet & Exhaust Boundary Points

Exit velocity is then set to be equal to jet velocity providing the following expression for exhaust flow field potential:

$$\phi_{I_e} = \frac{2(1 - V_J)\Delta X + 4\Phi_{(I_e+1)} - \Phi_{(I_e+2)}}{3} \qquad (18)$$

Values of V_J will depend on whether a cold or hot jet is being simulated.

A similar expression can be derived for the value of the flow field potential at the inlet face. In this case, inlet mass flow ratio provides the required velocity relation:

$$\frac{V_I}{V_\infty} = MFR \tag{19.1}$$

$$V_I = MFR = 1 + \phi_x \tag{19.2}$$

or

$$MFR = 1 + \frac{1}{2\Delta X}\left[3\phi_{(I_i)} - 4\phi_{(I_i - 1)} + \phi_{(I_i - 2)}\right] \tag{20}$$

The inlet flow field potential becomes:

$$\phi_{I_i} = \frac{2(MFR - 1)\Delta X + 4\phi_{(I_i - 1)} - \phi_{(I_i - 2)}}{3} \tag{21}$$

For pods and stores, or other bodies which do not have inlet and exhaust flow fields associated with them, both inlet and exhaust velocities are set to 0 (MFR = 0), to simulate stagnation conditions. Tail and nose flow field potentials are then computed according to Equations (18) and (21), respectively.

Positioning of the computational nacelle surface in the global crude grid structure is an important aspect of obtaining a good flow simulation. The vertical or Z grid system is constructed using a tangent function for stretching and the wing average chord length as a characteristic length (see Reference 6, page 12). If existing mesh points are interrogated to find the closest point to the nacelle centerline, more often than not, a poor flow simulation results. Calculations indicate that computed interference effects between the nacelle and wing are very sensitive to small changes in nacelle position. For this reason, it becomes very important to assure that computational and physical nacelle heights are identical. For configurations with nacelles or pods, the basic vertical grid system is adjusted (compressed) until the grid point just beyond the nacelle centerline position (as measured from the wing plane) falls on that position. This grid adjustment procedure has been illustrated in Figure 7.

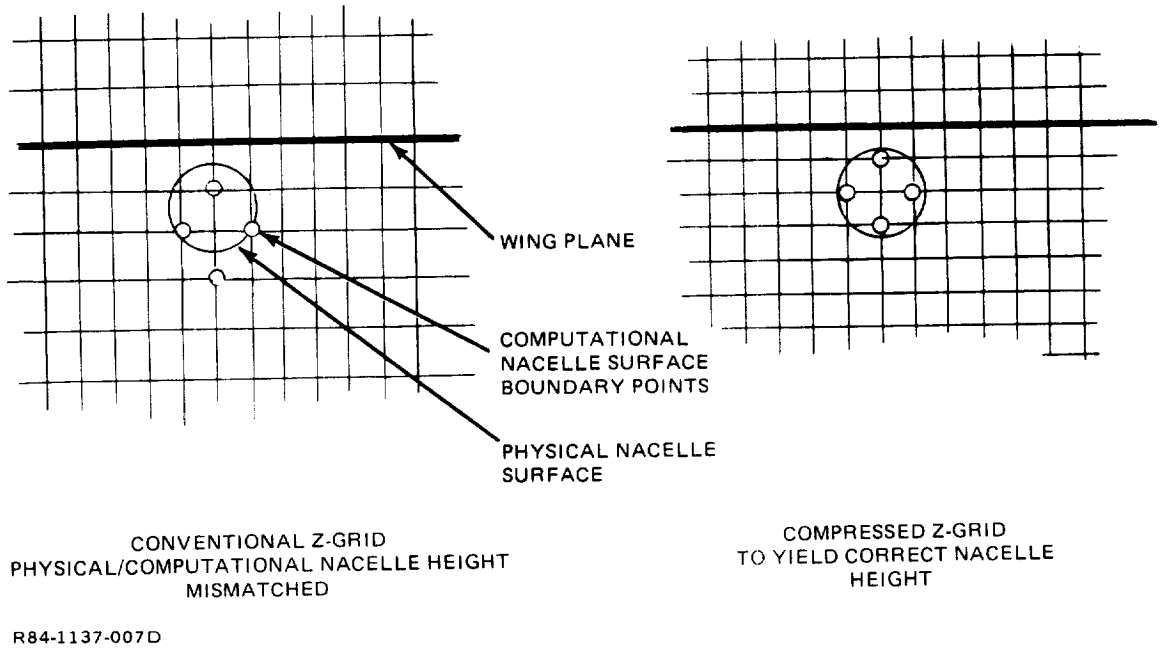

Figure 7 Global Crude Grid Adjustment for Nacelle Positioning

Spanwise positioning of the nacelle surface is not as critical as vertical positioning in most applications. The existing spanwise grid system places 18 mesh lines between the centerline and wing tip. Positioning the wing tip between two mesh lines to simulate proper aspect ratio is still the most critical requirement. As a result, the computational nacelle center may be positioned as much as 3% half-span away from the physical nacelle center position. This type of discrepancy will, as a rule, not lead to simulation problems. But in certain applications (i.e., fuselage mounted nacelle), the spanwise nacelle position may be as critical as the vertical position. Special grid provisions or compromises might be required to successfully simulate this type of flow.

Pylon Surfaces

Wing surfaces are modeled in an embedded grid system that is skewed and tapered to "fit" the wing planform (Figure 2). The spanwise lines (η) of this grid system are aligned with wing constant percent chord lines. As a result, a smooth simulation of wing leading edge flow is obtained and chordwise resolution is uniform between the root and tip of the wing.

Modeling of a surface which is not aligned with this grid system presents a problem. A symmetry plane and fuselage side are good examples of nonaligned surfaces (see Reference 6, page 24). Numerical stability is impaired in a region near the nonaligned surfaces and, in some cases, the relaxation solution diverges. Some investigators have unswept grid lines in these critical regions; however, the resulting local Cartesian grid typically produces erroneous oscillating pressure distributions. Pylon surfaces, like fuselage sides and symmetry planes, are not aligned with existing wing grid structure. Thus, the primary problem that must be overcome if pylon surfaces are to be modeled, is due to the inherent numerical instability of the pylon boundary condition.

Existing grid lines which cross the wing planform in the spanwise direction are generated by a hyperbolic tangent function and the requirement that the wing tip be centered between two grid lines. Eighteen lines are constrained to lie between the symmetry plane and wing tip. The computational pylon surface is positioned at one of these existing spanwise grid lines. A discrepancy which may be as large as 3% of wing semi-span can exist between the physical and computational pylon span position. Note that this is also true for nacelle positioning. No attempt has been made to correct for this displacement effect.

Figure 8 illustrates arrays of mesh points which are embedded along the wing. At any particular span station, the X-Z system is Cartesian in character. This wing grid system is also used to represent the pylon boundary surface. A separate grid system specifically for the pylon surface is not used. In addition, special provisions for swept leading edge simulation in the rectangular grid have not been made. As a result, current pylon modeling permits camber, twist and thickness variations; but the pylon planform is constrained to have no sweep or taper. This limitation has been sketched in Figure 9.

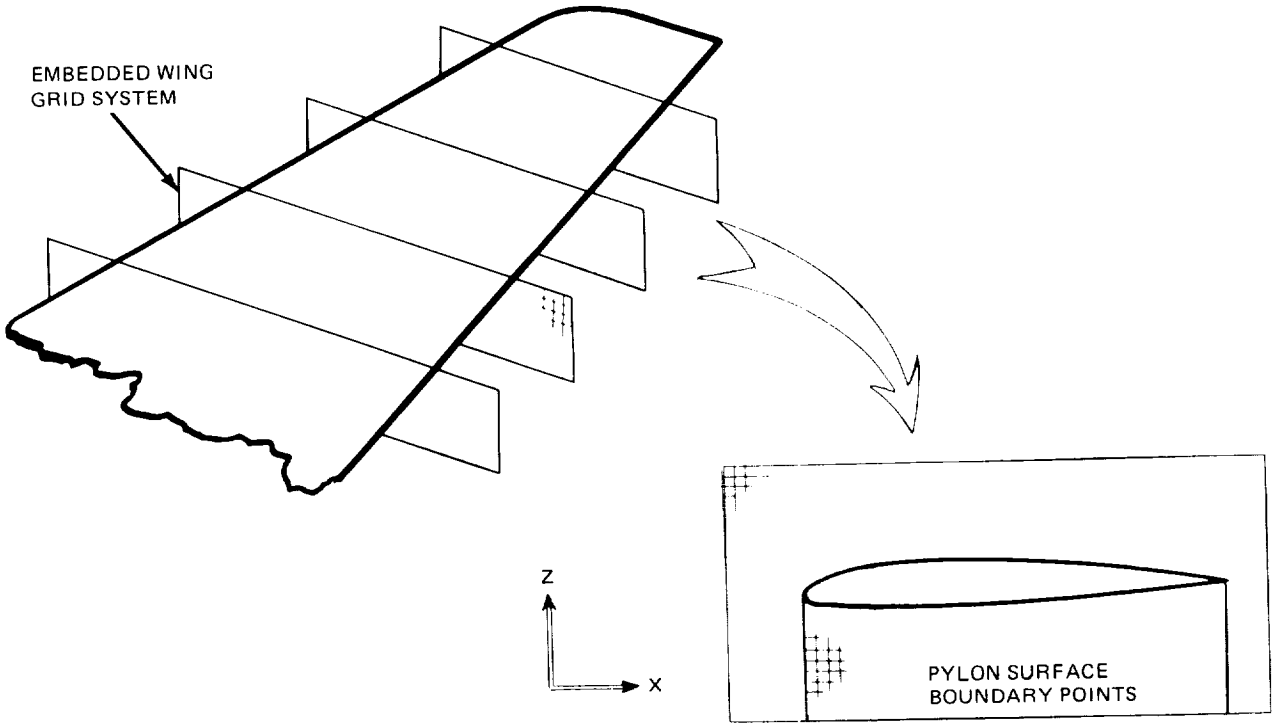

R84-1137-008D

Figure 8 Pylon Surface Boundary Points in Wing Fine Grid System

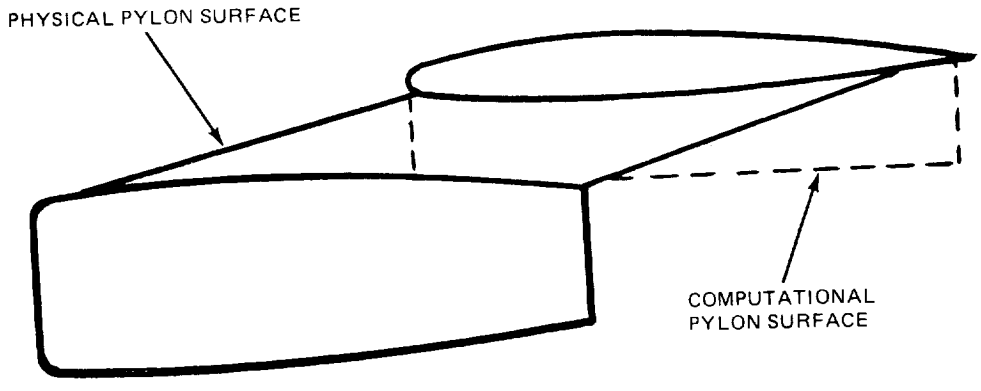

R84-1137-009D

Figure 9 Physical & Computational Pylon Surfaces

The standard wing fine grid system vertical boundaries are positioned based on a percentage of wing root chord length. When pylons are modeled, however, the fine wing grid lower boundary must be adjusted to insure that the pylon lower surface does not project below the grid limit. This is accomplished by positioning the lower grid boundary at the pylon base level and altering the vertical grid spacing so that the total number of vertical grid points remains within original limits.

There are several approaches that can be used to enforce pylon boundary conditions. In this effort, an attempt has been made to find the best compromise between providing a good flow simulation and providing a stable numerical solution that will converge for a variety of different flow/geometry cases. Calculations made to date indicate that if extrapolated differences are used to "set" the inboard and outboard pylon surface potential values, instabilities in the pylon leading edge region will result. Similarly, if pylon boundary conditions are used as a constraint on the cross-flow velocity, the solution will diverge. By using dummy potential arrays, however, a scheme can be developed which actually enhances the numerical stability of the solution. Calculations indicate that a satisfactory flow simulation is also obtained.

Figure 10 illustrates which grid points are involved in generating dummy potential values for inboard and outboard pylon surfaces. In the skewed grid system, the velocity component, v, can be written:

$$v = \phi_y = \phi_\eta \eta_y + \phi_\xi \xi_y \tag{22}$$

This can be set equal to the pylon boundary slope:

$$-\phi_y = f'_{pyl} - \beta_{pyl} \tag{23}$$

where the sign convection is due to the inboard surfaces of both winglets and pylons being specified as the input airfoil section "upper" surface. A special two-point (first order accurate) difference operator can be used to provide an approximation of the ϕ_ζ and ϕ_η derivatives. The expression for the inboard surface dummy potential point becomes:

$$\Phi_{D_{ib}} = \frac{\left[\frac{\eta_y}{\Delta Y}\Phi(i,j) - \frac{\xi_y}{\Delta X}\Phi(i+1,\ j+1) - \left(f'_{pyl_{ib}} - \beta_{pyl}\right)\right]}{\left(\frac{\eta_y}{\Delta Y} - \frac{\xi_y}{\Delta X}\right)} \qquad (24)$$

A similar expression can be written for the outboard surface dummy potential point:

$$\Phi_{D_{ob}} = \frac{\left[\frac{\xi_y}{\Delta X}\Phi(i-1,\ j-1) - \frac{\eta_y}{\Delta Y}\Phi(i,j) - \left(f'_{pyl_{ob}} - \beta_{pyl}\right)\right]}{\left(\frac{\xi_y}{\Delta X} - \frac{\eta_y}{\Delta Y}\right)} \qquad (25)$$

For each side, note that the coefficient of the dummy potential point is greater than the coefficient of other points involved. This enhances the effective diagonal dominance of the system.

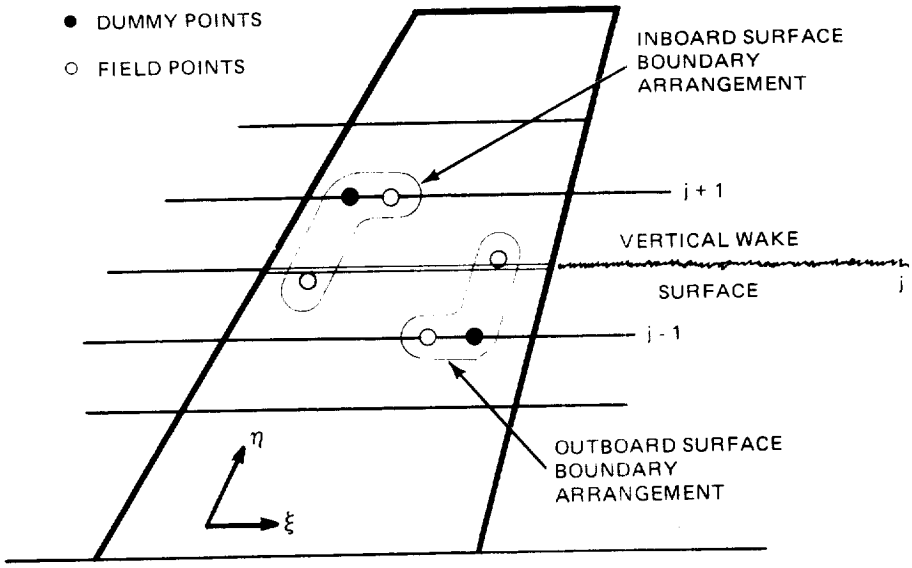

NOTE: FOR SWEPT-BACK WINGS, $\xi_y < 0$

$$\varphi_y = \varphi_\xi \xi_y + \varphi_\eta \eta_y$$

R84-1137-010D

Figure 10 Grid Points Required for Computing Pylon Inboard/Outboard Boundary Conditions

The computational method operates with three planes of grid point potentials in core at one time. When a pylon station is reached, the outboard plane is modified in the region which is directly aligned with the pylon surface. Equation 24 provides the temporary dummy flow field potential values. The inboard pylon surface is then relaxed in a manner similar to that used for normal field points. When the wing/pylon trailing edge is reached, the original outboard potential values are replaced, and inboard plane dummy values are established. The outboard side of the pylon surface is then relaxed and the pylon surface simulation is complete. Vertical pylon circulation is computed by:

$$\Gamma(Z)_{pyl} = \Phi_{J_{ib}} - \Phi_{J_{ob}} \tag{26}$$

This value of circulation provides the jump condition required for differencing across the pylon wake surface:

$$\Phi_{\eta\eta_{ib}} = \frac{\Phi_{(j-1,k)} - 2\Phi_{(j,k)} + \left[\Phi_{(j+1,k)} + \Gamma(Z)\right]}{\Delta\eta^2} \tag{27}$$

$$\Phi_{\eta\eta_{ob}} = \frac{\left[\Phi_{(j-1,k)} - \Gamma(Z)\right] - 2\Phi_{(j,k)} + \Phi_{(j+1,k)}}{\Delta\eta^2} \tag{28}$$

Winglet Surfaces

For wing-tip-mounted winglets, the small size of the lifting surface alone presents a formidable obstacle. Winglet planform areas are typically between 1/40 and 1/70 the area of the main wing. Sufficient resolution must be provided for both wing and winglet surfaces simultaneously. The stability problems which occurred when pylon development was in progress are not incurred since rectangular grid systems are set up specifically for winglet surface simulation to overcome the resolution problem.

Spanwise grid arrangement for a conventional wing tip is shown in Figure 11. The wing tip is positioned midway between two grid lines. This provides the best approximation of wing tip aerodynamics. If a winglet is modeled, the grid system must be adjusted to provide grid lines at the wing tip. These wing tip points are used for both the winglet boundary surface and the vertical winglet wake which extends to downstream infinity.

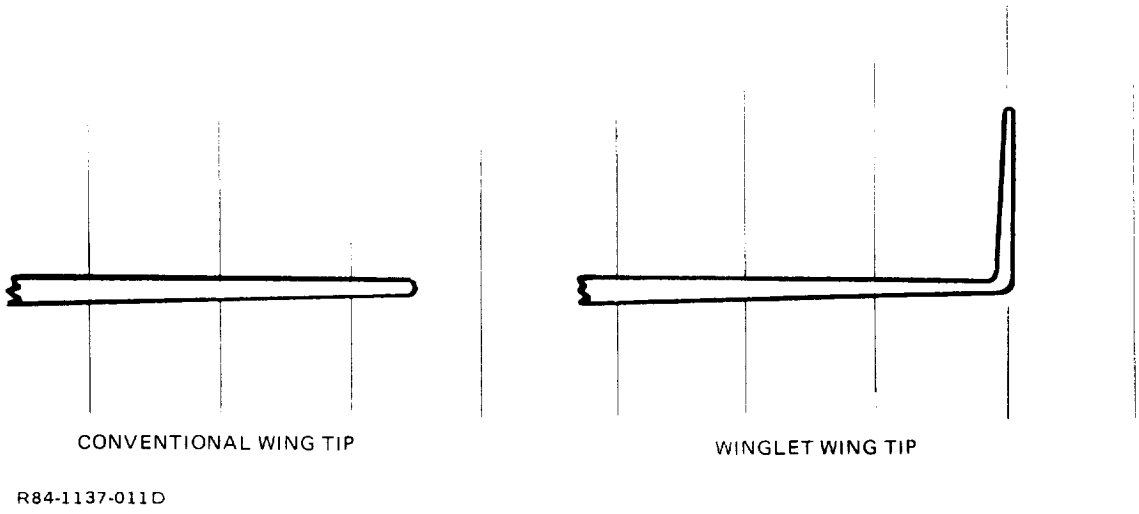

Figure 11 Wing Tip Spanwise Grid System for Winglet & Conventional Type Planforms

If a fine grid system were embedded along the winglet surface in the same manner currently used for wing surfaces, a diverging solution would probably result. This would be caused by the large disparity in resolution between the existing global crude grid structure and the embedded fine grid system. To overcome this problem, an intermediate mesh system is placed around the wing tip region. Figure 12 illustrates the resulting three-level grid arrangement required for resolving details of winglet flow fields. Both the global crude grid and intermediate grid are rectangular in character. The winglet embedded (fine) grid system is skewed and tapered to fit the winglet planform.

During the first phase of the solution process, only crude and intermediate grid systems are active. Winglet boundary conditions are imposed in the

higher resolution intermediate grid system. Since vertical line relaxation is used, the boundary condition is enforced by specifying the cross-flow velocity component in Equation (1). (Note that this will involve both the ϕ_y and ϕ_{xy} terms.) Winglet circulation and wake jump computations are identical to those specified for pylon surfaces (Equations 26, 27 and 28). Crude grid winglet points form a fixed potential surface and flow field potentials are generated by the interpolating values found in the intermediate grid. Most important, however, the crude grid system provides a means for carrying vertical wake circulation downstream.

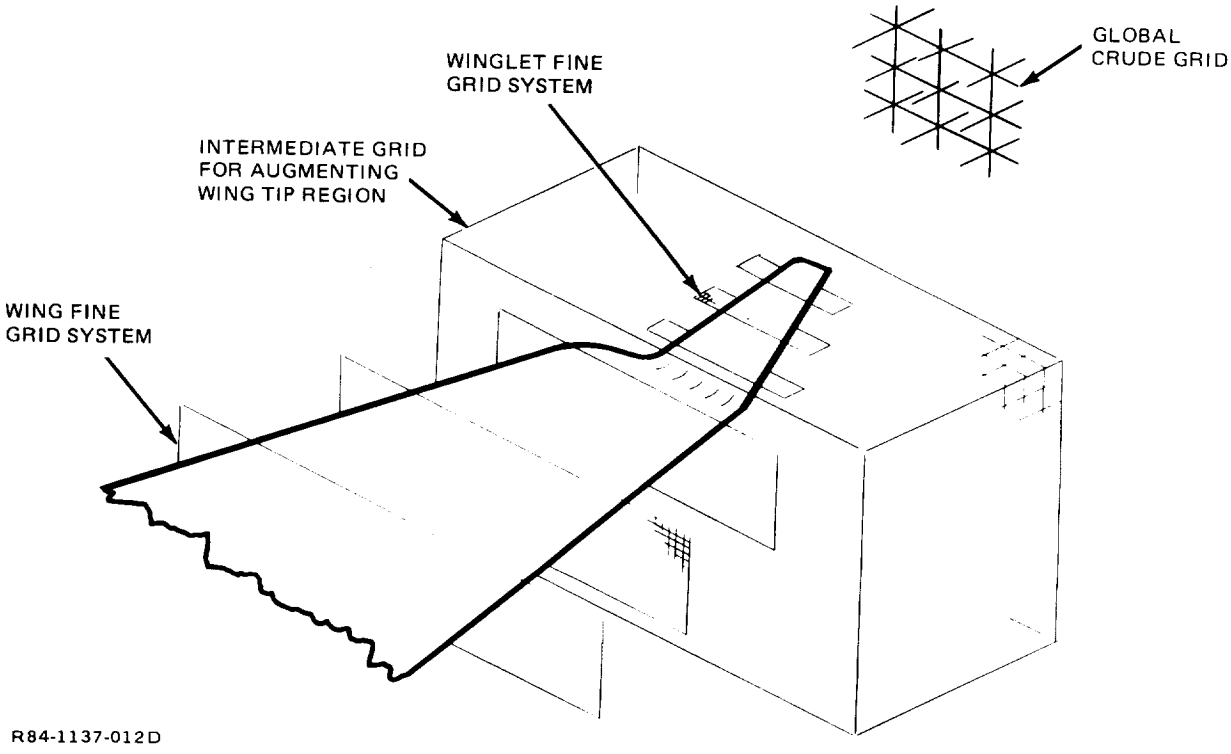

Figure 12 Crude/Medium/Fine Grid Arrangement for Wing-Tip-Mounted Winglets

The winglet flow field computed during the first phase of the solution process is used to provide a starting point for the second phase which requires crude-medium-fine grid interactions. Fine winglet grid boundary con-

ditions and fine wing grid boundary conditions are identical. Only the coordinate direction is changed. For the winglet inboard surface, the boundary condition is:

$$\phi_{yy}(x,y_{ib},z) = \frac{2}{\Delta Y}\left(\frac{\phi(j-1,k) - \phi(j,k)}{\Delta Y} - (f'_{wlt_{ib}} - \beta_{wlt})\right) \qquad (29)$$

The outboard surface condition is:

$$\phi_{yy}(x,y_{ob},z) = -\frac{2}{\Delta Y}\left(\frac{\phi(j,k) - \phi(j+1,k)}{\Delta Y} - (f'_{wlt_{ob}} - \beta_{wlt})\right) \qquad (30)$$

During the second phase of the solution process, flow field potentials are fixed on both crude and intermediate grid winglet surfaces. The global crude grid solution provides outer boundary potentials for the intermediate grid. The intermediate or medium grid solution provides outer boundary potentials for the embedded fine grid system.

Solution Process

This section describes the procedure which is used to solve for the multiple wing and body surface flow field. The procedure includes steps that are executed when nacelles, pylons and winglets are attached to the basic wing-body configuration. For simpler configurations, individual component steps are simply bypassed. Figures 2, 4 and 12 may prove to be useful in visualizing operations which are to be described. The solution process can be broken down into two separate phases.

Phase 1: INITIAL CRUDE GRID FLOW FIELD SOLUTION

An initial solution is obtained with the wing-body represented in the crude mesh. Typically, 100 iterations are sufficient. After 60% of the crude cycles are completed, flow field potentials from the global crude grid are used to establish a starting flow in the wing tip augmented grid (TAG). Note that TAG was referred to as an intermediate grid in the winglet surface section. For the remaining

40% of the crude grid cycles, winglet boundary conditions are enforced in TAG and the global grid serves also to carry wing and winglet wake systems downstream.

Phase 2: CRUDE/FINE GRID INTERACTION

Step 1: Using global crude grid flow field potentials obtained in Phase 1, a starting flow field for the embedded wing grid is established. A similar initialization procedure is performed for the embedded pod or body grid system. Flow field potentials from TAG provide a starting flow field for the winglet embedded grid system. Pylon outboard potential arrays are set equal to inboard potential values which make up the basic wing flow field. Pylon circulation distributions are set to zero.

Step 2: The wing fine grid system is relaxed with outer perimeter potential values fixed and conventional Neumann boundary conditions at fine grid section boundary points. Crude grid wing boundary point potentials are updated based on results from this step.

Step 3: The winglet fine grid system is relaxed in a manner similar to that in Step 2. Both the crude grid and TAG winglet surface boundary potentials are updated.

Step 4: Wing boundary layer δ^* is computed. Embedded body fine grid perimeter points are updated, based on global crude grid field potentials. Body fine grid boundary potentials are computed.

Step 5: The body fine grid system is relaxed subject to fixed potential values on the grid perimeter, body surface, and wing plane surface (see Figure 15, Reference 6).

Step 6: The crude grid body surface is updated based on fine grid field potentials determined in Step 5.

Step 7: The nacelle fine grid system is relaxed in a manner similar to that of the body (Steps 5 and 6). In addition, however, flow field potentials at inlet and exhaust faces must be determined before each relaxation sweep.

Step 8: The global crude grid is relaxed using Dirichlet boundary potentials generated by Steps 1-7. Field potentials from the crude grid now provide outer boundary potentials for embedded grid arrays.

Step 9: The TAG is relaxed with fixed perimeter and winglet surface boundary points.

Steps 1 through 9 are repeated until the grid systems are satisfactorily converged. Typically, 80 cycles are sufficient. When the boundary layer option is selected, a boundary layer displacement thickness (δ^*) will be computed every 20th iteration starting with the fifth iteration in phase two. The δ^* gradient is added to the wing surface slope for the wing boundary condition required in step 2. If the fine body or pod grid option is selected, grid perimeter potentials are updated every 10th iteration and the grid systems are relaxed every second iteration to conserve computing resources.

Pressure, Force and Moment Coefficients

Pressure, force and moment coefficient calculations for wing and body components are described in Reference 6. All pressure coefficients on pod, pylon, and winglet components are computed in the same manner as those described in Reference 6. Pylon surfaces, which are perpendicular to the wing plane, do not contribute to the total configuration forces and moments. For this reason, only nacelle and winglet force and moment calculations will be described.

Winglet section coefficients are obtained by integrating pressure coefficients on both inboard and outboard surfaces.

$$C_{\ell_{\omega\ell t}} = -\frac{1}{C_{loc}} \int_{o}^{c} (Cp_{ib} - Cp_{ob})\, dx \tag{31}$$

$$C_{m_{\omega\ell t}(loc)} = \frac{1}{C_{loc}^{2}} \int_{o}^{c} (Cp_{ib} - Cp_{ob})\,(X_{loc} - X_{c/4})\, dx \tag{32}$$

$$C_{d_{\omega\ell t}} = \frac{1}{C_{loc}} \int_{o}^{c} \left[Cp_{ib}\left(\frac{dy_{ib}}{dx} - \psi\right) - Cp_{ob}\left(\frac{dy_{ob}}{dx} - \psi\right)\right] dx \tag{33}$$

In addition, a sectional moment about the axial reference position is computed.

$$C_{m_{\omega\ell t}} = \frac{1}{M.A.C.\ C_{loc}} \int_{o}^{c} (C_{P_{ib}} - C_{P_{ob}})(X_{loc} - X_{REF})\, dx \tag{34}$$

Winglet lift, moment and drag coefficients are obtained by integrating section coefficients across the winglet span and multiplying by winglet cant angle.

$$C_{L_{WLT}} = \cos\Omega\, \frac{2}{b} \int_{o}^{b/2} \left(\frac{C_{loc}\, C_{\ell_{\omega lt}}}{C_{av}}\right) dy \tag{35}$$

$$C_{M_{WLT}} = \cos\Omega\, \frac{2}{b} \int_{o}^{b/2} \left(\frac{C_{loc}\, C_{m_{\omega lt}}}{C_{av}}\right) dy \tag{36}$$

$$C_{D_{P(WLT)}} = \frac{2}{b} \int_{o}^{b/2} \left(\frac{C_{loc}\, C_{d_{\omega lt}}}{C_{av}}\right) dy \tag{37}$$

Winglet skin friction drag is computed by using the Prandtl-Schlichting formula corrected for compressibility effects (see Equation 64, Reference 6).

Pod or nacelle force and moment coefficients are obtained by integrating surface pressure distributions and adding a skin friction component based on wetted area. A pod cross-sectional force coefficient distribution is computed first.

$$C_{\ell_{pod}} = \frac{-1}{2R_{loc}} \int_{-R_{loc}}^{R_{loc}} [C_P \cdot N_z]_{UPPER} \, dy - \frac{1}{2R_{loc}} \int_{-R_{loc}}^{R_{loc}} [C_P \cdot N_z]_{LOWER} \, dy \quad (38)$$

and

$$C_{d_{pod}} = \frac{1}{2R_{loc}} \int_{-R_{loc}}^{R_{loc}} [C_P \cdot N_x]_{UPPER} \, dy + \frac{1}{2R_{loc}} \int_{-R_{loc}}^{R_{loc}} [C_P \cdot N_x]_{LOWER} \, dy \quad (39)$$

The longitudinal coefficients are then integrated along the length of the body.

$$C_{L_{POD}} = \frac{1}{L} \int_{o}^{L} \left[\frac{C_{\ell_{pod}} \cdot R_{loc}}{R_{max}} \right] d\ell \quad (40)$$

Similarly,

$$C_{M_{POD}} = \frac{1}{L^2} \int_{o}^{L} \left[\frac{C_{\ell_{pod}} \cdot R_{loc}}{R_{max}} \right] (x_{loc} - x_{REF}) \, d\ell \quad (41)$$

and

$$C_{D_{POD}} = \frac{1}{L} \int_{o}^{L} \left[\frac{C_{d_{pod}} \cdot R_{loc}}{R_{max}} \right] d\ell \quad (42)$$

As was the case for winglets, the pod skin friction coefficient is computed using the Prandtl-Schlichting formula (see Equation 64, Reference 6).

The total configuration force and moment coefficients are obtained by adding the various component coefficients.

$$C_L = C_{L_{WING}} + C_{L_{BODY}} + C_{L_{WLT}} + C_{L_{PODS}} \quad (43)$$

$$C_M = C_{M_{WING}} + C_{M_{BODY}} + C_{M_{WLT}} + C_{M_{PODS}} \quad (44)$$

$$C_D = C_{D_{WING}} + C_{D_{BODY}} + C_{D_{WLT}} + C_{D_{PODS}} \quad (45)$$

Two-Dimensional Airfoil Analysis

The modified small disturbance equation/planar boundary condition approach, the basis for the present method, may in some cases produce results which are inferior to those that would be obtained if a full potential equation/exact boundary condition method were available. These discrepancies might become significant when surface shapes have extraordinarily high gradients or when flow conditions are extreme. Unfortunately, it would be difficult to evaluate potential problem areas when complex configurations are of interest. Flow interference can be complex and many different components of the computational method are contributing to the final result. For these reasons, special provisions have been made to permit analysis of two-dimensional airfoil shapes. Abundant experimental data and easy-to-use full potential equation/exact boundary condition computer analyses can then be used to assess problem areas in two dimensions before complex three-dimensional analyses are performed.

Figure 2 illustrated the position of the wing embedded fine grid system. This mesh array is made up of a series of two-dimensional arrays (see Figure 8). If a single planar array is used at the symmetry plane, a two-dimensional airfoil can be treated. Unlike the wing-body case (see Figure 13), however, far field boundaries which represent infinity are non-zero since the airfoil appears as a concentrated point vortex. This has been illustrated in Figure 14.

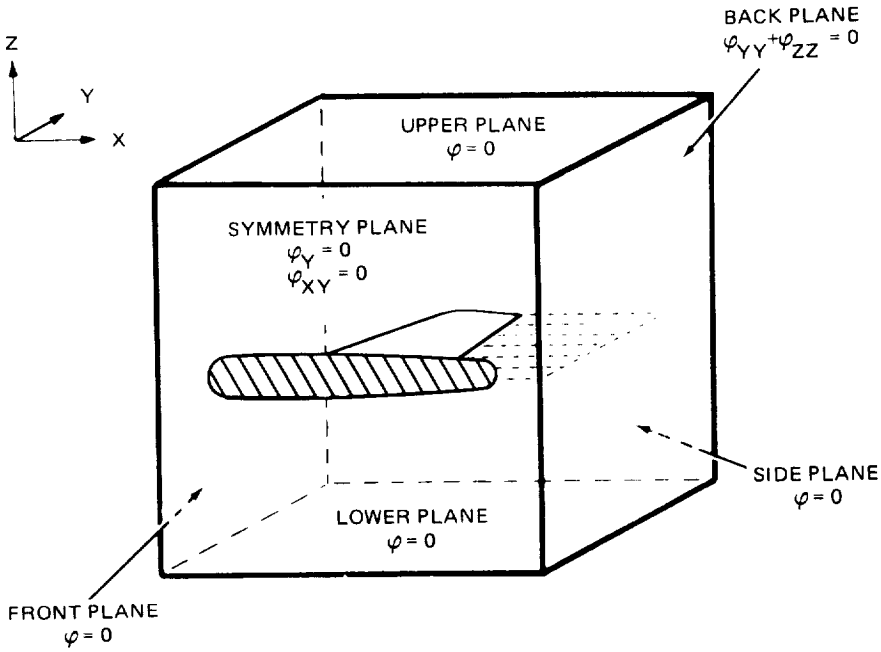

R84-1137-013D

Figure 13 Boundary Conditions at Infinity for Wing-Body Analysis

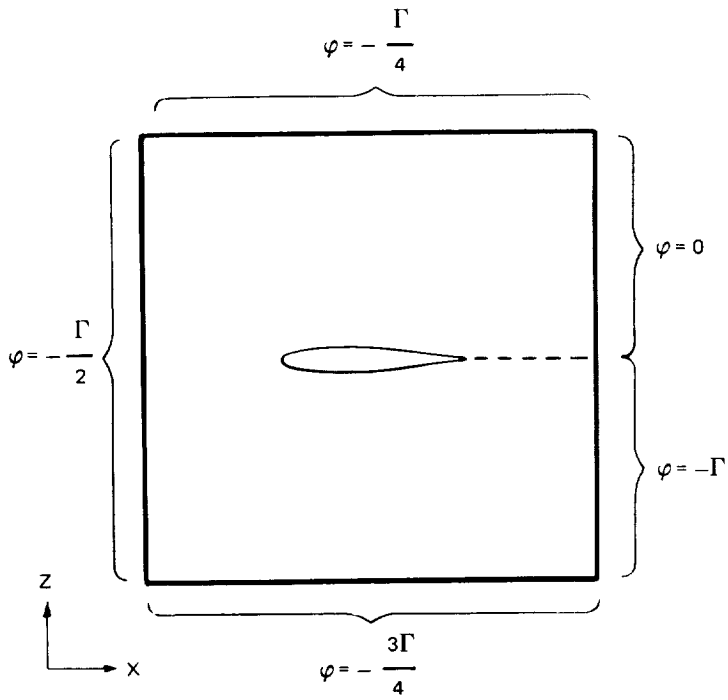

R84-1137-014D

Figure 14 Boundary Conditions at Infinity for Airfoil Analysis

The global flow equation (Equation 1) which is used for all three-dimensional computations is simplified by eliminating all cross-flow terms when airfoil analysis is required.

$$\left[1 - M_{\infty}^2 - (\gamma + 1)M_{\infty}^2\phi_x - \frac{\gamma + 1}{2} M_{\infty}^2\phi_x^2\right]\phi_{xx} + \phi_{zz} = 0 \qquad (46)$$

Airfoil pressure coefficients are computed using the following equation.

$$Cp = -[2\phi_x + (1 - M_{\infty}^2)\phi_x^2] \qquad (47)$$

COMPARISONS & TYPICAL RESULTS

Correlations with experimental data for isolated bodies, isolated wings, and wing-body combinations were presented in Reference 6 using the basic wing-body code. These examples will not be included in this report, but it should be noted that the present method will reproduce those results in addition to providing the more complex configuration flow simulations contained herein. Thus, the present method can be used to analyze 1) two-dimensional airfoils, 2) isolated wings, 3) isolated bodies, 4) wing-body combinations, and 5) aircraft configurations with as many as four pods/nacelles, four pylons, and wing-tip-mounted winglets. This provides flexibility for studying component interference effects.

The computations which follow illustrate the new airfoil and nacelle, pylon, winglet simulation capabilities. Component interference effects are shown for cases where component on/off wind tunnel data is available. For some components (nacelles and winglets), detailed pressure comparisons are included. For one case (G-III), flight data is used to augment wind tunnel results.

Airfoil Correlations

Two airfoils have been selected for correlation studies. The NACA 0012 airfoil is somewhat conventional in shape. It is also a section which is often used in theoretical or analytical test samples. The second airfoil selected is the new type NASA LS(1) airfoil which features considerable aft-loading. Experimental data for these sections can be found in Reference 9 along with Korn-Garabedian and Carlson 2-D code analysis results. Correlations with experimental data using the present method can be seen in Figure 15.

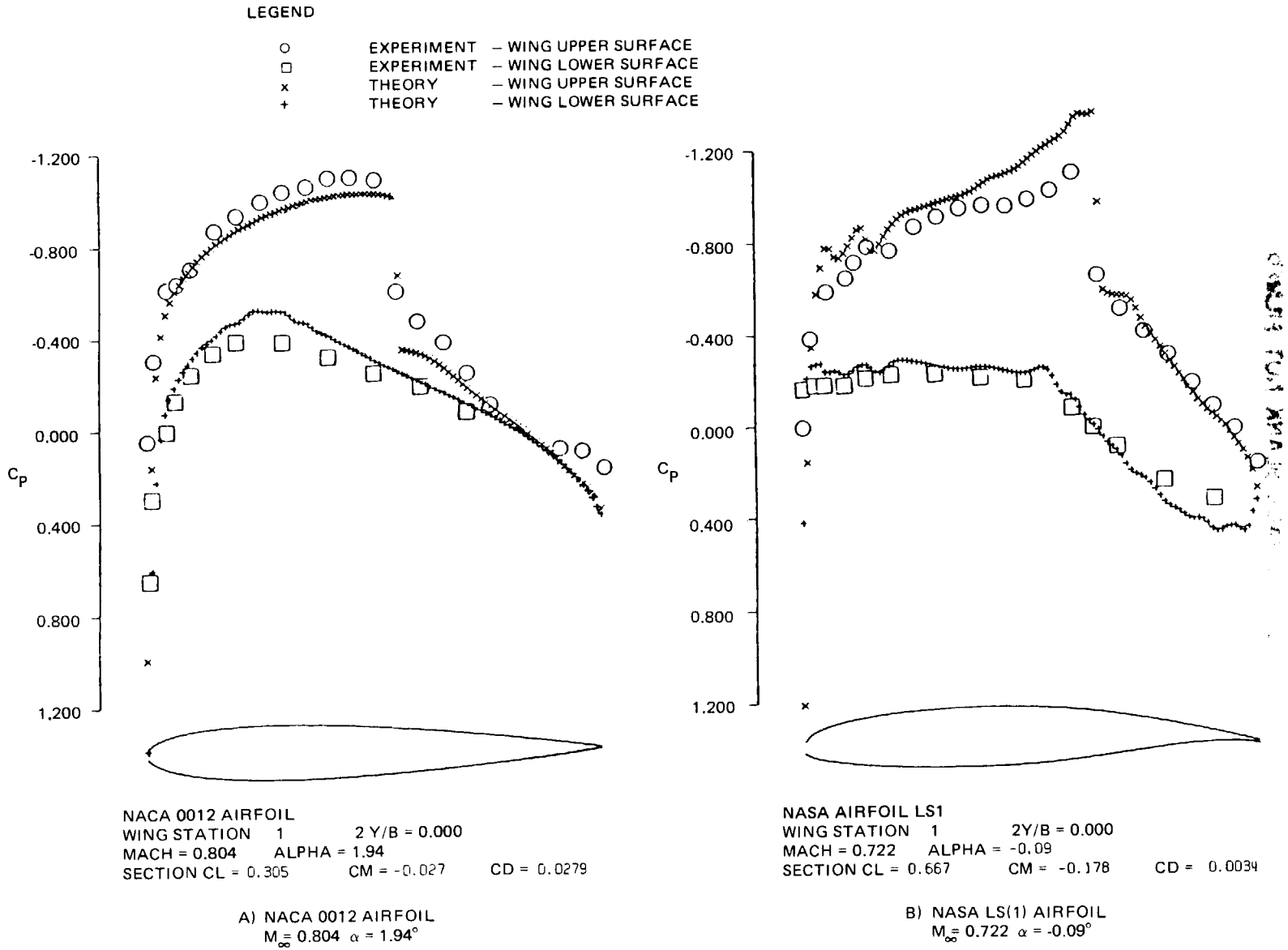

A) NACA 0012 AIRFOIL
M_∞ = 0.804 α = 1.94°

B) NASA LS(1) AIRFOIL
M_∞ = 0.722 α = -0.09°

R84-1137-015D

Figure 15 Two-Dimensional Airfoil Pressure Distribution Correlation

Nacelle Flow Simulations

Two different transport configurations have been selected for comparisons to experimental data. Together, they illustrate both nacelle operational modes. The first, a crude grid nacelle simulation, provides flow disturbances on the wing. The second involves a fine embedded grid computation which is used to predict detailed pressures on the engine nacelle surface.

Figure 16 illustrates the G-III configuration. This transport has a low wing and two fuselage-mounted nacelles. The wing has an aspect ratio of 6, and a taper ratio of 0.279. Wing leading edge sweep is 31.7 degrees. Nacelles are canted 2.75 degrees nose up, and 0.5 degrees nose inboard.

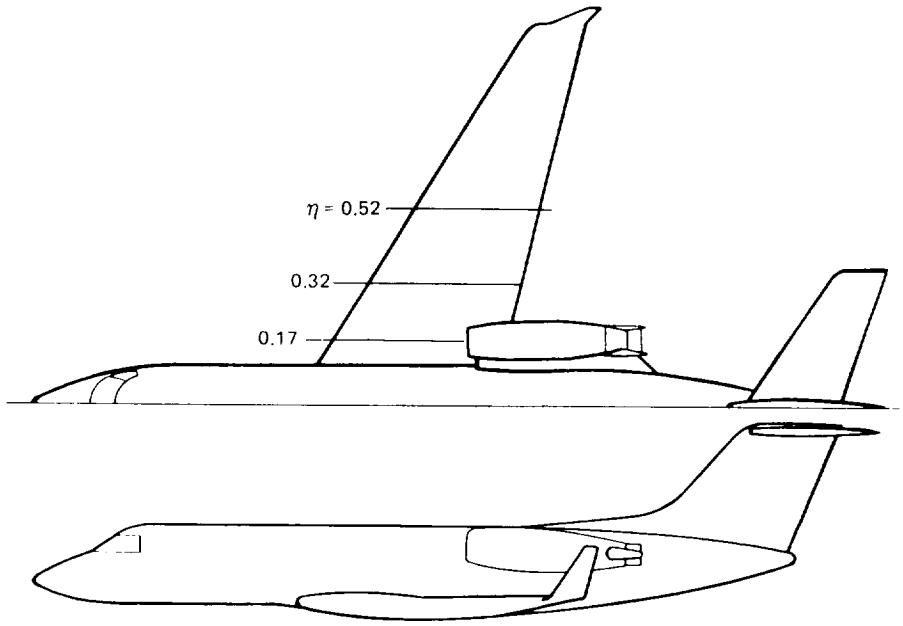

Figure 16 G-III with Pressure Tap Locations for Nacelle Interference Study

G-III cruise conditions occur near Mach 0.75 and an angle-of-attack of 4 degrees. The wing root pressure distribution at this flow condition is relatively shock free and not very challenging for the transonic computational method. For this reason, a higher Mach number case has been selected for comparisons. The Mach 0.85 flow condition exhibits a strong shock wave. The selected incidence must be lower than cruise levels to avoid flow separation.

Wing upper surface, superimposed, computed pressure distributions for the basic wing-fuselage and the wing-fuselage-nacelle cases can be seen in Figure 17 at Mach 0.85 and 0 degree angle-of-attack. A single shock wave spans the wing between the fuselage side and wing tip. With the nacelle mounted, the shock wave disappears in the wing-fuselage-nacelle juncture region. Resulting flow on the wing under the nacelle exhibits a deceleration in front of the inlet face, and an acceleration just behind the inlet lip. The inlet MFR for this case is 0.66.

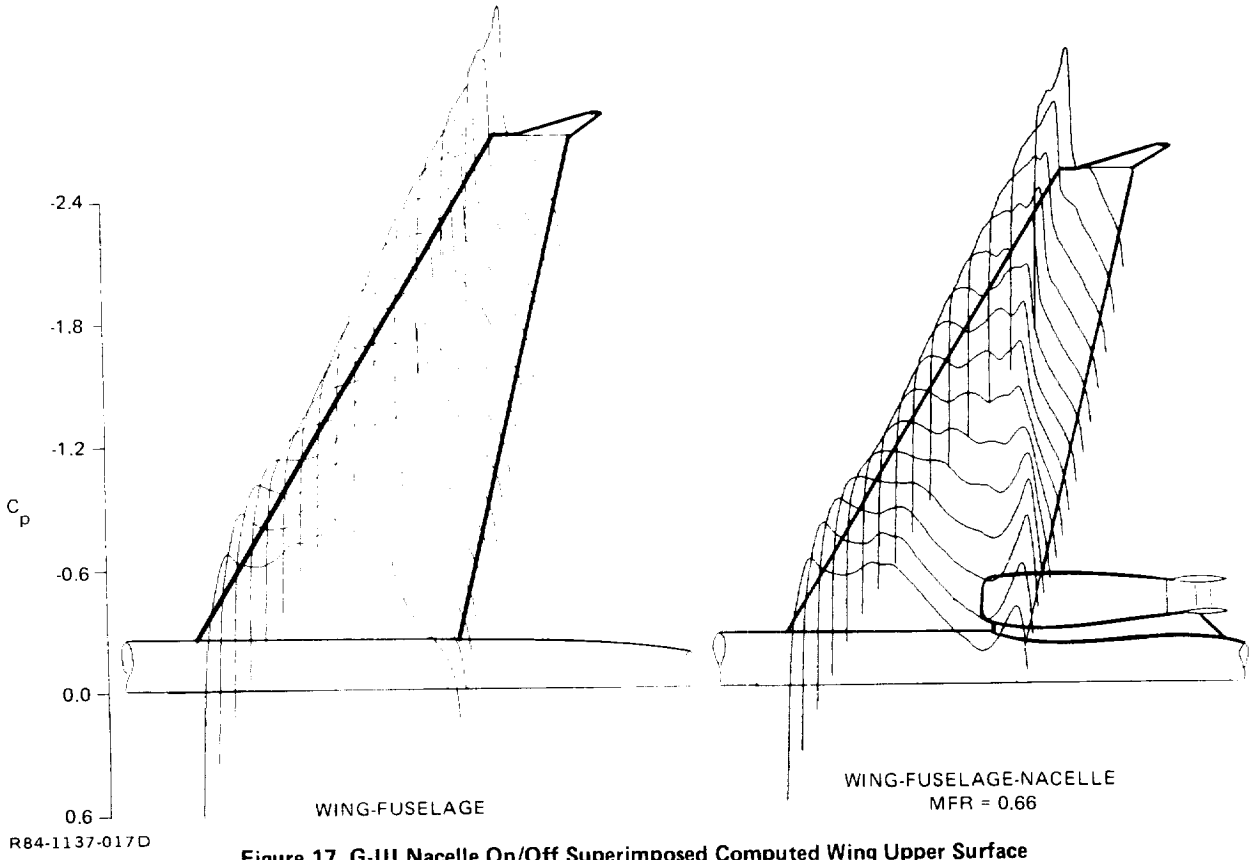

Figure 17 G-III Nacelle On/Off Superimposed Computed Wing Upper Surface Pressure Distributions $M_\infty = 0.85$, $\alpha = 0^\circ$

Correlations with experimental data at three span stations along the wing can be seen in Figure 18. Note that the character of this complex three-dimensional flow field is predicted quite well. The lower surface pressures are essentially unaffected by the presence of the engine, and the interference effect can be observed to decay properly as distance from the nacelle increases. Experimental data is taken from Reference 10.

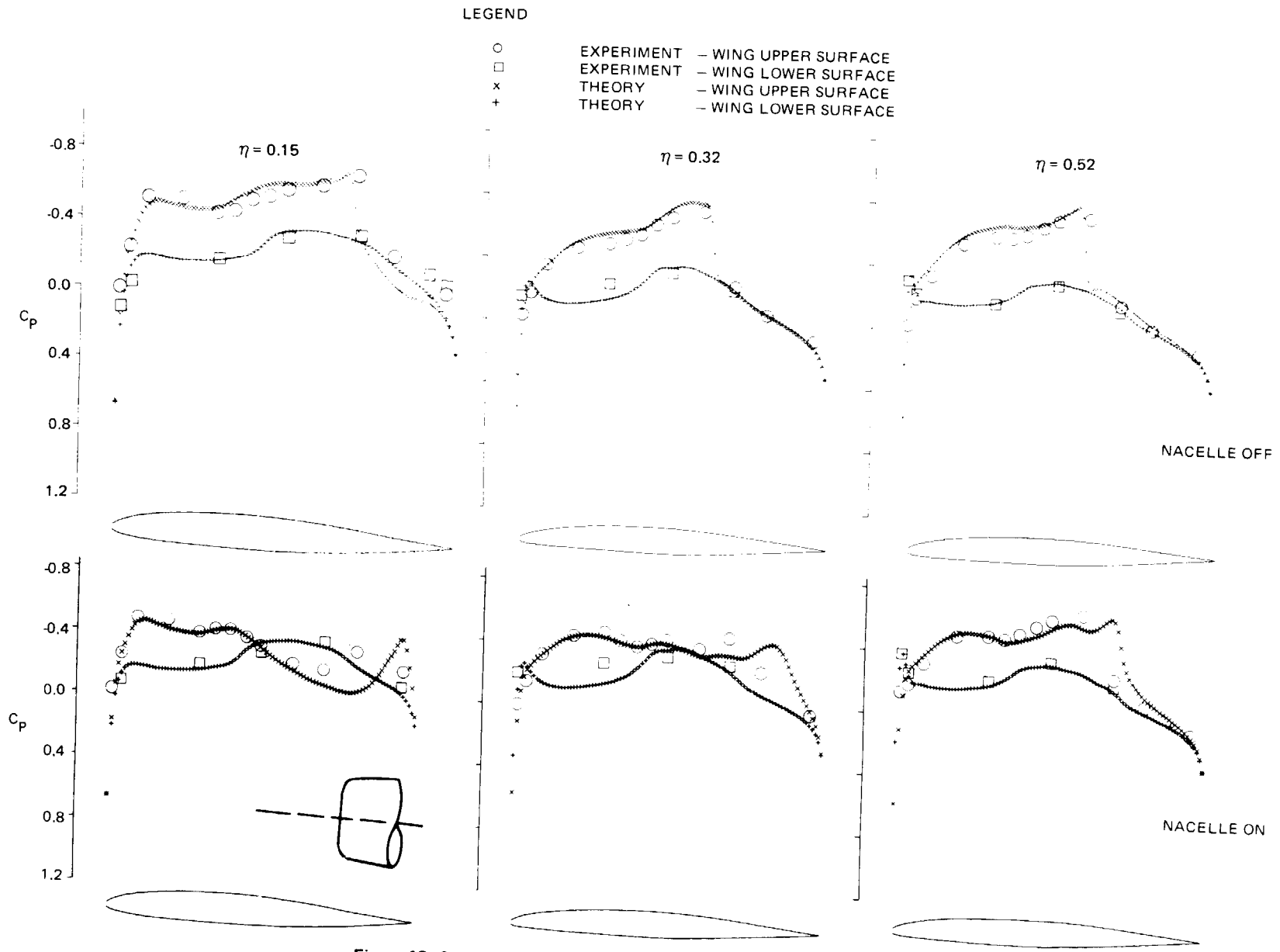

R84-1137-018D

Figure 18 G-III Nacelle On/Off Wing Pressure Distribution Correlations
$M_\infty = 0.85$, $\alpha = 0°$

The C-5A configuration is illustrated in Figure 19. For flow conditions near the cruise point (M_∞ = 0.775 and α = 2.0 degrees), an embedded fine grid has been positioned around the inboard engine nacelle. Experimental data can be found in Reference 11. The actual engine consists of a fan cowl, turbine cowl and plug. Engine surface discontinuities and expected flow separation aft of the fan cowl cannot be properly modeled using the present attached flow methodology. For this reason, the long duct flow-through nacelle (Configuration 10, Reference 11) is modeled for analysis. Computed results are compared to experimental pressures which were measured on the basic nacelle (Configuration 1).

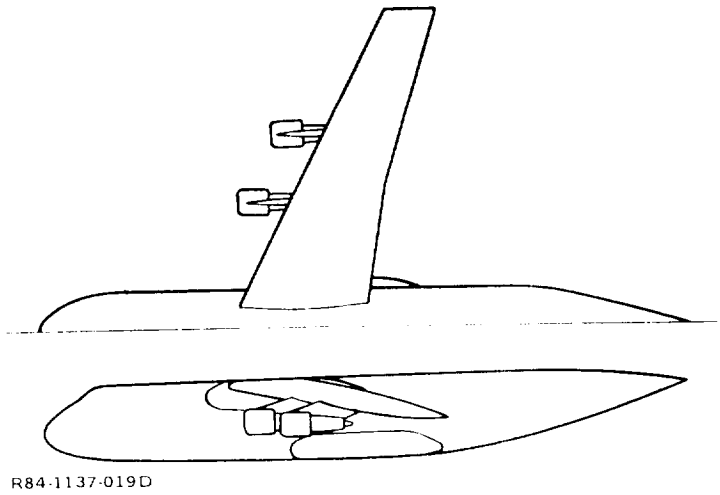

Figure 19 C-5A Configuration

Correlations with experimental data at three stations around the nacelle can be seen in Figure 20. Note that both basic and flow-through nacelle shapes have been sketched. Computed results on the turbine portion of the nacelle can only be considered as approximate. They are included because the character of this flow which is influenced by the wing leading edge is properly predicted.

Figure 21 shows inboard nacelle port and starboard comparisons superimposed. The variation in flow character is probably caused by a combination of interference effects that include fuselage effects inboard, second nacelle effects outboard, and the swept back wing leading edge.

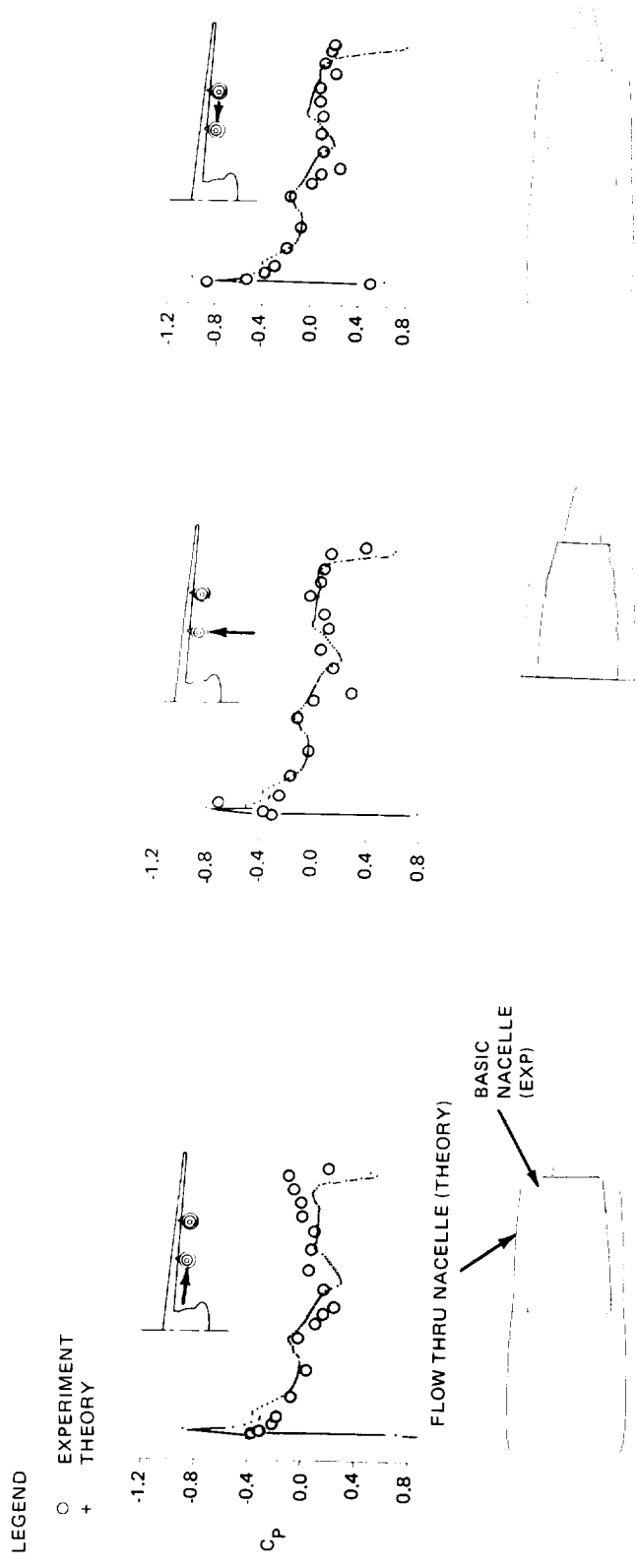

Figure 20 C-5A Inboard Nacelle Pressure Distribution Correlation $M_\infty = 0.775$, $\alpha = 2°$, NPR = 2.84

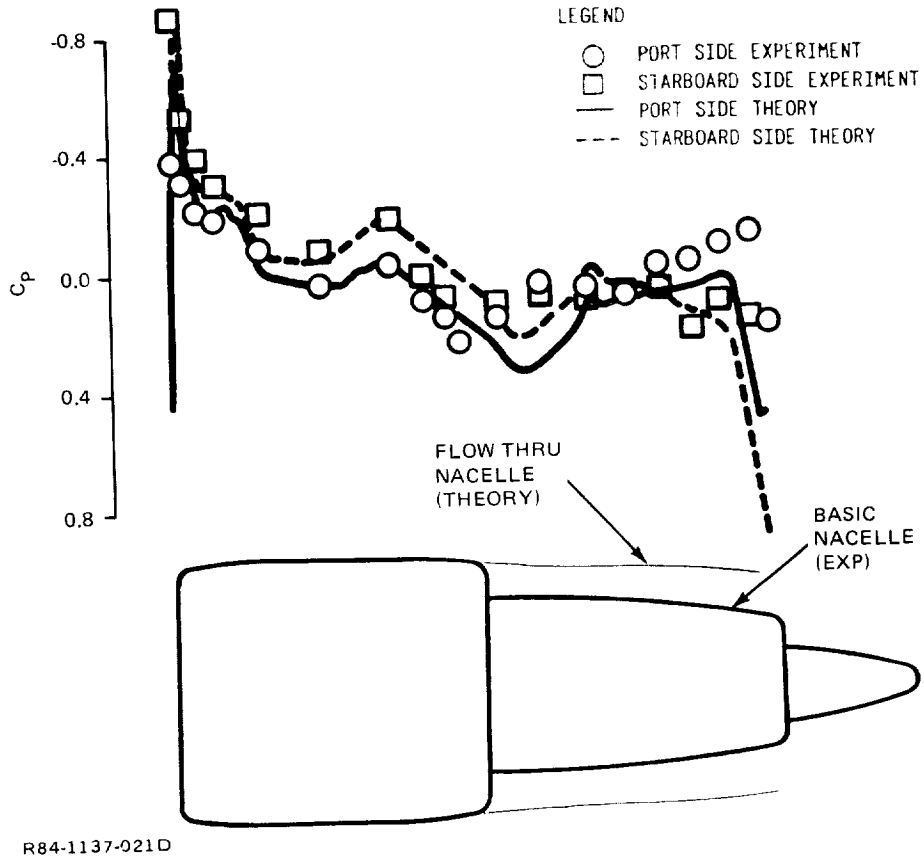

Figure 21 Comparison of C-5A Inboard Nacelle Port and Starboard Pressure Distribution Correlations
$M_\infty = 0.775$ $\alpha = 2°$ NPR = 2.84

Pylon Interference Effects

The C-5A configuration (Figure 19) has been selected to demonstrate the pylon computational capability. Reference 11 provides experimental data for the basic C-5A wing-fuselage configuration and various configurations with different pylon and nacelle combinations. Wing pressure data which illustrate pylon interference effects are available at both pylon span stations (Figure 22). For the wing lower surface, pressure taps are positioned on both sides of the wing pylon juncture. A double shock wave system exists inboard of the mid-semi-span region; outboard, only a single shock wave exists. Correlations with experimental data at the inboard station for the pylon/nacelle on and off can be seen in Figure 23. Outboard station comparisons can be found in

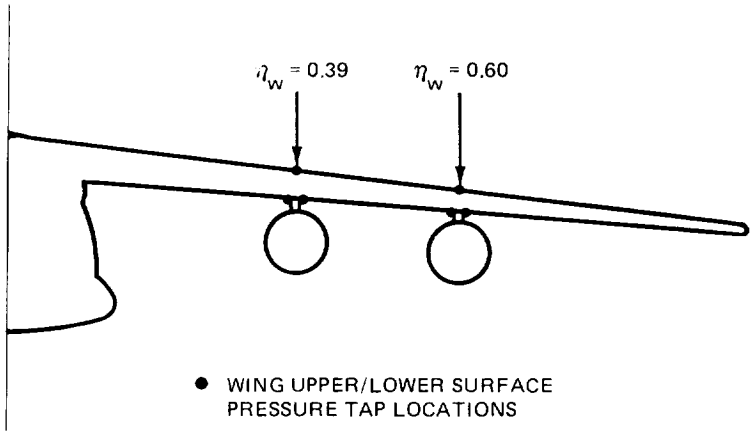

Figure 22 C-5A Wing Stations for Pylon/Nacelle Interference Study

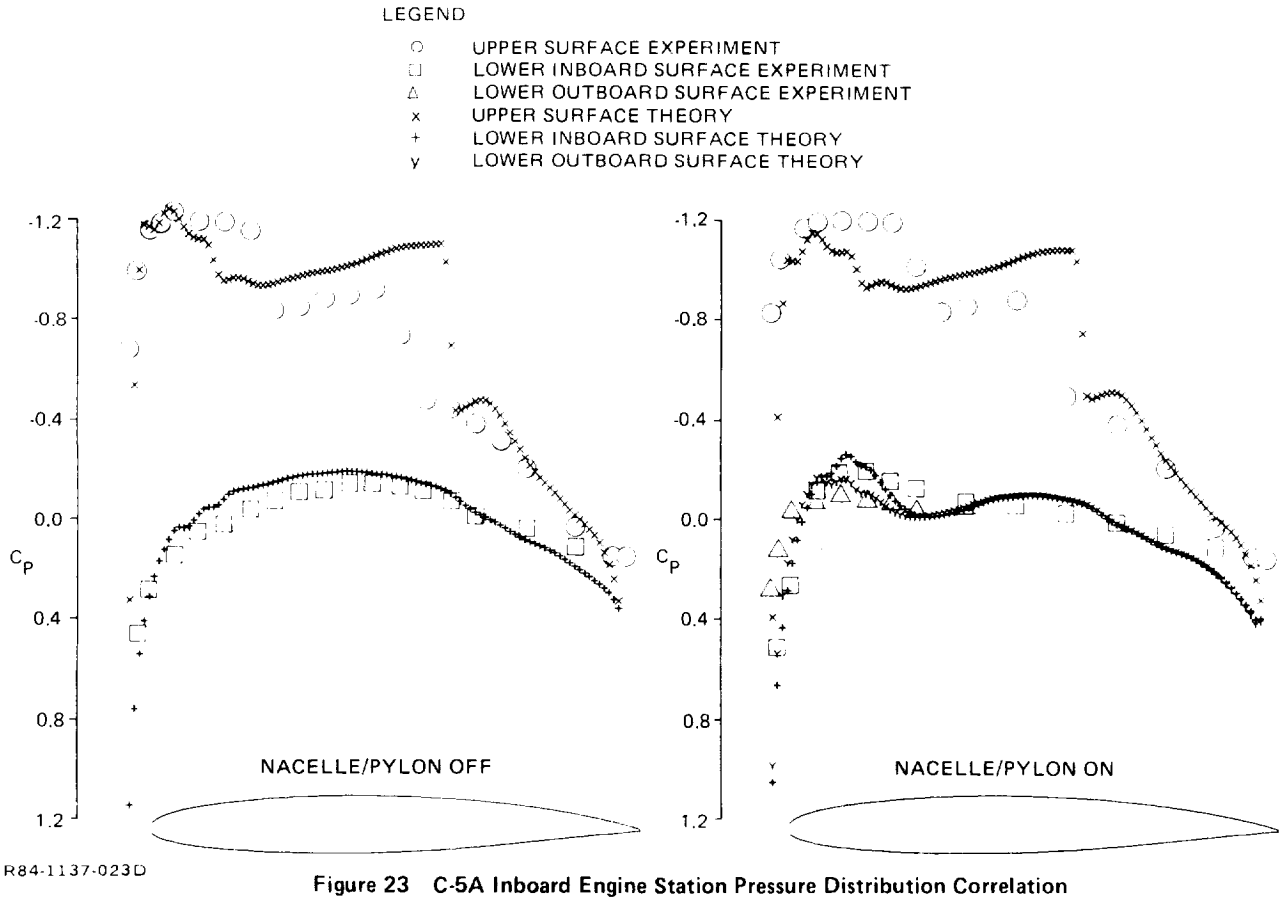

Figure 23 C-5A Inboard Engine Station Pressure Distribution Correlation
M_∞ = 0.775 α = 2° NPR = 2.84

Figure 24. Note that pylon/nacelle interference pressures are properly predicted and the multiple shock wave character is accurately reproduced. These comparisons were made for Configuration 1 in Reference 11. The P_j/P_∞ value of 1.5 converts to an NPR of 2.84.

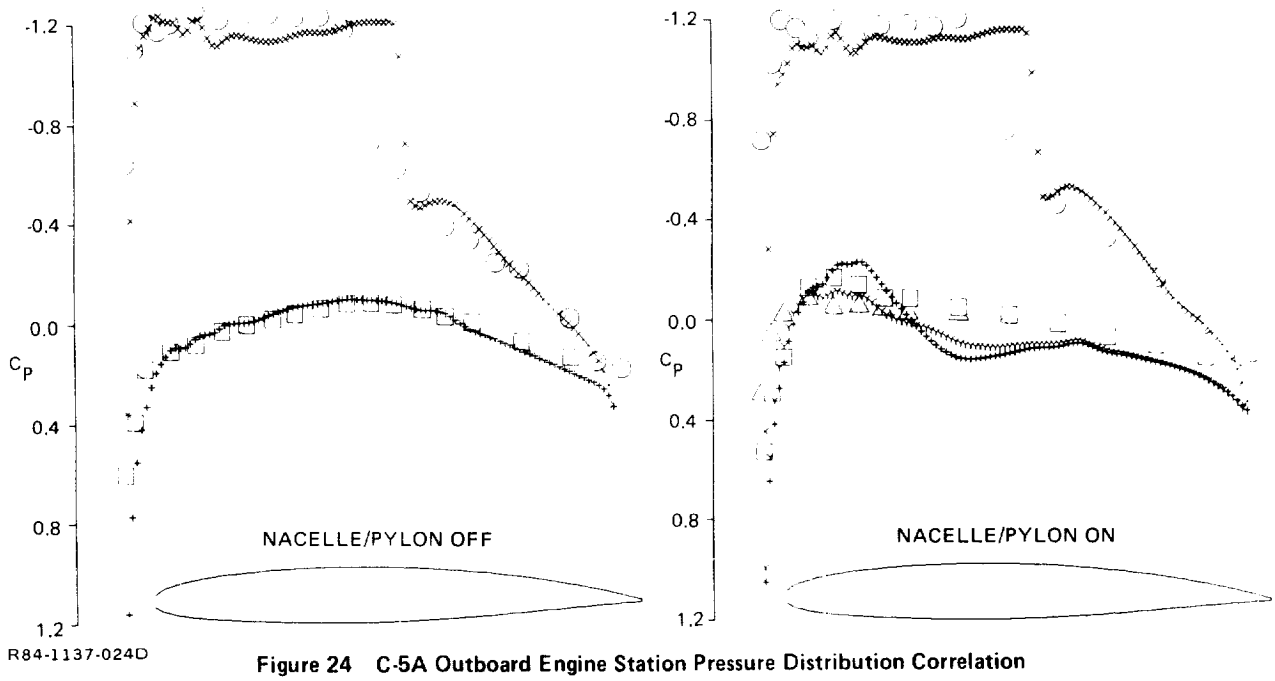

Figure 24 C-5A Outboard Engine Station Pressure Distribution Correlation
M_∞ = 0.775 α = 2° NPR = 2.84

Winglet Flow Simulations

Reference 10 provides experimental data suitable for verifying the winglet computational capability. The G-III configuration with labeled experimental pressure tap stations can be seen in Figure 25. Figure 26 illustrates the wing tip comparison for both winglet on and off. It is interesting to note that the more complex winglet/wing tip arrangement shows better agreement. This is probably caused by differences in wing tip rake for the two planforms. The analysis method cannot resolve details of the highly swept tip-leading-edge contour, thus, it predicts higher loadings in the leading edge region than those given by experiment. The winglet-on wing tip is trapezoidal in character and, therefore, in better agreement with the wing tip region computational model.

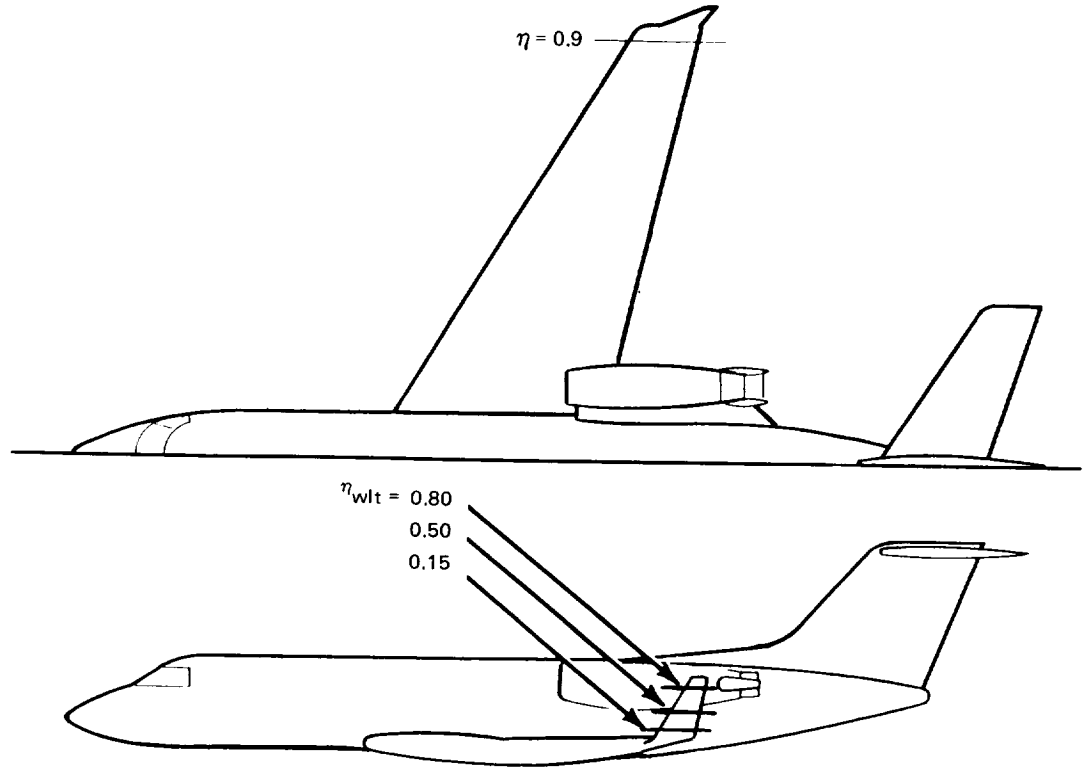

Figure 25 G-III Wing/Winglet Pressure Tap Locations for Evaluating Winglet Interference

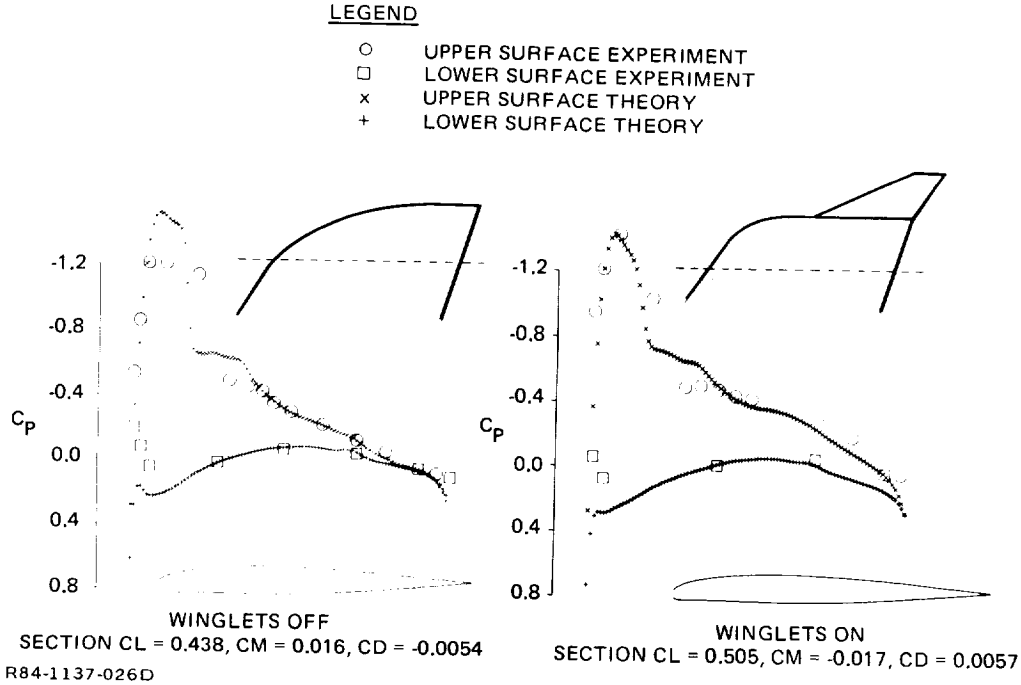

Figure 26 G-III Wing Tip Pressure Distribution Correlation $M_\infty = 0.75$ $\alpha = 4°$

Winglet pressure distribution correlations at three stations along the winglet span can be seen in Figure 27. Viscous effects are not modeled in these computations. A mild shock wave can be identified as it follows the leading edge of the winglet on the inboard side.

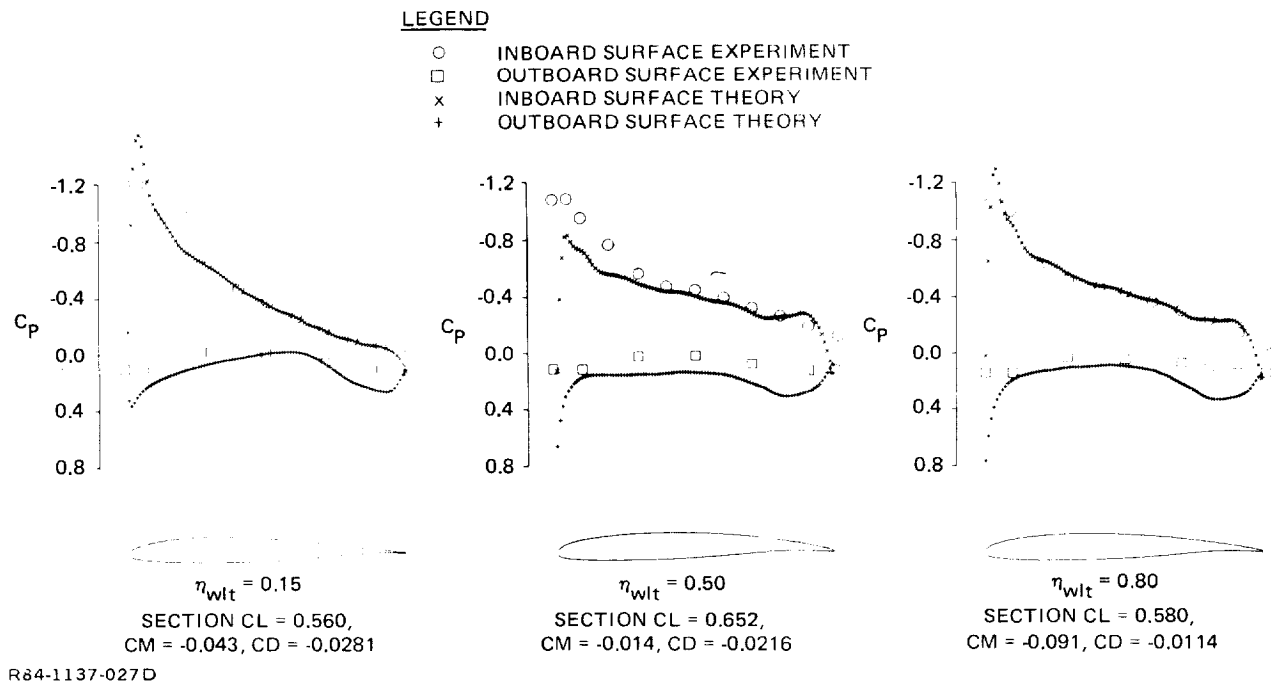

Figure 27 G-III Winglet Pressure Distribution Correlations M_∞ = 0.75 α = 4°

Combined Interference Effects

Pressure distributions across the G-III span show the good results that can be obtained after modeling all configuration components (see Figure 28). This comparison includes both wind tunnel and flight data.

The KC-135 provides an additional case that can be used for code validation (Reference 12). This configuration has four pylons, four engine nacelles, and wing-tip-mounted winglets. Pressure data is available at several wing stations and several winglet stations. Strong shock waves are not present at cruise conditions. If flow conditions are pushed beyond the cruise point, wing tip flow separation is apparent. Comparisons with experimental data at the

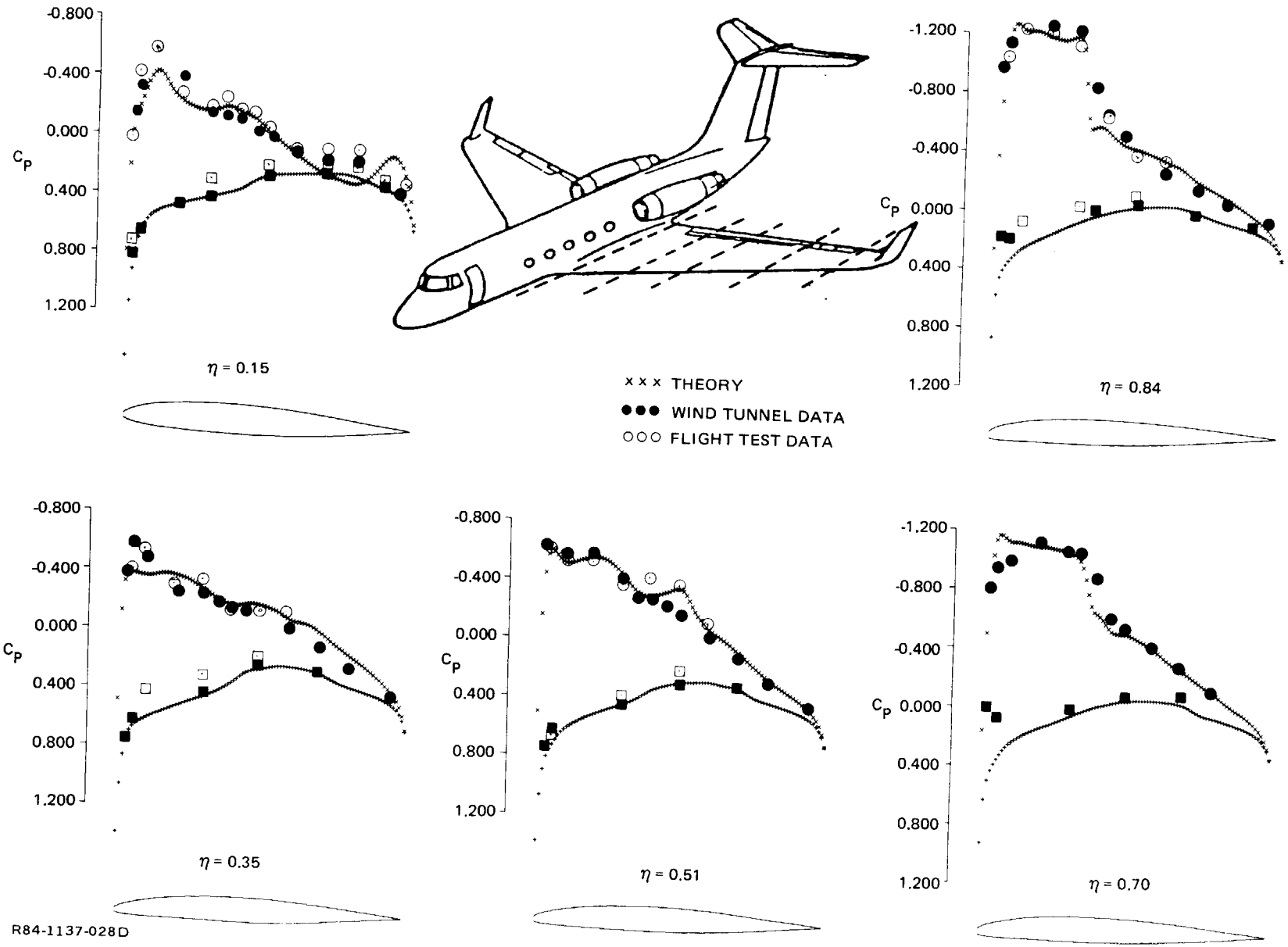

Figure 28 G-III Wing Pressure Distribution Correlation $M_\infty = 0.78$ $\alpha = 4°$

cruise point can be seen in Figure 29. It should be pointed out that the winglet is positioned at a 90 degree angle to the wing surface when modeled in the computational method. In reality, both the KC-135 and G-III winglets are canted outboard 15 degrees.

The C-141 transport configuration can be seen in Figure 30. This case is interesting because it illustrates interference effects caused by nacelles, pylons, and fuselage fairings. The fuselage geometry model, made up of body and cross-section lines, can be seen Figure 31. Wing-body juncture and landing gear fairings can be identified.

Figure 32 compares unpublished wind tunnel pressure data* taken at four wing stations. The flow condition is $M_\infty = 0.77$, $\alpha = 1.5$ degrees, and $R_e = 2 \times 10^6$. Note the analysis method angle-of-attack is 1/2 degree higher than that of the experiment. The experimental variations in flow field character which result from the addition of nacelle/pylon combinations are predicted quite well.

*Wind tunnel data obtained from M. Lores, Lockheed-Georgia Company.

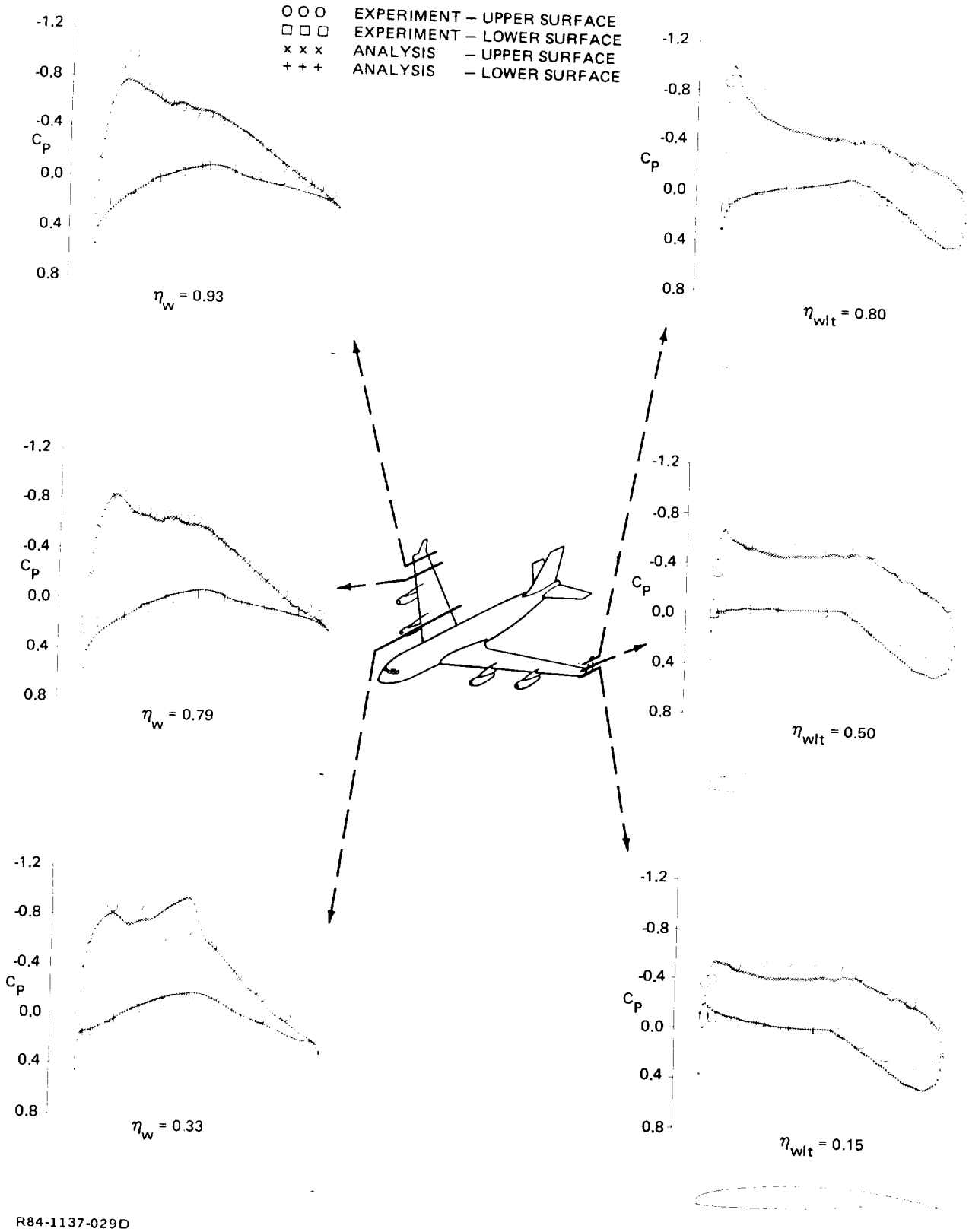

R84-1137-029D

Figure 29 Boeing KC-135 Wing & Winglet Pressure Distribution Correlations $M_\infty = 0.78$ $\alpha = 2°$

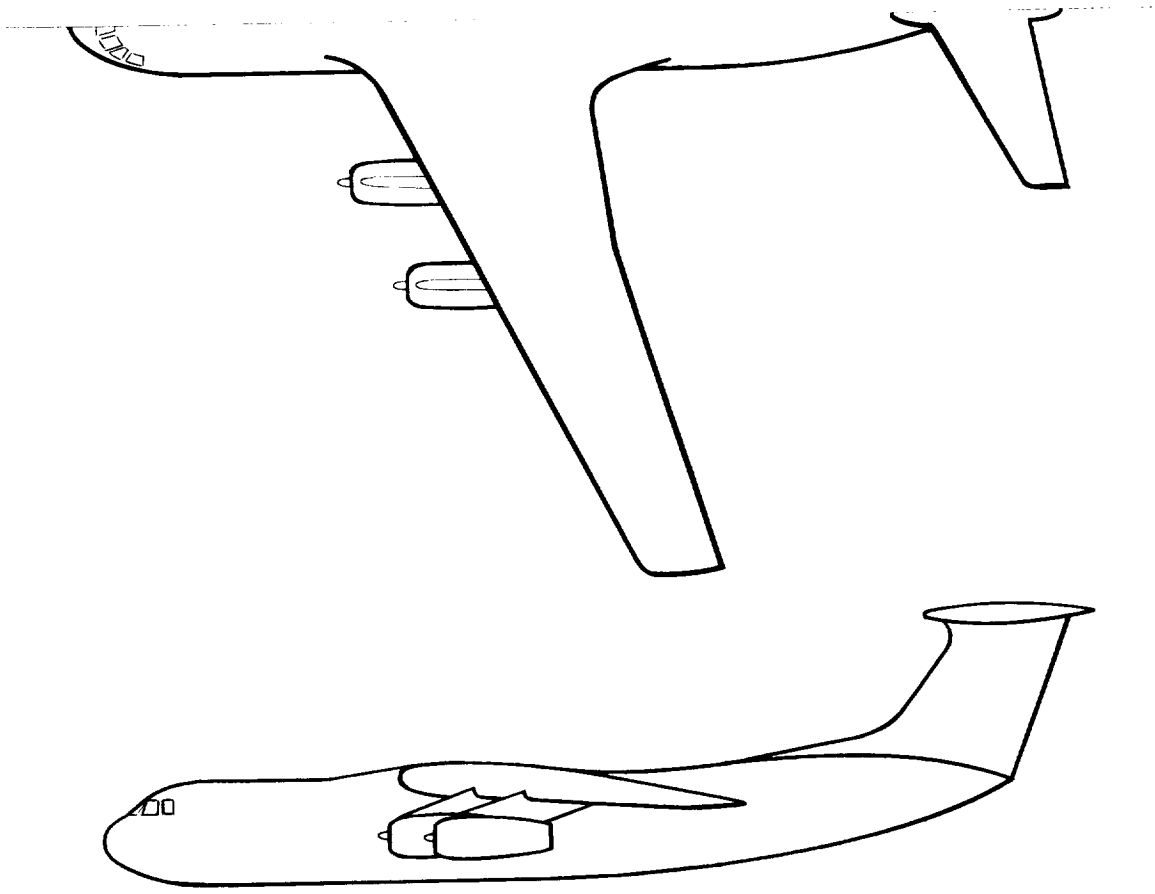

R84-1137-030D

Figure 30 C-141 Configuration

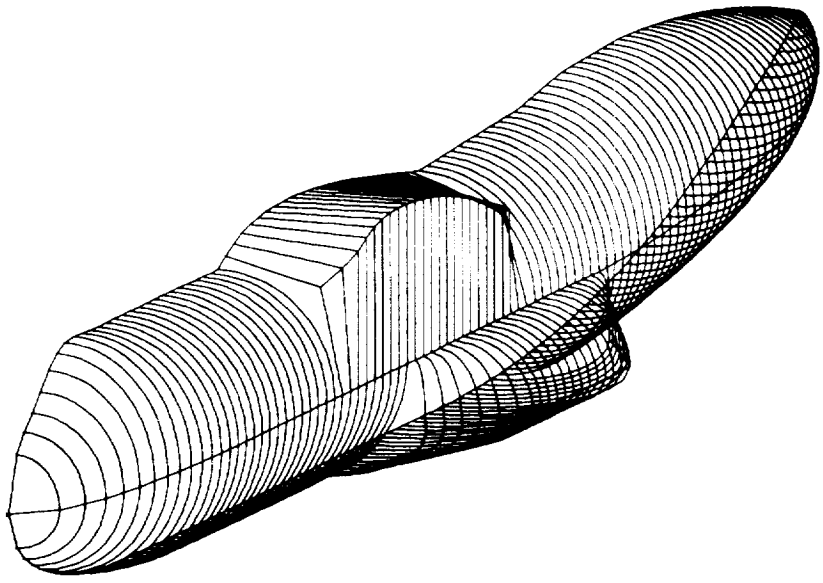

R84-1137-031D

Figure 31 C-141 Fuselage Geometry Model

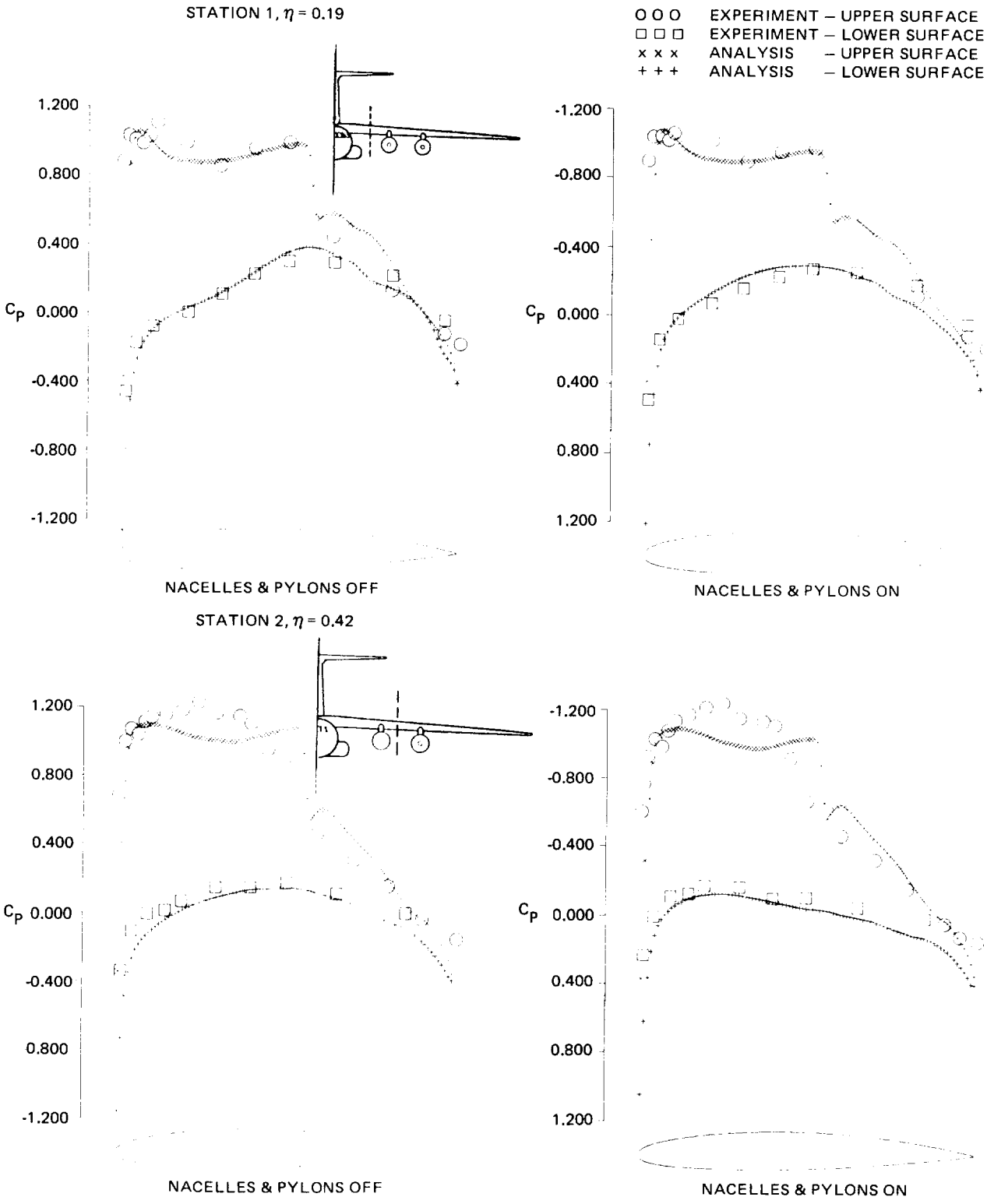

Figure 32 C-141 Wing Pressure Distribution Correlation $M_\infty = 0.77$ $\alpha = 1.2^o$ $R_e = 2 \times 10^6$ (Sheet 1 of 2)

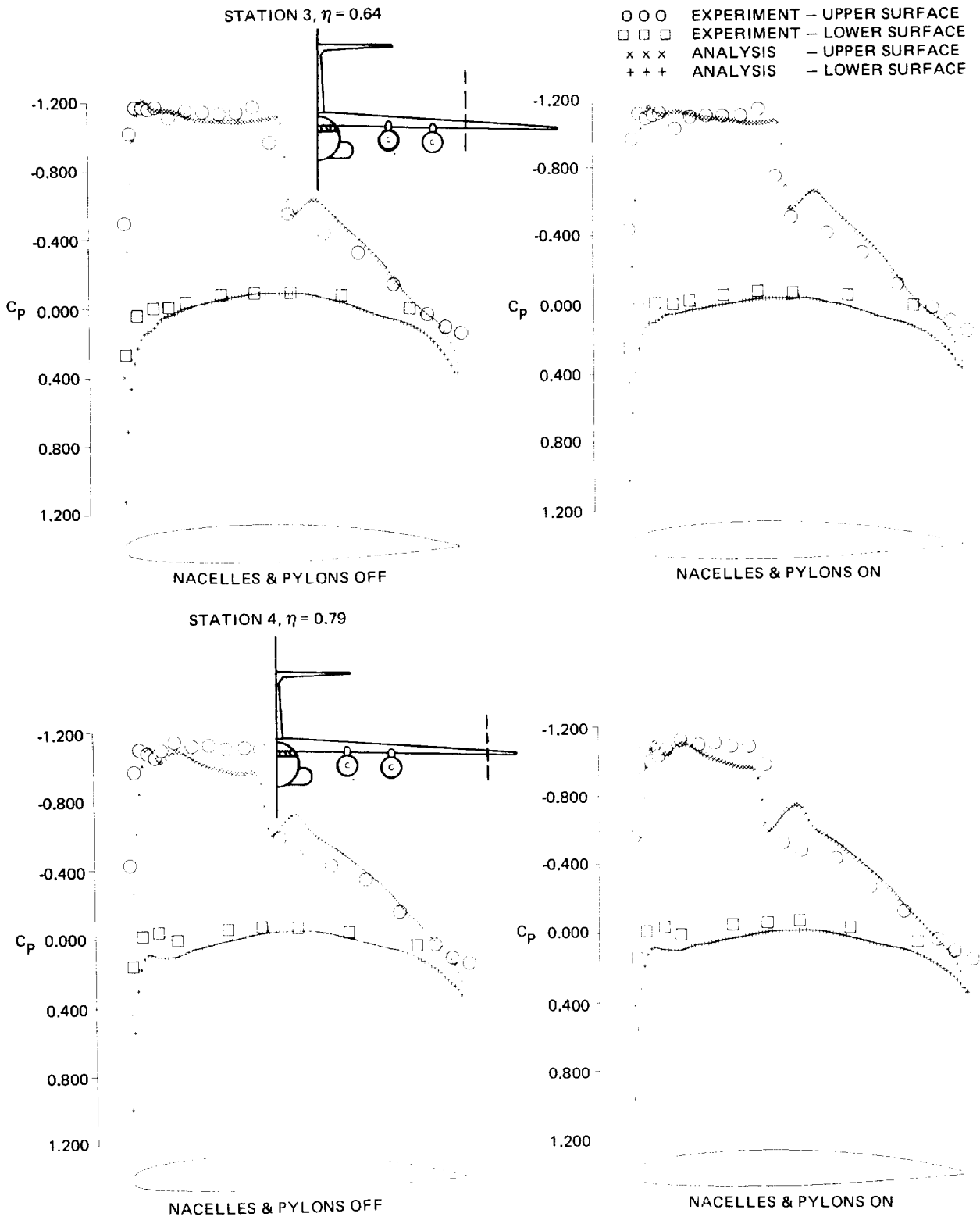

R84-1137-032D(2)

Figure 32 C-141 Wing Pressure Distribution Correlation $M_\infty = 0.77$ $\alpha = 1.2°$ $R_e = 2 \times 10^6$ (Sheet 2 of 2)

CONCLUDING REMARKS

The computational method described has been specifically developed to provide an engineering analysis for realistic aircraft configurations at transonic speeds. It is unique in its ability to treat a variety of shapes. This feature should prove to be useful in the study of aerodynamic interference effects. Compared to existing methodology, the approach provides very high computational resolution. Resolution varies between 200 boundary points for a simple airfoil to over 9000 points for a complex wing-fuselage combination with nacelles, pylons and winglets.

Method flexibility, which is required for treating a variety of complex shapes, is balanced by the simplicity of its components. Coordinate systems are essentially rectangular in character, a simple two-dimensional strip boundary layer analysis provides viscous corrections, and finally, a fast, easy to use fuselage modeling system yields arbitrary body shape surface normals. While more sophisticated components could be used, the simplicity and cost effective character of the present arrangement should enhance the probability of obtaining accurate flow simulations.

APPENDIX A

COMPUTER CODE DESCRIPTION

CONTENTS

GENERAL COMPUTER CODE DESCRIPTION

The computer code is operational on both IBM and CDC type computers*. Overlay structures are not used although this approach (for reducing core requirements) may be advantageous depending on facility charging algorithms. The IBM version using the extended H compiler (opt = 2) requires approximately $970K_{10}$ for storage and execution. There is considerable use of temporary disk storage units. Since interpolation and searching is required, a result of the mesh embedding approach, it is useful to have planar potential (ϕ) arrays separate and addressable. As a result, 15 different units are currently employed. The disk unit number and a description of contents are listed below.

DISK NUMBER	DESCRIPTION
1	Input data transferred to Unit 1 (formatted data)
8	Quick-geometry problem diagnosis printed-output
12	Global crude grid potential array
13	Fine wing grid potential array
14	Fine body/nacelle grid potential array
15	Fine winglet grid potential array
80	Crude grid wing upper/lower surface boundary conditions
81	Fine wing grid upper/lower surface boundary conditions
82	Fine wing grid x-coordinate array
83	Fine wing grid section surface ordinates
84	Crude grid body surface normal (direction cosines)
85	Fine grid body surface normal (direction cosines)
86	Fine wing grid shearing angles
87	Wing and body pressure coefficient arrays
88	Boundary layer displacement thickness slope

*This appendix describes the IBM code version whereas Appendix B gives only the modifications for the CDC code version.

Computer running time will of course vary depending on the facility and the mode of operation or operating system. The absolute levels specified may be out dated shortly after they are specified. IBM 370/3081 running times are specified below, however, since the relative increment for various options will remain essentially steady, these increments will be useful for estimating the time and cost of using different options.

CASE	TIME (CPU Minutes)
Isolated body	5 (50 crude/50 fine iterations)
Isolated wing	14 (100 crude/80 fine iterations)
Airfoil	7 (150 crude/150 fine iterations)
Isolated wing w/viscous interaction	15 (100 crude/80 fine iterations)
Wing-body (body modeled in crude grid)	15 (100 crude/80 fine iterations)
Wing body w/pod-pylon-winglet	15 (100 crude/80 fine iterations)
Wing-body (body modeled in fine grid)	20 (100 crude/80 fine iterations)
Geometry/Grid verification	1 (No iterations)

An effort has been made to minimize the amount of data required to define the configuration geometry and flow condition. This should simplify matters for most applications involving configuration analysis and reduce the chances for input errors. For example, the computational grid systems (extent and density) have been set in the FORTRAN coding to provide good results under most conditions. Occasionally, it will be advantageous to manipulate the preset values and limiters. FORTRAN coding changes will be necessary if this is the case. The following values and limiters may be modified in certain special applications:

1) Gas constant ($\gamma = 1.4$)
2) Fine wing/body embedded grid limits or extent
3) Fine wing/body embedded grid density
4) Subsonic relaxation factor ($\omega = 1.5$)
5) Boundary layer transition ($X/C_{tran} = 0.05$)
6) The number of inviscid cycles between each viscous calculation (currently set to 20)

All sample cases were computed using the basic code without modification. If code modifications of type (2) or (3) are made care must be taken to insure that common and dimensioned arrays are sufficient and consistent.

Input data format description can be found on the following pages. Descriptions are thought to be relatively straightforward except in the case of wing section definition. It is important to extend wing planform/section definition to the symmetry plane even for wing-body configurations. This serves several purposes. First, the code will compute a wing-body juncture which will be a function of both configuration geometry and the computational grid system. If the computational juncture is slightly inboard of the geometric juncture, section definition in this region becomes important. Second, the input planform shape provides both aspect ratio for the lift-induced drag computation and reference lengths and areas used to reduce integrated pressures to give force and moment coefficients. Finally, data input for defining a wing-body configuration can be used directly for the isolated wing case. This feature can be used to study wing-body interference effects.

It is important to note that provisions have been made for inputting a wing reference area. This number is used to reduce integrated pressure coefficients to provide wing or wing-fuselage total lift, drag, and moment coefficients. All other reference areas and lengths are computed from input geometry and printed at the end of the output stream. If reference values used to reduce experimental data are different than those computed by the code, then computed force and moment coefficients must be rescaled.

The computer code has been structured to permit the analyses of common aircraft configurations. There are a number of restrictions, however, that should be identified before modeling is started:

1) No boundary layer δ^* computed for winglet surfaces.
2) No differencing approximations for secondary lower surface winglet.
3) No provisions made for pylon surface attached to top of wing.
4) The fine embedded nacelle/pod grid option cannot be used along with the pylon option; crude pod and fine pylon representation only.

5) The winglet cant angle is used only to resolve force and moment coefficients. Computational winglet surfaces are always perpendicular to the wing surface.
6) The fine body grid and fine nacelle/pod grid potential arrays use the same dimensioned space. The two options cannot be implemented simultaneously.
7) In addition to the current rectangular pylon planform restriction, the computational pylon lower surface is fixed at the wing fine grid lower boundary.
8) Fuselage shoulder mounted nacelles must be positioned to allow at least one mesh cell between the nacelle and the fuselage.

An overall view of the input data sequence can be seen in Figure A-1. Figure A-2 illustrates relationships between the wing to body distance (ZWING) and the wing to pod distance (ZBODY1).

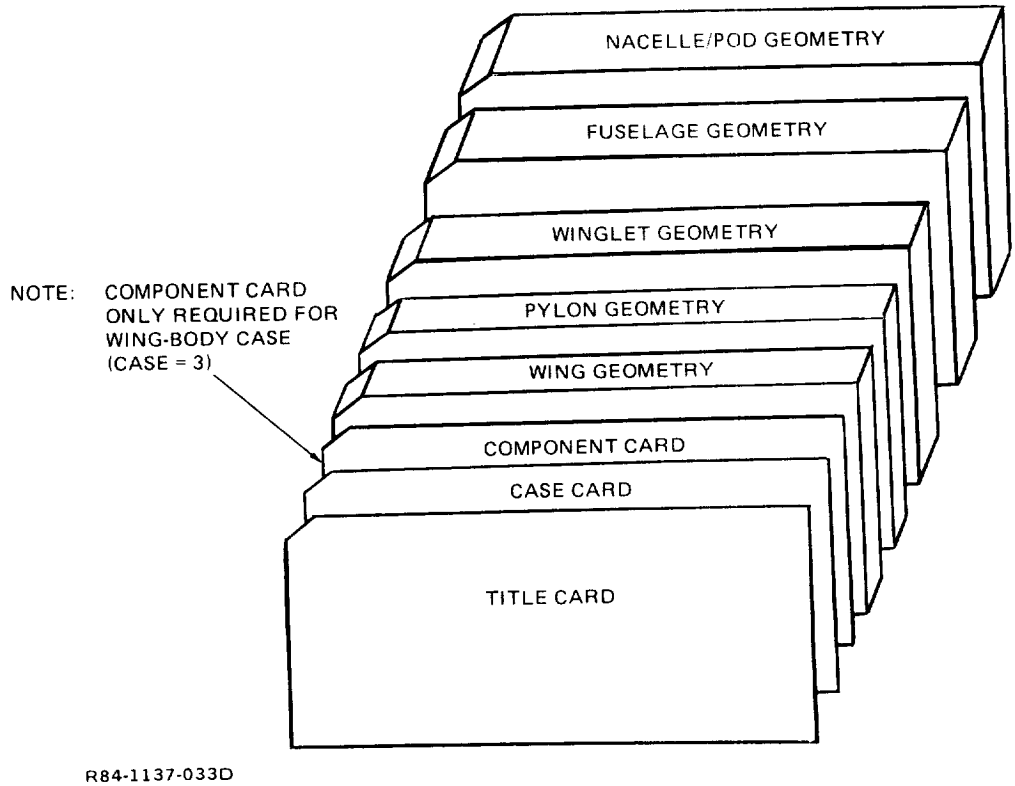

Fig. A-1 Input Data Sequence

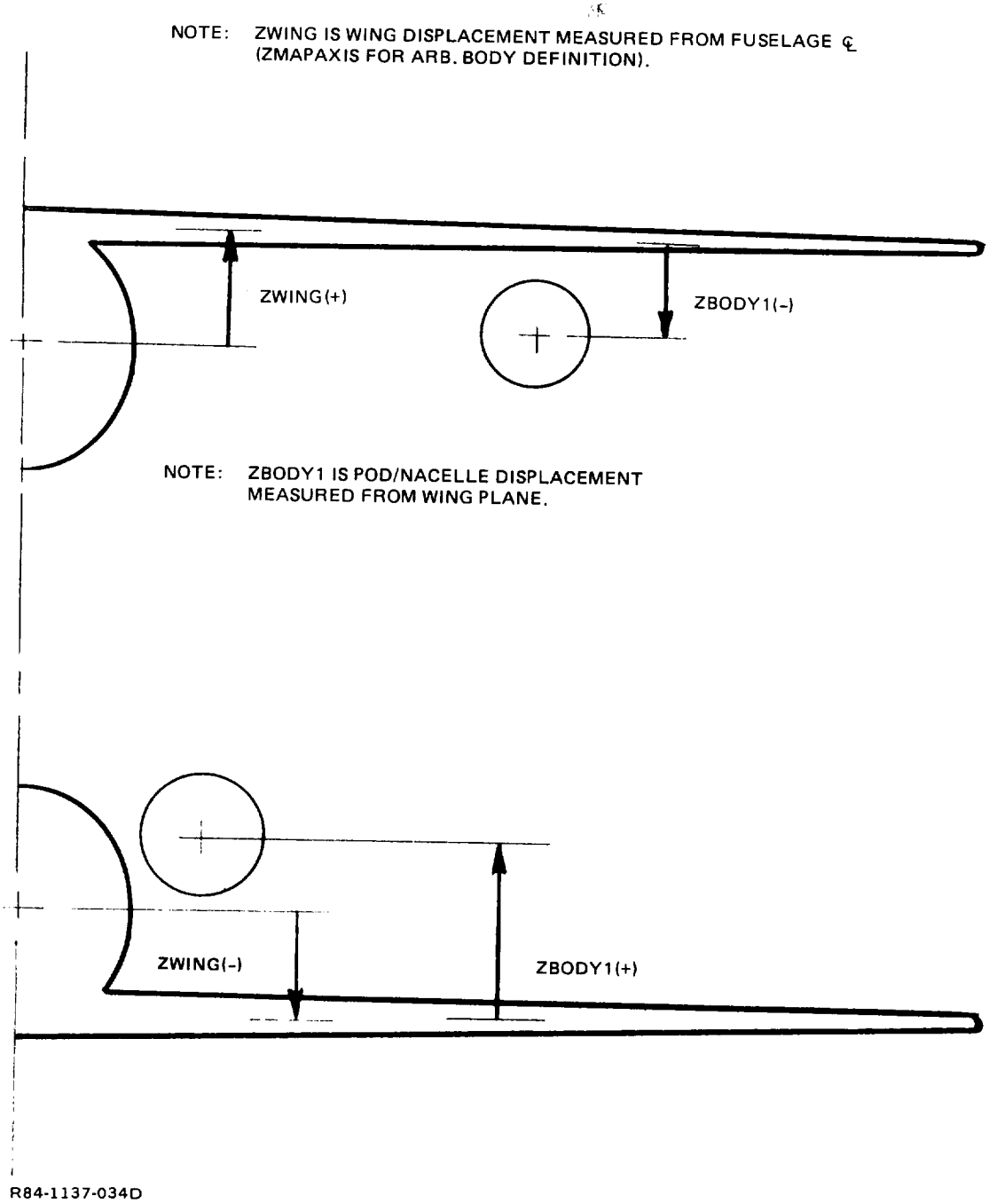

Fig. A-2 Sign Convention for Wing/Body & Wing/Nacelle Position Variables

INPUT DATA FORMAT

Excluding literal cards, all input data cards are punched* in seven field ten digit format (7F10.0). A decimal point is required in each field.

CARD NUMBER	CARD COLUMN	VARIABLE NAME	DESCRIPTION
Card 1-A	1-80	TITLE	Configuration or run title to identify graphic and printed output.
Card 2-A	1-10	CASE	CASE = 1. Isolated Body (omit cards -W) CASE = 2. Isolated Wing (omit cards -B) CASE = 3. Wing-Body
	11-20	AMACH	Mach Number (AMACH < 1.0)
	21-30	AOA	Angle-of-Attack (degrees)
	31-40	RE	Reynolds Number ($X10^6$)
	41-50	AXIT	Number of initial crude grid iterations. (AXIT = 0. for geometry verification only)
	51-60	AXITF	Number of crude/fine grid iteration cycles.
	61-70	VISMOD	VISMOD = 1. No viscous effects. VISMOD = 2. Viscous effects computed at end of inviscid analysis. VISMOD = 3. Inviscid/viscous interaction.

NOTE: Omit card 3-A for CASE = 1 or CASE = 2.

Card 3-A	1-10	PY	Number of pylons($0 \leq PY \leq 2.$)
	11-20	VER	Winglet code VER = 0. No winglet. VER = 1. Winglet definition to follow on cards WLT.
	21-30	POD	Number of pods or nacelles($0 \leq POD \leq 2.$)

NOTE: Two-dimensional airfoils can be analyzed by setting ASECT = 1 for the isolated wing CASE = 2.

*Formatted input data files are created as card images.

CARD NUMBER	CARD COLUMN	VARIABLE NAME	DESCRIPTION
NOTE: Omit card set W for CASE = 1 (card 2-A).			
Card 1-W	1-10	ASECT	Number of streamwise sections defining wing planform ($1 \leq$ ASECT ≤ 20).
	11-20	ANIN	Number of ordinates defining each wing section (ANIN ≤ 60).
	21-30	ANOSW	ANOSW = 0. Sharp nose wing sections. ANOSW = 1. Blunt nose wing sections.
	31-40	XMOM	X-position about which moment is to be computed.
	41-50	ZWING	Z-position of wing (waterline), see Fig. A-2.
	51-60	REFAR	Wing reference area.
	61-70	WS	Wing Cp distribution plot scaling per inch (typically 0.4 or 0.8).
NOTE: Card set 2-W through 5-W is repeated ASECT times.			
Card 2-W	1-10	XPL	Wing section leading edge (X-value).
	11-20	YP	Wing section span position (Y-value). First Y-value must be 0.0 (symmetry plane), even for wing-body case.
	21-30	XPT	Wing section trailing edge (X-value).
	31-40	TWIST	Wing section local incidence (twist angle in degrees).
	41-50	AKODE	AKODE = 0. Section ordinates identical to preceding section (omit cards 3-W through 5-W). AKODE = 1. New section definition expected on cards 4-W and 5-W.
	51-60	AQXFG	Number of fine X-grid points at wing tip station (default = 100). Read only on first Card 2-W.

CARD NUMBER	CARD COLUMN	VARIABLE NAME	DESCRIPTION
Card 3-W	1-70	XINW	Wing section X-coordinates (cards 3-W defined only for first wing section, ANIN values expected).
Card 4-W	1-70	YINU	Wing section upper surface Y-coordinates (ANIN values).
Card 5-W	1-70	YINL	Wing section lower surface Y-coordinates (ANIN values).

NOTE: Read Card set PY, PY times (Card 3-A).

Card 1-PY	1-80	TITLPY	Pylon title to identify printed output.
Card 2-PY	1-10	PSEC	Number of streamwise sections defining pylon planform ($2 \leq PSEC \leq 10$).
	11-20	PIN	Number of ordinates defining each pylon section ($PIN \leq 60$).
	21-30	PNOS	PNOS = 0. Sharp nose pylon sections. PNOS = 1. Blunt nose pylon sections.
	31-40	PSTA	Y - position of pylon on wing.

NOTE: Card set 3-PY through 6-PY is repeated PSEC times.

Card 3-PY	1-10	XPYL*	Pylon section leading edge (X-value).
	11-20	ZPYL*	Pylon section height (Z-value).
	21-30	XPYT*	Pylon section trailing edge.
	31-40	TPIST	Pylon section local incidence in degrees (for positive TPIST - pylon nose rotation toward centerline).

*Note: Pylon planform description used for pylon wetted area calculation (pylon skin friction) only. Planform shape is now restricted to the boundaries of the wing fine grid system below the wing.

CARD NUMBER	CARD COLUMN	VARIABLE NAME	DESCRIPTION
Card 3-PY (contd)	41-50	PKOD	PKOD = 0. Section ordinates identical to preceding section (omit cards 5-PY and 6-PY). PKOD = 1. New section definition to follow.
Card 4-PY	1-70	XINP	Pylon section X-ordinates (cards 4-PY defined only for first pylon section, PIN values expected).
Card 5-PY	1-70	YINUP	Pylon section inboard surface coordinates (PIN values).
Card 6-PY	1-70	YINLP	Pylon section outboard surface coordinates (PIN values).

NOTE: Omit card set WLT for WLT = 0 (Card 3-A).

Card 1-WLT	1-80	TITLW	Winglet title
Card 2-WLT	1-10	VSEC	Number of streamwise sections defining winglet planform ($2 \leq VSEC \leq 10$).
	11-20	VIN	Number of ordinates defining each winglet section ($VIN \leq 60$).
	21-30	VNOS	VNOS = 0. Sharp nose winglet sections. VNOS = 1. Blunt nose winglet sections.
	31-40	VANGL	Winglet cant angle in degrees (for positive VANGL - winglet rotation upward from wing plane).

CARD NUMBER	CARD COLUMN	VARIABLE NAME	DESCRIPTION
NOTE: Card set 3-WLT through 6-WLT is repeated VSEC times.			
Card 3-WLT	1-10	XVL	Winglet section leading edge.
	11-20	YV	Winglet section span position (Note: Winglet is defined in plane of wing).
	21-30	XVT	Winglet section trailing edge.
	31-40	TVIST	Winglet section local incidence in degrees (for positive TVIST, winglet nose rotated toward centerline).
	41-50	VKOD	VKOD = 0. Section ordinates identical to preceding section (omit cards 5-WLT to 6-WLT). VKOD = 1. New section definition to follow.
Card 4-WLT	1-70	XINV	Winglet section X-ordinates (cards 4-WLT defined for first winglet section only, VIN values expected).
Card 5-WLT	1-70	YINUV	Winglet section inboard surface ordinates (VIN values).
Card 6-WLT	1-70	YINLV	Winglet section outboard surface ordinates (VIN values).
NOTE: Omit Card set B for CASE = 2 (Card 2-A).			
Card 1-B	1-10	BKOD = 1.	Infinite cylinder (only RADIUS need be input).
		BKOD = -1.	Same as BKOD = 1. No embedded body grid. Crude grid body representation only.
		BKOD = 2.	Simple axisymmetric body definition requested (input XINB, RIN on card(s) 2-B and 3-B).

CARD NUMBER	CARD COLUMN	VARIABLE NAME	DESCRIPTION
Card 1-B (contd)			BKOD = -2. Same as BKOD = 2. No embedded body grid. Crude grid body representation only.
			BKOD = 3. Complex body definition requested (input Quick-Geometry model on card(s) 4-B through 13-B).
			BKOD = -3. Same as BKOD = 3. No embedded body grid. Crude grid body representation only.
	11-20	BNOSE	Body nose (X-value) } For BKOD = ±2. or ±3.
	21-30	BTAIL	Body tail (X-value) }
	31-40	BNIN	Number of axisymmetric body coordinates to be input for BKOD = ±2 only (BNIN ≤ 60).
	41-50	RADIUS	Cylinder radius for BKOD = ±1 only.
	51-60	ANOSB	ANOSB = 0. Sharp nose body } BKOD = ±2 only.
			ANOSB = 1. Blunt nose body }
	61-70	BS	Body Cp plot scaling per inch (typically 0.08).
			NOTE: Omit card sets 2-B and 3-B for BKOD = ±1 or BKOD = ±3.
Card(s) 2-B	1-70	XINB	Axisymmetric body X-coordinates (BNIN values).
Card(s) 3-B	1-70	RIN	Axisymmetric body radii (BNIN values).
			NOTE: Omit card sets 4-B through 13-B for BKOD = ±1 or BKOD = ±2.
Card 4-B	1-70	VTITLE	Quick-Geometry model title.
Card 5-B	1-10	ACSM	Number of distinct cross-section models (1 ≤ ACSM ≤ 10). (ACSM card sets 6-B and 7-B will follow).

CARD NUMBER	CARD COLUMN	VARIABLE NAME	DESCRIPTION
Card 6-B	1-10	ADUM	Running count of current cross-section model (1-ACSM).
	11-20	AARC	Number of arcs in current cross-section model (1 ≤ AARC ≤ 10). (AARC Card(s) 7-B will follow).
	21-60	CTITLE	Title or descriptor of current cross-section model.
Card 7-B	1-8	ARCNAM	Arc or component name.
	11-14	ASHAPE	Arc or component shape.
	21-28	PNTNAM(1)	Control point name for beginning of this arc.
	31-38	PNTNAM(2)	Control point name for termination of this arc.
	41-48	PNTMAN(3)	Slope control point name for this arc, if required.
Card 8-B	1-10	ANTCSM	Number of cross-section models to define entire body (1 ≤ ANTCSM ≤ 10). (ANTCSM card(s) 9-B will follow).
Card 9-B	1-10	ADUM	Running count of current cross-section model (1-ANTCSM)
	11-20	AMODEL	Index corresponding to already defined cross-section models (between 1 and ACSM).
	21-30	XCSMS1	Starting X-station for current cross-section model.
	31-40	XCSMS2	Ending X-station for current cross-section model.
Card 10-B	1-10	BLINE	Number of body line models to be defined by segments (1 ≤ BLINE ≤ 25). (BLINE card sets 11-B and 12-B follow).
	11-20	ALIAS	Number of body line models to be aliased (1 ≤ ALIAS ≤ 25). (ALIAS card(s) 13-B follow).

CARD NUMBER	CARD COLUMN	VARIABLE NAME	DESCRIPTION
Note: Card set 11-B and 12-B is repeated BLINE times.			
Card 11-B	1-10	BLSEG	Number of segment(s) defining body line model ($1 \leq$ BLSEG ≤ 10).
	11	BYORZ	The letter Y or Z indicates which data definition is to follow.
	12-19	BNAME	Body line name to be defined.
Card 12-B	1-4	SSHAPE	Segment shape.
	11-20	D(1)	X-station for beginning of segment.
	21-30	D(2)	Y or Z value corresponding to D(1).
	31-40	D(3)	X-station for termination of segment.
	41-50	D(4)	Y or Z value corresponding to D(3).
	51-60	D(5)	X-station for segment slope control point.
	61-70	D(6)	Y or Z value corresponding to D(5)
Note: Card set 13-B is repeated ALIAS times.			
Card 13-B	11	BYORZ	The letter Y or Z indicates which data definition is to follow.
	12-19	BNAME	Body line name to be defined.
	21	AYORZ	The letter Y or Z indicates which definition is to be used for aliasing.
	22-29	ANAME	Body line name to which BNAME is aliased.
NOTE: Read Card set POD, POD times (Card 3-A).			
Card 1-POD	1-70	TITLEP	Pod/nacelle title to identify graphic and printed output.

CARD NUMBER	CARD COLUMN	VARIABLE NAME	DESCRIPTION
Card 2-POD	1-10	PTYPE	PTYPE = 0. Closed body (pod, tank, etc.). PTYPE = 1. Engine nacelle - cold jet. } FMFR PTYPE =-1. Engine nacelle - hot jet. } and FNPR expected on Card 3-POD.
	11-20	BNOSE1	Pod nose (X-position).
	21-30	BTAIL1	Pod tail (X-position).
	31-40	YBODY1	Pod span position (Y-position).
	41-50	ZBODY1	Pod height (Z-position).
	51-60	BNIN1	Number of coordinates defining pod geometry (BNIN1 ≤ 30).
	61-70	ANOSB1	ANOSB1 = 0. Sharp nose pod. ANOSB1 = 1. Blunt nose pod.
Card 3-POD	1-10	BODALF	Pod angle-of-attack.
	11-20	BODBET	Pod yaw angle (positive-nose of pod away from centerline).
	21-30	FIFP	Pod embedded grid code FIFP = 0. Pod FIFP = 0. crude grid only. FIFP = 1. Fine pod grid used.
	31-40	FMFR	Engine inlet mass flow ratio, MFR.
	41-50	FNPR	Engine nozzle pressure ratio, NPR.
Card 4-POD	1-70	XINBP	Axisymmetric pod non-dimensional X-ordinates (BNIN1 values).
Card 5-POD	1-70	RINP	Axisymmetric pod non-dimensional radii (BNIN1 values).

SAMPLE INPUT DATA SETS

```
NACA 0012 AIRFOIL
2.          0.804       1.94        3.00        150 .       150.        3.0
1.          56.         1.0         0.25        0.          1.          0.4
0.          0.          100.0       0.          0.
    0.0         0.00200     0.00500     0.01000     0.02000     0.03000     0.04000
    0.05000     0.06000     0.08000     0.10000     0.12000     0.14000     0.16000
    0.18000     0.20000     0.22000     0.24000     0.26000     0.28000     0.30000
    0.32000     0.34000     0.36000     0.38000     0.40000     0.42000     0.44000
    0.46000     0.48000     0.50000     0.52000     0.54000     0.56000     0.58000
    0.60000     0.62000     0.64000     0.66000     0.68000     0.70000     0.72000
    0.74000     0.76000     0.78000     0.80000     0.82000     0.84000     0.86000
    0.88000     0.90000     0.92000     0.94000     0.96000     0.98000     1.00000
    0.0         0.00780     0.01210     0.01690     0.02350     0.02830     0.03220
    0.03540     0.03830     0.04300     0.04670     0.04980     0.05230     0.05440
    0.05610     0.05740     0.05840     0.05910     0.05960     0.06000     0.06010
    0.06000     0.05980     0.05940     0.05880     0.05810     0.05730     0.05640
    0.05540     0.05420     0.05300     0.05170     0.05030     0.04890     0.04720
    0.04570     0.04410     0.04230     0.04050     0.03870     0.03670     0.03480
    0.03270     0.03070     0.02850     0.02630     0.02410     0.02180     0.01940
    0.01700     0.01450     0.01200     0.00950     0.00680     0.00420     0.00150
    0.0        -0.00780    -0.01210    -0.01690    -0.02350    -0.02830    -0.03220
   -0.03540    -0.03830    -0.04300    -0.04670    -0.04980    -0.05230    -0.05430
   -0.05600    -0.05730    -0.05830    -0.05900    -0.05950    -0.05990    -0.06000
   -0.05990    -0.05970    -0.05920    -0.05860    -0.05800    -0.05720    -0.05630
   -0.05530    -0.05420    -0.05280    -0.05160    -0.05020    -0.04870    -0.04720
   -0.04560    -0.04400    -0.04220    -0.04040    -0.03860    -0.03660    -0.03470
   -0.03260    -0.03060    -0.02840    -0.02620    -0.02400    -0.02160    -0.01920
   -0.01680    -0.01440    -0.01190    -0.00930    -0.00670    -0.00400    -0.00130
```

```
NASA AIRFOIL LS1
2.          0.722       -1.50       4.96        150 .       150.        3.0
1.          38.         1.0         0.25        0.          1.          0.4
0.          0.          100.0       0.          0.
   0.0         0.20000     0.50000     1.25000     2.50000     3.75000     5.00000
   7.50000    10.00000    12.50000    15.00000    17.50000    19.99998    25.00000
  30.00000    35.00000    39.99998    44.99998    50.00000    55.00000    57.49998
  60.00000    62.50000    64.99998    67.50000    69.99998    72.50000    75.00000
  77.49998    80.00000    82.49998    85.00000    87.50000    89.99998    92.50000
  94.99998    97.50000   100.00000
   0.0         1.03000     1.63000     2.46000     3.36000     4.00000     4.51000
   5.28000     5.88000     6.37000     6.77000     7.12000     7.42000     7.88000
   8.20000     8.40000     8.49000     8.46000     8.33000     8.07000     7.89000
   7.67000     7.39000     7.08000     6.72000     6.33000     5.91000     5.45000
   4.97000     4.47000     3.95000     3.41000     2.85000     2.28000     1.70000
   1.10000     0.49000    -0.15000
   0.0        -0.66000    -0.97000    -1.44000    -1.88000    -2.23000    -2.50000
  -2.94000    -3.28000    -3.57000    -3.80000    -3.98000    -4.15000    -4.38000
  -4.49000    -4.52000    -4.49000    -4.37000    -4.17000    -3.86000    -3.62000
  -3.37000    -3.07000    -2.76000    -2.43000    -2.10000    -1.75000    -1.43000
  -1.10000    -0.78000    -0.51000    -0.28000    -0.12000     0.0         0.01000
  -0.07000    -0.28000    -0.71000
```

```
KC-135 TRANSPORT WITH PODS, PYLONS, AND WINGLETS
3.          0.78        2.0         5.25        100.        80.         1.
2.          1.          2.
6.          26.         0.          52.90       -4.25       1440.0      0.8
28.66       0.0         70.27       2.22        1.0
0.          0.5         0.75        1.25        2.50        5.0         7.5
10.         15.         20.         25.         30.         35.         40.
45.         50.         55.         60.         65.         70.         75.
80.         85.         90.         95.         100.
0.740       1.750       2.055       2.539       3.470       4.830       5.813
6.572       7.661       8.380       8.860       9.137       9.218       9.105
8.766       8.258       7.620       6.870       6.029       5.168       4.300
3.445       2.584       1.723       0.861       0.
0.000       -0.872      -1.076      -1.390      -1.915      -2.613      -3.178
-3.665      -4.510      -5.228      -5.757      -6.104      -6.275      -6.250
-6.044      -5.678      -5.185      -4.618      -4.041      -3.464      -2.886
-2.309      -1.732      -1.155      -0.577      0.
32.02       4.37        62.89       2.02        0.
36.38       10.36       57.86       1.75        1.
0.536       1.399       1.654       2.060       2.840       3.998       4.850
5.511       6.436       7.070       7.500       7.760       7.920       7.910
7.725       7.382       6.895       6.284       5.570       4.782       3.985
3.188       2.391       1.594       0.797       0.
0.000       -0.733      -0.895      -1.123      -1.475      -1.915      -2.290
-2.646      -3.318      -3.925      -4.401      -4.746      -4.980      -5.070
-5.007      -4.793      -4.448      -3.995      -3.496      -2.996      -2.497
-1.998      -1.498      -0.999      -0.499      0.
41.41       16.73       59.20       1.46        1.0
0.374       1.123       1.340       1.687       2.350       3.360       4.114
4.699       5.530       6.047       6.422       6.666       6.805       6.829
6.736       6.509       6.136       5.643       5.049       4.380       3.687
2.929       2.197       1.465       0.732       0.
0.000       -0.570      -0.684      -0.837      -1.053      -1.307      -1.544
-1.787      -2.265      -2.731      -3.118      -3.425      -3.642      -3.763
-3.782      -3.696      -3.487      -3.174      -2.787      -2.389      -1.991
-1.593      -1.194      -0.796      -0.398      0.
50.81       29.30       64.90       0.70        1.0
0.306       0.997       1.198       1.519       2.160       3.130       3.857
4.423       5.210       5.704       6.050       6.280       6.430       6.449
6.370       6.178       5.850       5.412       4.880       4.267       3.605
2.904       2.178       1.452       0.726       0.
0.000       -0.465      -0.558      -0.657      -0.750      -0.895      -1.041
-1.187      -1.479      -1.770      -2.059      -2.275      -2.445      -2.543
-2.568      -2.501      -2.330      -2.078      -1.818      -1.558      -1.299
-1.039      -0.775      -0.520      -0.260      0.
69.27       53.96       77.27       -1.0        0.
INBOARD PYLON
2.          26.         1.0         22.12
0.          -19.0       1.0         0.          1.0
0.          0.5         0.75        1.25        2.50        5.0         7.5
10.0        15.0        20.0        25.0        30.0        35.0        40.0
45.0        50.0        55.0        60.0        65.0        70.0        75.0
80.0        85.0        90.0        95.0        100.0
0.          0.50        0.90        1.15        1.70        2.36        2.82
3.24        3.86        4.34        4.66        4.90        5.02        5.02
4.90        4.64        4.30        3.88        3.40        2.88        2.34
1.76        1.22        0.7         0.26        0.
0.          -0.50       -0.90       -1.15       -1.70       -2.36       -2.82
-3.24       -3.86       -4.34       -4.66       -4.90       -5.02       -5.02
-4.90       -4.64       -4.30       -3.88       -3.40       -2.88       -2.34
-1.76       -1.22       -0.7        -0.26       0.
0.          0.          1.0         0.          0.
OUTBOARD PYLON
2.          26.         1.0         38.00
0.          -25.0       1.0         0.          1.0
0.          0.5         0.75        1.25        2.50        5.0         7.5
10.0        15.0        20.0        25.0        30.0        35.0        40.0
45.0        50.0        55.0        60.0        65.0        70.0        75.0
80.0        85.0        90.0        95.0        100.0
0.          0.50        0.90        1.15        1.70        2.36        2.82
3.24        3.86        4.34        4.66        4.90        5.02        5.02
4.90        4.64        4.30        3.88        3.40        2.88        2.34
1.76        1.22        0.7         0.26        0.
0.          -0.50       -0.90       -1.15       -1.70       -2.36       -2.82
-3.24       -3.86       -4.34       -4.66       -4.90       -5.02       -5.02
-4.90       -4.64       -4.30       -3.88       -3.40       -2.88       -2.34
-1.76       -1.22       -0.7        -0.26       0.
0.          0.          1.0         0.          0.
```

```
KC-135 WINGLET
2.          38.         1.0         75.0
72.07       53.96       77.27       -4.0        1.0
0.          0.2         0.5         1.25        2.50        3.75        5.00
7.50        10.0        12.5        15.0        17.5        20.0        25.0
30.0        35.0        40.0        45.0        50.0        55.0        57.5
60.0        62.5        65.0        67.5        70.0        72.5        75.0
77.5        80.0        82.5        85.0        87.5        90.0        92.5
95.0        97.5        100.0
0.          0.77        1.19        1.79        2.49        2.96        3.33
3.89        4.33        4.69        4.99        5.25        5.47        5.81
6.05        6.21        6.28        6.27        6.18        5.99        5.87
5.72        5.54        5.33        5.08        4.81        4.51        4.19
3.84        3.49        3.11        2.70        2.28        1.84        1.38
0.89        0.38        -0.20
0.          -0.31       -0.41       -0.60       -0.77       -0.90       -1.00
-1.18       -1.32       -1.44       -1.54       -1.61       -1.67       -1.75
-1.76       -1.74       -1.68       -1.58       -1.44       -1.22       -1.06
-0.90       -0.71       -0.52       -0.33       -0.15       0.04        0.20
0.36        0.49        0.60        0.65        0.64        0.59        0.45
0.21        -0.13       -0.67
78.32       61.96       80.00       -4.0        0.0
-2.         0.00        108.30      22.         5.04        1.          .4
0.          2.0         4.0         6.0         8.0         10.0        12.0
14.0        16.0        20.0        30.0        40.0        50.0        60.0
70.0        78.0        80.0        85.0        90.0        95.0        100.0
108.3
0.          2.50        3.35        3.90        4.30        4.60        4.80
4.95        5.04        5.04        5.04        5.04        5.04        5.04
5.04        5.04        4.92        4.65        4.20        3.55        2.65
2.60
KC135A INBOARD ENGINE NACELLE
0.          33.464      45.610      22.05       -3.816      17.         0.
2.          0.          0.          0.          0.
0.          0.58        1.81        4.61        7.57        10.37       16.14
21.90       27.66       39.19       43.31       50.72       62.24       79.53
91.06       96.82       100.0
9.72        10.21       10.87       11.69       12.35       12.84       13.50
13.83       14.16       14.00       14.16       14.00       13.67       11.94
10.04       8.40        7.41
KC135A OUTBOARD ENGINE NACELLE
0.          45.840      57.986      38.15       -3.816      17.         0.
2.          0.          0.          0.          0.
0.          0.58        1.81        4.61        7.57        10.37       16.14
21.90       27.66       39.19       43.31       50.72       62.24       79.53
91.06       96.82       100.0
9.72        10.21       10.87       11.69       12.35       12.84       13.50
13.83       14.16       14.00       14.16       14.00       13.67       11.94
10.04       8.40        7.41
```

```
GULFSTREAM III CONFIGURATION WITH WINGLET AND NACELLE
3.          0.780       4.00        3.10        100.        80.         1.0
0.          1.          1.
14.         26.         1.0         451.3       -47.0       134582.4    0.6
275.0       0.          508.72      0.0         1.0
    0.0         0.00500     0.00750     0.01250     0.02500     0.05000     0.07500
    0.10000     0.15000     0.20000     0.25000     0.30000     0.35000     0.40000
    0.45000     0.50000     0.55000     0.60000     0.65000     0.70000     0.75000
    0.80000     0.85000     0.90000     0.95000     1.00000
   -0.05467    -0.04646    -0.04435    -0.04088    -0.03409    -0.02419    -0.01713
   -0.01245    -0.00905    -0.00845    -0.00902    -0.01059    -0.01369    -0.01760
   -0.02274    -0.02857    -0.03483    -0.04147    -0.04846    -0.05585    -0.06385
   -0.07309    -0.08260    -0.09212    -0.10163    -0.11114
   -0.05467    -0.06342    -0.06548    -0.06876    -0.07480    -0.08334    -0.08974
   -0.09489    -0.10287    -0.10912    -0.11465    -0.11965    -0.12419    -0.12819
   -0.13145    -0.13344    -0.13438    -0.13447    -0.13398    -0.13299    -0.13151
   -0.12940    -0.12634    -0.12234    -0.11750    -0.11150
302.7       45.0        519.7       0.0         1.0
   -0.06251    -0.05440    -0.05240    -0.04908    -0.04276    -0.03373    -0.02726
   -0.02281    -0.01835    -0.01672    -0.01651    -0.01725    -0.01905    -0.02224
   -0.02643    -0.03161    -0.03744    -0.04390    -0.05090    -0.05848    -0.06670
   -0.07555    -0.08430    -0.09277    -0.10112    -0.10947
   -0.06251    -0.07061    -0.07249    -0.07551    -0.08106    -0.08880    -0.09450
   -0.09900    -0.10588    -0.11137    -0.11608    -0.12020    -0.12382    -0.12697
   -0.12963    -0.13143    -0.13217    -0.13214    -0.13149    -0.13026    -0.12848
   -0.12603    -0.12275    -0.11895    -0.11473    -0.10984
321.2       75.0        526.9       0.0         1.0
   -0.06846    -0.06048    -0.05856    -0.05540    -0.04943    -0.04099    -0.03498
   -0.03067    -0.02556    -0.02323    -0.02245    -0.02275    -0.02382    -0.02618
   -0.02970    -0.03434    -0.03976    -0.04588    -0.05279    -0.06044    -0.06884
   -0.07764    -0.08605    -0.09375    -0.10098    -0.10821
   -0.06846    -0.07600    -0.07775    -0.08055    -0.08568    -0.09275    -0.09783
   -0.10172    -0.10771    -0.11242    -0.11640    -0.11986    -0.12294    -0.12573
   -0.12822    -0.12984    -0.13047    -0.13033    -0.12952    -0.12813    -0.12612
   -0.12339    -0.12015    -0.11659    -0.11277    -0.10858
328.0       86.0        529.6       0.0         1.0
   -0.07081    -0.06289    -0.06099    -0.05790    -0.05208    -0.04391    -0.03804
   -0.03377    -0.02847    -0.02586    -0.02487    -0.02497    -0.02590    -0.02787
   -0.03113    -0.03550    -0.04072    -0.04669    -0.05350    -0.06110    -0.06947
   -0.07817    -0.08637    -0.09368    -0.10070    -0.10771
   -0.07080    -0.07812    -0.07981    -0.08250    -0.08746    -0.09424    -0.09900
   -0.10266    -0.10825    -0.11263    -0.11633    -0.11957    -0.12250    -0.12519
   -0.12767    -0.12922    -0.12980    -0.12961    -0.12874    -0.12727    -0.12515
   -0.12235    -0.11915    -0.11571    -0.11204    -0.10808
352.7       126.0       539.4       0.0         1.0
   -0.08021    -0.07258    -0.07083    -0.06805    -0.06282    -0.05561    -0.05032
   -0.04618    -0.04025    -0.03671    -0.03486    -0.03425    -0.03455    -0.03554
   -0.03751    -0.04070    -0.04509    -0.05026    -0.05626    -0.06320    -0.07088
   -0.07824    -0.08511    -0.09198    -0.09885    -0.10572
   -0.08021    -0.08648    -0.08793    -0.09022    -0.09433    -0.09957    -0.10288
   -0.10532    -0.10913    -0.11228    -0.11516    -0.11789    -0.12051    -0.12308
   -0.12539    -0.12671    -0.12711    -0.12666    -0.12551    -0.12366    -0.12116
   -0.11827    -0.11531    -0.11229    -0.10922    -0.10608
364.4       145.0       544.0       0.0         1.0
   -0.08522    -0.07780    -0.07614    -0.07350    -0.06866    -0.06191    -0.05687
   -0.05281    -0.04666    -0.04270    -0.04042    -0.03942    -0.03938    -0.04008
   -0.04145    -0.04397    -0.04775    -0.05246    -0.05778    -0.06389    -0.07057
   -0.07739    -0.08420    -0.09102    -0.09784    -0.10465
   -0.08522    -0.09085    -0.09215    -0.09418    -0.09766    -0.10159    -0.10387
   -0.10566    -0.10872    -0.11153    -0.11420    -0.11679    -0.11938    -0.12194
   -0.12415    -0.12533    -0.12563    -0.12505    -0.12369    -0.12162    -0.11899
   -0.11620    -0.11340    -0.11061    -0.10781    -0.10502
378.0       167.0       549.3       0.0         1.0
   -0.08537    -0.07765    -0.07592    -0.07324    -0.06830    -0.06147    -0.05641
   -0.05232    -0.04615    -0.04216    -0.03986    -0.03883    -0.03878    -0.03948
   -0.04089    -0.04336    -0.04701    -0.05165    -0.05690    -0.06290    -0.06947
   -0.07624    -0.08301    -0.08978    -0.09655    -0.10333
   -0.08537    -0.09119    -0.09249    -0.09450    -0.09783    -0.10149    -0.10387
   -0.10575    -0.10888    -0.11169    -0.11433    -0.11687    -0.11939    -0.12186
   -0.12382    -0.12480    -0.12496    -0.12426    -0.12281    -0.12070    -0.11797
   -0.11511    -0.11226    -0.10940    -0.10654    -0.10369
402.7       207.0       559.0       0.0         1.0
   -0.08567    -0.07738    -0.07555    -0.07270    -0.06756    -0.06057    -0.05544
   -0.05130    -0.04508    -0.04104    -0.03868    -0.03759    -0.03753    -0.03824
   -0.03970    -0.04208    -0.04556    -0.05004    -0.05508    -0.06086    -0.06721
   -0.07387    -0.08054    -0.08721    -0.09388    -0.10055
   -0.08567    -0.09187    -0.09319    -0.09518    -0.09825    -0.10147    -0.10391
   -0.10592    -0.10919    -0.11198    -0.11453    -0.11691    -0.11928    -0.12150
   -0.12294    -0.12361    -0.12349    -0.12263    -0.12099    -0.11872    -0.11582
   -0.11283    -0.10985    -0.10687    -0.10389    -0.10091
```

```
452.7     288.0     578.7     0.0       1.0
  -0.08651  -0.07666  -0.07457  -0.07130  -0.06566  -0.05815  -0.05279
  -0.04849  -0.04213  -0.03799  -0.03548  -0.03425  -0.03409  -0.03478
  -0.03643  -0.03865  -0.04176  -0.04568  -0.05039  -0.05555  -0.06134
  -0.06751  -0.07386  -0.08021  -0.08656  -0.09291
  -0.08651  -0.09375  -0.09513  -0.09705  -0.09957  -0.10218  -0.10442
  -0.10635  -0.10954  -0.11212  -0.11434  -0.11631  -0.11809  -0.11931
  -0.11993  -0.11992  -0.11917  -0.11784  -0.11582  -0.11319  -0.10984
  -0.10653  -0.10321  -0.09990  -0.09659  -0.09327
479.9     332.0     589.4     0.0       1.0
  -0.08717  -0.07612  -0.07384  -0.07037  -0.06425  -0.05630  -0.05073
  -0.04631  -0.03987  -0.03561  -0.03299  -0.03162  -0.03139  -0.03213
  -0.03389  -0.03608  -0.03890  -0.04252  -0.04690  -0.05181  -0.05713
  -0.06280  -0.06885  -0.07489  -0.08094  -0.08698
  -0.08717  -0.09518  -0.09664  -0.09860  -0.10081  -0.10313  -0.10510
  -0.10676  -0.10946  -0.11164  -0.11345  -0.11508  -0.11625  -0.11699
  -0.11714  -0.11670  -0.11564  -0.11393  -0.11167  -0.10869  -0.10516
  -0.10160  -0.09803  -0.09447  -0.09091  -0.08734
502.8     369.0     598.4     0.0       1.0
  -0.08789  -0.07569  -0.07323  -0.06933  -0.06280  -0.05435  -0.04854
  -0.04396  -0.03737  -0.03300  -0.03022  -0.02875  -0.02840  -0.02925
  -0.03101  -0.03316  -0.03587  -0.03923  -0.04321  -0.04787  -0.05279
  -0.05799  -0.06352  -0.06915  -0.07479  -0.08042
  -0.08789  -0.09680  -0.09832  -0.10030  -0.10231  -0.10410  -0.10551
  -0.10674  -0.10877  -0.11040  -0.11186  -0.11299  -0.11374  -0.11403
  -0.11375  -0.11291  -0.11147  -0.10950  -0.10693  -0.10364  -0.09992
  -0.09609  -0.09227  -0.08844  -0.08461  -0.08078
513.9     387.0     602.8     0.0       1.0
  -0.08833  -0.07543  -0.07286  -0.06881  -0.06191  -0.05316  -0.04718
  -0.04257  -0.03587  -0.03146  -0.02861  -0.02701  -0.02658  -0.02753
  -0.02929  -0.03145  -0.03408  -0.03728  -0.04109  -0.04556  -0.05032
  -0.05533  -0.06049  -0.06582  -0.07115  -0.07648
  -0.08833  -0.09769  -0.09931  -0.10130  -0.10324  -0.10445  -0.10545
  -0.10638  -0.10792  -0.10937  -0.11060  -0.11153  -0.11204  -0.11203
  -0.11154  -0.11053  -0.10894  -0.10678  -0.10396  -0.10061  -0.09676
  -0.09278  -0.08879  -0.08481  -0.08083  -0.07684
540.5     430.0     613.2     0.0       1.0
  -0.08969  -0.07483  -0.07178  -0.06722  -0.05948  -0.04968  -0.04313
  -0.03819  -0.03115  -0.02667  -0.02347  -0.02156  -0.02091  -0.02191
  -0.02369  -0.02596  -0.02852  -0.03143  -0.03481  -0.03863  -0.04305
  -0.04757  -0.05200  -0.05614  -0.06014  -0.06414
  -0.08969  -0.10053  -0.10233  -0.10458  -0.10632  -0.10538  -0.10458
  -0.10425  -0.10443  -0.10528  -0.10594  -0.10620  -0.10601  -0.10540
  -0.10432  -0.10266  -0.10052  -0.09781  -0.09462  -0.09110  -0.08673
  -0.08229  -0.07784  -0.07339  -0.06894  -0.06450
552.8     450.0     618.1     0.0       1.0
  -0.09055  -0.07451  -0.07127  -0.06635  -0.05796  -0.04758  -0.04061
  -0.03544  -0.02824  -0.02363  -0.02027  -0.01803  -0.01754  -0.01840
  -0.02010  -0.02231  -0.02490  -0.02782  -0.03104  -0.03459  -0.03870
  -0.04311  -0.04732  -0.05111  -0.05371  -0.05632
  -0.09055  -0.10234  -0.10428  -0.10664  -0.10846  -0.10626  -0.10401
  -0.10236  -0.10161  -0.10218  -0.10245  -0.10231  -0.10179  -0.10087
  -0.09939  -0.09748  -0.09503  -0.09190  -0.08859  -0.08503  -0.08030
  -0.07558  -0.07085  -0.06613  -0.06140  -0.05668
G-III WINGLET
3.        24.       1.0       75.0
576.0     450.0     618.1     0.0       1.0
0.        0.005     0.01      0.02      0.05      0.10      0.15
0.20      0.25      0.30      0.35      0.40      0.45      0.50
0.55      0.60      0.65      0.70      0.75      0.80      0.85
0.90      0.95      1.0
0.0       0.0088    0.01198   0.01650   0.02580   0.03615   0.04311
0.04762   0.05049   0.05175   0.05150   0.05020   0.04805   0.04534
0.04212   0.03850   0.03425   0.02990   0.02515   0.02034   0.01535
0.01060   0.00605   0.00170
0.0       -0.00780  -0.01007  -0.01290  -0.01740  -0.02163  -0.02424
-0.02577  -0.02650  -0.02670  -0.02640  -0.02555  -0.02440  -0.02295
-0.02100  -0.01845  -0.01500  -0.01070  -0.00620  -0.00250  0.00010
0.00155   0.00100   -0.00220
602.5     483.5     631.0     0.        1.0
0.0       0.01166   0.01608   0.02183   0.03160   0.04160   0.04790
0.05270   0.05625   0.05855   0.05995   0.06060   0.06060   0.05967
0.05790   0.05540   0.05200   0.04755   0.04230   0.03665   0.03030
0.02300   0.01385   0.00300
0.0       -0.00757  -0.01012  -0.01300  -0.01709  -0.02045  -0.02202
-0.02265  -0.02265  -0.02220  -0.02115  -0.01975  -0.01793  -0.01555
-0.01280  -0.00973  -0.00630  -0.00270  0.00070   0.00360   0.00480
0.00430   0.00200   -0.00220
629.0     517.0     644.0     0.0       0.0
-3.       8.0       864.5     0.        0.        0.        0.4
```

```
GULFSTREAM FUSELAGE QUICK-GEOMETRY MODEL
3.
1.          2.          NOSE TO WINDSHIELD BASE
BODYLO      ELLI        BDYBCL      BDYMHB      BDYLSCP
BODYHI      ELLI        BDYMHB      BDYTCL      BDYUSCP
2.          3.          WINDSHIELD
CANLO       ELLI        BDYBCL      BDYMHB      BDYLSCP
CANSI       ELLI        BDYMHB      CANLOW      CANLSCP
WINDF       LINE        CANLOW      BDYTCL
3.          4.          CANOPY
CANOPLO     ELLI        BDYBCL      BDYMHB      BDYLSCP
CANOPSI     ELLI        BDYMHB      CANLOW      CANLSCP
WINDSI      LINE        CANLOW      CANHIE
CANOPUP     ELLI        CANHIE      BDYTCL      CANTSCP
5.
1.          1.          8.0         64.0
2.          2.          64.0        83.5
3.          3.          83.5        133.0
4.          1.          133.0       575.5
5.          1.          575.5       864.5
10.         11.
3.          ZBDYBCL
ELLX        8.0         78.5        133.0       53.0        8.0         53.0
LINE        133.0       53.0        575.5       53.0
CUBI        575.5       53.0        864.5       114.5       625.0       53.0
5.          ZBDYTCL
ELLX        8.0         78.5        64.0        113.5       8.0         94.5
LINE        64.0        113.5       83.5        132.5
CUBI        83.5        132.5       133.0       147.0       98.0        147.0
LINE        133.0       147.0       575.5       147.0
CUBI        575.5       147.0       864.5       114.5       658.0       147.0
1.          YCENTER
LINE        8.0         0.0         864.5       0.0
3.          ZBDYMHB
CUBI        8.0         78.5        181.0       100.0       135.5       100.0
LINE        181.0       100.0       502.0       100.0
CUBI        502.0       100.0       864.5       114.5       616.5       100.0
3.          YBDYMHB
ELLX        8.0         0.          206.0       47.0        8.0         47.0
LINE        206.0       47.0        502.0       47.0
CUBI        502.0       47.0        864.5       0.          636.0       47.0
1.          ZCANLOW
LINE        64.0        113.5       133.0       113.5
1.          ZCANHIE
LINE        83.5        132.5       133.0       132.5
2.          YCANLOW
LINE        64.0        0.          79.5        28.0
LINE        79.5        28.0        133.0       42.0
2.          YCANHIE
LINE        83.5        0.          96.0        24.5
LINE        96.0        24.5        133.0       34.0
1.          YCANTSCP
LINE        83.5        0.          133.0       22.0
            ZMAPAXIS    ZBDYMHB
            YMAPAXIS    YCENTER
            ZCANTSCP    ZBDYTCL
            ZCANLSCP    ZCANLOW
            YCANLSCP    YBDYMHB
            YBDYTCL     YCENTER
            YBDYBCL     YCENTER
            YBDYLSCP    YBDYMHB
            ZBDYLSCP    ZBDYBCL
            YBDYUSCP    YBDYMHB
            ZBDYUSCP    ZBDYTCL
G-III NACELLE
1.          481.25      668.75      78.95       73.3        16.0        0.0
2.75        -0.5        0.          0.66        2.0
0.          6.67        13.33       20.00       26.67       33.33       40.00
46.67       53.33       60.00       66.67       73.33       80.00       86.67
93.33       100.0
9.82        12.0        13.05       13.69       13.89       14.04       14.04
14.04       13.96       13.62       13.13       12.21       11.16       9.89
8.42        6.81
```

```
C-5A TRANSPORT WITH ENGINE PODS AND PYLONS
3.          0.775       2.50        2.5         100.        80.         3.0
2.          0.          2.
5.          31.         1.0         165.3       20.0        18720.0     1.0
109.96      0.          189.17      4.18        0.
    0.0         0.25000     0.50000     0.75000     1.00000     2.00000     4.00000
    6.00000     8.00000    10.00000    12.00000    14.00000    16.00000    18.00000
   20.00000    25.00000    30.00000    35.00000    40.00000    45.00000    50.00000
   55.00000    60.00000    65.00000    70.00000    75.00000    80.00000    85.00000
   90.00000    95.00000   100.00000
    0.56298     1.16181     1.49063     1.74381     1.95621     2.59646     3.35404
    3.94282     4.39117     4.76414     5.05056     5.33434     5.58457     5.79552
    6.00648     6.39246     6.67431     6.85000     6.91854     6.91625     6.76694
    6.55966     6.26794     5.90856     5.45495     4.90702     4.25141     3.48790
    2.56929     1.46900     0.12887
    0.56336    -0.41909    -0.70382    -0.89820    -1.06155    -1.56102    -2.31165
   -2.92237    -3.41914    -3.83526    -4.15688    -4.47850    -4.76203    -5.00587
   -5.24884    -5.68123    -5.98528    -6.16150    -6.20322    -6.11709    -5.90316
   -5.57466    -5.13838    -4.58723    -3.96548    -3.29717    -2.57890    -1.84615
   -1.16210    -0.57491    -0.12896
147.37      69.5        201.04      2.90        1.0
    0.58099     1.16726     1.49248     1.75712     1.96323     2.60530     3.38237
    3.98024     4.44052     4.80000     5.11966     5.41050     5.66225     5.87825
    6.09324     6.49263     6.78225     6.97204     7.06200     7.06200     6.97212
    6.78242     6.50284     6.14336     5.68417     5.11525     4.41675     3.58518
    2.58115     1.44331     0.11019
    0.58099    -0.39277    -0.70676    -0.90126    -1.06083    -1.51522    -2.11367
   -2.57321    -2.92607    -3.20495    -3.40705    -3.60305    -3.77372    -3.90973
   -4.04572    -4.28388    -4.42525    -4.49639    -4.48732    -4.40760    -4.24770
   -4.01791    -3.71824    -3.34869    -2.90013    -2.42997    -1.94043    -1.46043
   -0.98114    -0.53175    -0.11019
154.10      82.0        203.17      2.68        1.0
    0.58031     1.15696     1.49673     1.75361     1.96380     2.60772     3.38790
    3.98975     4.43000     4.79000     5.14097     5.43662     5.69037     5.90815
    6.12201     6.53237     6.82420     7.00831     7.10610     7.11697     7.02803
    6.84322     6.57149     6.20261     5.75804     5.18479     4.47149     3.59955
    2.59158     1.37545     0.10949
    0.58031    -0.39956    -0.70439    -0.89548    -1.05719    -1.49729    -2.06062
   -2.47998    -2.79766    -3.03450    -3.20384    -3.36684    -3.50283    -3.60284
   -3.70284    -3.88321    -3.98274    -4.01792    -3.99696    -3.92039    -3.77952
   -3.56939    -3.31939    -2.98628    -2.60584    -2.19457    -1.77261    -1.35957
   -0.94637    -0.52253    -0.10949
167.59      108.0       211.27      2.18        1.0
    0.60323     1.24885     1.57273     1.82851     2.04443     2.69783     3.47276
    4.06878     4.51000     4.89000     5.21000     5.51035     5.74338     5.96338
    6.17917     6.57927     6.85882     7.04174     7.11491     7.10258     6.98062
    6.76147     6.45772     6.05988     5.58484     5.00134     4.28537     3.44006
    2.47901     1.35890     0.11050
    0.60323    -0.38175    -0.72092    -0.91419    -1.07370    -1.52129    -2.06233
   -2.45674    -2.74150    -2.95825    -3.10856    -3.25177    -3.37625    -3.47381
   -3.57137    -3.73756    -3.86369    -3.93764    -3.93943    -3.87902    -3.74297
   -3.53591    -3.26171    -2.94464    -2.54515    -2.13052    -1.70554    -1.28083
   -0.86666    -0.47665    -0.11080
204.32      178.80      233.32      0.9         1.0
    0.74507     1.58808     1.96509     2.27170     2.49666     3.17314     3.94205
    4.51033     4.91000     5.27655     5.54855     5.82055     6.05628     6.26346
    6.46873     6.83983     7.10184     7.18633     7.15015     6.99479     6.70912
    6.31043     5.83194     5.25452     4.59713     3.89070     3.19065     2.46205
    1.74123     0.96068     0.10068
    0.74507    -0.23683    -0.68123    -0.92621    -1.13260    -1.62776    -2.07020
   -2.32072    -2.46180    -2.54245    -2.59064    -2.63146    -2.67519    -2.72437
   -2.77355    -2.95676    -3.20575    -3.47032    -3.63361    -3.64473    -3.53790
   -3.31576    -2.99489    -2.61461    -2.19781    -1.77575    -1.29685    -0.85767
   -0.45959    -0.20068    -0.10068
C-5A INBOARD PYLON
2.          31.         1.0         69.48
0.          -13.0       1.0         0.          1.0
0.          0.12048     0.25301     0.37349     0.49398     0.62651     0.74799
1.0         1.25301     1.87952     2.49398     5.0         7.61446     10.0
15.0        20.0        25.0        30.0        40.0        45.0        50.0
55.0        60.0        65.0        70.0        75.0        80.0        85.0
90.0        95.0        100.0
0.          0.43193     0.68675     0.85542     1.02410     1.12048     1.24096
1.42169     1.57831     1.90361     2.18072     2.81928     3.22892     3.53012
3.91566     4.08434     4.22892     4.25301     4.25301     4.22892     4.14458
4.02410     3.83133     3.59036     3.28916     2.92771     2.49398     2.00000
1.43373     0.79518     0.08434
0.          -0.43193    -0.68675    -0.85542    -1.02410    -1.12048    -1.24096
-1.42169    -1.57831    -1.90361    -2.18072    -2.81928    -3.22892    -3.53012
-3.91566    -4.08434    -4.22892    -4.25301    -4.25301    -4.22892    -4.14458
-4.02410    -3.83133    -3.59036    -3.28916    -2.92771    -2.49398    -2.00000
-1.43373    -0.79518    -0.08434
0.          0.          1.          0.          0.
```

```
C-5A OUTBOARD PYLON
2.          31.         1.0         108.14
0.          -13.0       1.0         0.          1.0
0.          0.12048     0.25301     0.37349     0.49398     0.62651     0.74799
1.0         1.25301     1.87952     2.49398     5.0         7.61446     10.0
15.0        20.0        25.0        30.0        40.0        45.0        50.0
55.0        60.0        65.0        70.0        75.0        80.0        85.0
90.0        95.0        100.0
0.          0.48193     0.68675     0.85542     1.02410     1.12048     1.24096
1.42169     1.57831     1.90361     2.18072     2.81928     3.22892     3.53012
3.91566     4.08434     4.22892     4.25301     4.25301     4.22892     4.14458
4.02410     3.83133     3.59036     3.28916     2.92771     2.49398     2.00000
1.43373     0.79518     0.08434
0.          -0.48193    -0.68675    -0.85542    -1.02410    -1.12048    -1.24096
-1.42169    -1.57831    -1.90361    -2.18072    -2.81928    -3.22892    -3.53012
-3.91566    -4.08434    -4.22892    -4.25301    -4.25301    -4.22892    -4.14458
-4.02410    -3.83133    -3.59036    -3.28916    -2.92771    -2.49398    -2.00000
-1.43373    -0.79518    -0.08434
0.          0.          1.          0.          0.
-3.         -30.0       380.04      0.          0.0         0.          0.4
LOCKHEED C-5A FUSELAGE          QUICK-GEOMETRY MODEL
4.
1.          2.          NOSE/TAIL
BODYLO      ELLI        BDYBCL      BDYMHB      BDYLSCP
BODYHI      ELLI        BDYMHB      BDYTCL      BDYUSCP
2.          3.          WING-BODY FAIRING
BODYLO      ELLI        BDYBCL      BDYMHB      BDYLSCP
BODYSI      LINE        BDYMHB      FAIRT
BODYUP      ELLI        FAIRT       BDYTCL      BDYUSCP
3.          4.          W-B FAIRING W/ WHEEL FAIRING
BODYLO      ELLI        BDYBCL      BULSI       BULLSCP
BULSID      ELLI        BULSI       BULTOP      BULUSCP
BODYSI      LINE        BULTOP      FAIRT
BODYUP      ELLI        FAIRT       BDYTCL      BDYUSCP
4.          4.          AFT FUSELAGE W/ WHEEL FAIRING
BODYLO      ELLI        BDYBCL      BULSI       BULLSCP
BULSID      ELLI        BULSI       BULTOP      BULUSCP
BODYSI      LINE        BULTOP      BDYMHB
BODYHI      ELLI        BDYMHB      BDYTCL      BDYUSCP
5.
1.          1.          -30.0       92.0
2.          2.          92.0        141.0
3.          3.          141.0       185.0
4.          4.          185.0       224.0
5.          1.          224.0       380.04
10.         13.
4.          ZBDYTCL
ELLX        -30.0       -4.0        -5.0        18.0        -30.0       5.5
ELLY        -5.0        18.0        10.0        23.38       1.0         23.38
LINE        10.0        23.38       290.0       23.38
ELLY        290.0       23.38       380.04      13.0        335.0       23.38
3.          ZBDYBCL
ELLX        -30.0       -4.0        10.0        -23.38      -30.0       -23.38
LINE        10.0        -23.38      215.0       -23.38
ELLY        215.0       -23.38      380.04      13.0        265.0       -23.38
3.          ZBDYMHB
ELLY        -30.0       -4.0        10.0        0.0         -20.0       0.0
LINE        10.0        0.          215.0       0.
ELLY        215.0       0.          380.04      13.0        300.0       0.0
1.          YCENTER
LINE        -30.0       0.          380.04      0.0
3.          YBDYMHB
ELLX        -30.0       0.0         10.0        21.0        -30.0       21.0
LINE        10.0        21.0        300.0       21.0
ELLY        300.0       21.0        380.04      0.0         320.0       21.0
3.          ZFAIRT
ELLX        92.0        0.0         112.0       20.0        92.0        20.0
LINE        112.0       20.0        140.0       20.0
ELLX        140.0       20.0        185.0       0.0         185.0       0.0
3.          YBULSI
ELLX        141.0       19.0        160.0       27.54       141.0       27.54
LINE        160.0       27.54       204.0       27.54
ELLX        204.0       27.54       224.0       19.0        224.0       27.54
1.          ZBULSI
LINE        141.0       -16.0       224.0       -16.0
1.          ZBULTOP
LINE        141.0       -6.0        224.0       -6.0
1.          YBULTOP
LINE        141.0       20.0        224.0       20.0
            YBDYBCL     YCENTER
            YBDYTCL     YCENTER
```

```
          YMAPAXIS  YCENTER
          ZMAPAXIS  ZBDYMHB
          ZBDYUSCP  ZBDYTCL
          YBDYUSCP  YBDYMHB
          YBDYLSCP  YBDYMHB
          ZBDYLSCP  ZBDYBCL
          YFAIRT    YBDYMHB
          YBULLSCP  YBULSI
          ZBULLSCP  ZBDYBCL
          YBULUSCP  YBULSI
          ZBULUSCP  ZBULTOP
C5A INBOARD ENGINE NACELLE (CONFIGURATION 1, NASA TN X-2530)
1.        115.41    161.90    69.48     -13.10    26.0
0.        -1.       0.        1.        1.93
0.        0.38      1.58      3.55      6.34      12.25     19.88
30.17     34.91     37.69     39.65     44.74     51.10     56.99
62.08     67.17     71.33     75.49     79.77     81.85     84.97
88.79     92.02     94.91     98.50     100.0
13.99     14.39     14.80     15.20     15.61     16.01     16.01
15.84     15.49     15.14     14.97     14.80     14.45     14.10
13.70     13.35     12.95     12.49     12.10     11.79     11.54
11.02     10.50     10.00     9.30      8.93
C5A OUTBOARD ENGINE NACELLE
1.        136.20    182.69    108.14    -13.10    26.0
0.        -1.       0.        1.        1.93
0.        0.38      1.58      3.55      6.34      12.25     19.88
30.17     34.91     37.69     39.65     44.74     51.10     56.99
62.08     67.17     71.33     75.49     79.77     81.85     84.97
88.79     92.02     94.91     98.50     100.0
13.99     14.39     14.80     15.20     15.61     16.01     16.01
15.84     15.49     15.14     14.97     14.80     14.45     14.10
13.70     13.35     12.95     12.49     12.10     11.79     11.54
11.02     10.50     10.00     9.30      8.93
```

```
C-141 TRANSPORT WITH PODS AND PYLONS
3.          0.82        -0.3        36.0        100.        80.         3.
2.          0.          2.
6.          33.         1.0         747.99      85.0        463007.0    0.8
648.76      0.          1045.54     4.89        1.0
0.          0.002408    0.009607    0.021530    0.038060    0.059040    0.084266
0.113495    0.146447    0.182804    0.222216    0.264303    0.308660    0.354859
0.402456    0.450993    0.5         0.549011    0.597547    0.645144    0.691344
0.735700    0.777787    0.817199    0.853555    0.886507    0.915736    0.940962
0.961941    0.978471    0.990393    0.997593    1.0
0.          0.010839    0.019266    0.027140    0.034418    0.041114    0.047226
0.052771    0.057762    0.062198    0.066040    0.069274    0.071815    0.073591
0.074499    0.074464    0.073450    0.071465    0.068551    0.064789    0.060277
0.055175    0.049126    0.042299    0.035174    0.028283    0.021681    0.015644
0.010439    0.006214    0.003099    0.001191    0.000548
0.          -0.007695   -0.015563   -0.022735   -0.028997   -0.034457   -0.039186
-0.043259   -0.046734   -0.049646   -0.052012   -0.053822   -0.055037   -0.055602
-0.055437   -0.054479   -0.052711   -0.050132   -0.046857   -0.042895   -0.038417
-0.033620   -0.029048   -0.024745   -0.020469   -0.016421   -0.012715   -0.009258
-0.006230   -0.003781   -0.001972   -0.000902   -0.000548
709.51      113.60      1062.45     4.44        1.0
0.          0.010402    0.018683    0.026436    0.033623    0.040246    0.046301
0.051798    0.056733    0.061120    0.064922    0.068117    0.070612    0.072354
0.073246    0.073197    0.072173    0.070185    0.067274    0.063510    0.059035
0.053955    0.048009    0.041336    0.034369    0.027628    0.021199    0.015324
0.010255    0.006139    0.003104    0.001244    0.000617
0.          -0.007613   -0.015273   -0.022194   -0.028211   -0.033438   -0.037952
-0.041829   -0.045123   -0.047867   -0.050087   -0.051776   -0.052897   -0.053399
-0.053203   -0.052245   -0.050524   -0.048042   -0.044870   -0.041056   -0.036852
-0.032331   -0.028064   -0.023881   -0.019742   -0.015872   -0.012279   -0.008938
-0.006034   -0.003690   -0.001971   -0.000954   -0.000617
875.95        426.57      1108.76     2.68        1.0
0.          0.008481    0.015968    0.023056    0.029734    0.035960    0.041691
0.046925    0.051651    0.055865    0.059550    0.062643    0.065006    0.066662
0.067546    0.067507    0.066524    0.064600    0.061798    0.058169    0.053788
0.048790    0.043247    0.037220    0.030960    0.024872    0.019225    0.013866
0.009265    0.005640    0.003025    0.001452    0.000927
0.          -0.007009   -0.013598   -0.019253   -0.024035   -0.028082   -0.031496
-0.034367   -0.036773   -0.038743   -0.040312   -0.041492   -0.042249   -0.042551
-0.042335   -0.041530   -0.040198   -0.038345   -0.035862   -0.032981   -0.029791
-0.026339   -0.022870   -0.019502   -0.016308   -0.013138   -0.010145   -0.007451
-0.005158   -0.003299   -0.001973   -0.001188   -0.000927
970.00      610.61      1168.16     2.0         1.0
0.          0.009672    0.017676    0.025221    0.032209    0.038329    0.043795
0.048929    0.053559    0.057574    0.061091    0.064058    0.066351    0.067961
0.068811    0.068739    0.067726    0.065764    0.062924    0.059250    0.054829
0.049790    0.044213    0.038187    0.032121    0.026136    0.020200    0.014781
0.009914    0.006080    0.003314    0.001649    0.001094
0.          -0.008537   -0.014707   -0.020053   -0.024283   -0.027654   -0.03010
-0.032494   -0.034330   -0.035952   -0.037221   -0.038194   -0.038813   -0.039056
-0.038847   -0.038094   -0.036832   -0.035076   -0.032742   -0.030065   -0.027074
-0:023953   -0.020878   -0.017915   -0.014951   -0.012050   -0.009334   -0.006916
-0.004857   -0.003190   -0.002020   -0.001324   -0.001094
1046.90     761.11      1216.72     1.10        1.0
0.          0.010861    0.019412    0.026801    0.033809    0.040077    0.045764
0.051155    0.055703    0.059494    0.062821    0.065645    0.067854    0.069416
0.070227    0.070119    0.069069    0.067069    0.064185    0.060466    0.055998
0.050912    0.045301    0.039291    0.033280    0.027176    0.021081    0.015406
0.010456    0.006450    0.003576    0.001849    0.001273
0.          -0.007864   -0.015035   -0.020423   -0.024372   -0.027112   -0.028905
-0.030311   -0.031517   -0.032754   -0.033689   -0.034434   -0.034903   -0.035080
-0.034886   -0.034193   -0.033012   -0.031370   -0.029209   -0.026693   -0.023989
-0.021234   -0.018547   -0.015925   -0.013294   -0.010747   -0.008389   -0.006294
-0.004527   -0.003120   -0.002099   -0.001480   -0.001273
1147.81     958.89      1280.45     -0.36       1.0
0.          0.011822    0.020558    0.029023    0.037201    0.043904    0.049966
0.055534    0.059913    0.063263    0.066214    0.068748    0.070790    0.072251
0.072985    0.072806    0.071682    0.069612    0.066645    0.062835    0.058284
0.053105    0.047429    0.041455    0.035483    0.029030    0.022233    0.016142
0.011014    0.006945    0.004003    0.002223    0.001626
0.          -0.010134   -0.017776   -0.022607   -0.024847   -0.025861   -0.025927
-0.025799   -0.025793   -0.026292   -0.026582   -0.026890   -0.027076   -0.027139
-0.026981   -0.026417   -0.025407   -0.023997   -0.022188   -0.020096   -0.018016
-0.015950   -0.013922   -0.011912   -0.009968   -0.008134   -0.006497   -0.005069
-0.003860   -0.002889   -0.002189   -0.001765   -0.001623
```

```
C-141 INBOARD PYLON
2.          49.         1.0         278.91
0.          -15.0       1.0         0.
0.          0.25        0.50        0.75        1.0         1.25        1.50
1.75        2.00        2.50        5.00        7.50        10.0        12.50
15.00       17.578      20.0        22.50       25.00       27.50       30.00
32.50       35.00       37.50       40.00       42.50       45.00       47.50
50.0        52.50       55.00       57.50       60.00       62.50       65.00
67.50       70.00       72.50       75.102      77.50       80.00       82.50
85.00       87.50       90.00       92.50       95.00       97.50       100.0
0.          1.16140     1.62826     1.98016     2.27227     2.52600     2.75230
2.95773     3.14664     3.48600     4.73800     5.60000     6.24200     6.73996
7.12800     7.43384     7.65000     7.81298     7.92200     7.98298     8.00200
7.98394     7.93194     7.84905     7.73800     7.60107     7.44066     7.25903
7.05800     6.83912     6.60357     6.35225     6.08600     5.80545     5.51140
5.20471     4.88600     4.55577     4.20014     3.86170     3.49800     3.12325
2.73723     2.33959     1.93000     1.50820     1.07400     0.62728     0.16800
0.          -1.16140    -1.62826    -1.98016    -2.27227    -2.52600    -2.75230
-2.95773    -3.14664    -3.48600    -4.73800    -5.60000    -6.24200    -6.73996
-7.12800    -7.43384    -7.65000    -7.81298    -7.92200    -7.98298    -8.00200
-7.98394    -7.93194    -7.84905    -7.73800    -7.60107    -7.44066    -7.25903
-7.05800    -6.83912    -6.60357    -6.35225    -6.08600    -5.80545    -5.51140
-5.20471    -4.88600    -4.55577    -4.20014    -3.86170    -3.49800    -3.12325
-2.73723    -2.33959    -1.93000    -1.50820    -1.07400    -0.62728    -0.16800
0.          0.          1.          0.          0.
C-141 OUTBOARD PYLON
2.          49.         1.0         456.89
0.          -18.0       1.0         0.          1.0
0.          0.25        0.50        0.75        1.0         1.25        1.50
1.75        2.00        2.50        5.00        7.50        10.0        12.50
15.00       17.578      20.0        22.50       25.00       27.50       30.00
32.50       35.00       37.50       40.00       42.50       45.00       47.50
50.0        52.50       55.00       57.50       60.00       62.50       65.00
67.50       70.00       72.50       75.102      77.50       80.00       82.50
85.00       87.50       90.00       92.50       95.00       97.50       100.0
0.          1.16140     1.62826     1.98016     2.27227     2.52600     2.75230
2.95773     3.14664     3.48600     4.73800     5.60000     6.24200     6.73996
7.12800     7.43384     7.65000     7.81298     7.92200     7.98298     8.00200
7.98394     7.93194     7.84905     7.73800     7.60107     7.44066     7.25903
7.05800     6.83912     6.60357     6.35225     6.08600     5.80545     5.51140
5.20471     4.88600     4.55577     4.20014     3.86170     3.49800     3.12325
2.73723     2.33959     1.93000     1.50820     1.07400     0.62728     0.16800
0.          -1.16140    -1.62826    -1.98016    -2.27227    -2.52600    -2.75230
-2.95773    -3.14664    -3.48600    -4.73800    -5.60000    -6.24200    -6.73996
-7.12800    -7.43384    -7.65000    -7.81298    -7.92200    -7.98298    -8.00200
-7.98394    -7.93194    -7.84905    -7.73800    -7.60107    -7.44066    -7.25903
-7.05800    -6.83912    -6.60357    -6.35225    -6.08600    -5.80545    -5.51140
-5.20471    -4.88600    -4.55577    -4.20014    -3.86170    -3.49800    -3.12325
-2.73723    -2.33959    -1.93000    -1.50820    -1.07400    -0.62728    -0.16800
0.          0.          1.          0.          0.
-3.          230.4       1818.0      0.          0.          0.          0.4
LOCKHEED C-141 QUICK-GEOMETRY FUSELAGE MODEL
4.
1.          2.          NOSE TO TAIL
BODYLO      ELLI        BDYBCL      BDYMHB      BDYLSCP
BODYHI      ELLI        BDYMHB      BDYTCL      BDYUSCP
2.          3.          FUSELAGE WITH WING MOUNT FAIRING
FAIRLO      ELLI        BDYBCL      BDYMHB      BDYLSCP
FAIRSI      LINE        BDYMHB      BS
FAIRTP      LINE        BS          BDYTCL
3.          5.          FUSELAGE WITH WHEEL AND WING FAIRING
WHEELO      LINE        BDYBCL      WL
WHEELSI     LINE        WL          WT
WHEELUP     LINE        WT          BDYMHB
FAIRS       LINE        BDYMHB      BS
FAIRT       LINE        BS          BDYTCL
4.          4.          FUSELAGE WITH WHEEL FAIRING
WHELO       LINE        BDYBCL      WL
WHELS       LINE        WL          WT
WHELU       LINE        WT          BDYMHB
UPPER       ELLI        BDYMHB      BDYTCL      BDYUSCP
5.
1.          1.          230.4       650.0
2.          2.          650.0       794.0
3.          3.          794.0       1050.0
4.          4.          1050.0      1198.0
5.          1.          1198.0      1822.0
11.         8.
3.          ZBDYBCL
ELLX        230.4       -15.0       445.0       -85.0       230.4       -85.0
LINE        445.0       -85.0       1100.0      -85.0
CUBI        1100.0      -85.0       1822.0      70.0        1485.0      -85.0
```

```
3.          YBDYMHB
ELLX        230.4       0.          445.0       85.0        230.4       85.0
LINE        445.0       85.0        1475.0      85.0
CUBI        1475.0      85.0        1822.0      0.0         1685.0      85.0
1.          YCENTER
LINE        230.4       0.          1822.0      0.
10.         ZBDYTCL
ELLX        230.4       -15.0       270.0       40.0        230.4       22.0
LINE        270.0       40.0        310.0       70.0
CUBI        310.0       70.0        400.0       85.0        330.0       85.0
LINE        400.0       85.0        650.0       85.0
CUBI        650.0       85.0        785.0       110.0       700.0       110.0
CUBI        785.0       110.0       1050.0      85.0        850.0       110.0
LINE        1050.0      85.0        1250.0      94.0
LINE        1250.0      94.0        1350.0      107.0
LINE        1350.0      107.0       1450.0      111.0
CUBI        1450.0      111.0       1822.0      70.0        1645.0      111.0
3.          ZBDYMHB
CUBI        230.4       -15.0       445.0       0.          330.0       0.
LINE        445.0       0.          1150.0      0.
CUBI        1150.0      0.          1822.0      70.0        1440.0      0.
2.          ZBS
CUBI        650.0       60.0        785.0       111.0       700.0       111.0
CUBI        785.0       111.0       1050.0      60.0        850.0       111.0
3.          YBS
LINE        650.0       60.0        690.0       85.0
LINE        690.0       85.0        1000.0      85.0
LINE        1000.0      85.0        1050.0      60.0
3.          ZWL
LINE        794.0       -85.0       900.0       -75.0
LINE        900.0       -75.0       1100.0      -75.0
LINE        1100.0      -75.0       1198.0      -85.0
3.          YWL
LINE        794.0       0.          900.0       136.5
LINE        900.0       136.5       1100.0      136.5
LINE        1100.0      136.5       1198.0      0.
1.          ZWT
LINE        794.0       -24.0       1198.0      -24.0
3.          YWT
LINE        794.0       73.0        900.0       136.5
LINE        900.0       136.5       1100.0      136.5
LINE        1100.0      136.5       1198.0      73.0
            ZMAPAXIS    ZBDYMHB
            YMAPAXIS    YCENTER
            YBDYTCL     YCENTER
            YBDYBCL     YCENTER
            YBDYUSCP    YBDYMHB
            ZBDYUSCP    ZBDYTCL
            YBDYLSCP    YBDYMHB
            ZBDYLSCP    ZBDYBCL
C-141 INBOARD NACELLE
0.          667.91      883.32      278.91      -95.00      30.0        0.
0.          2.          0.          1.          2.
0.          0.25        0.50        1.0         1.5         2.5         3.51
4.52        5.52        6.53        7.53        8.54        9.54        10.54
12.55       14.56       16.26       54.18       55.23       58.75       63.77
68.79       72.81       77.82       81.84       85.86       89.88       93.89
98.99       100.0
12.53       12.92       13.10       13.37       13.58       13.92       14.18
14.40       14.59       14.76       14.90       15.01       15.11       15.18
15.26       15.31       15.32       15.32       15.32       15.26       15.06
14.72       14.35       13.75       13.17       12.49       11.72       10.85
9.61        9.34
C-141 OUTBOARD NACELLE
0.          755.02      970.43      456.89      -95.00      30.0        0.
0.          1.0         0.          1.          2.
0.          0.25        0.50        1.0         1.5         2.5         3.51
4.52        5.52        6.53        7.53        8.54        9.54        10.54
12.55       14.56       16.26       54.18       55.23       58.75       63.77
68.79       72.81       77.82       81.84       85.86       89.88       93.89
98.99       100.0
12.53       12.92       13.10       13.37       13.58       13.92       14.18
14.40       14.59       14.76       14.90       15.01       15.11       15.18
15.26       15.31       15.32       15.32       15.32       15.26       15.06
14.72       14.35       13.75       13.17       12.49       11.72       10.85
9.61        9.34
```

OUTPUT DATA (PRINT & PLOT) FORMAT

Printed and plotted output data is provided. Since a typical print or plot sequence is lengthy, only a brief description of each type of output will be provided here. Note that samples of plotted output can be found in the results and geometry verification section of this report.

Printed Output

The printed output can be divided into three distinct sections.

Section I	Input Data Listing/Geometry and Grid System Verification
Section II	Relaxation Solution Convergence History
Section III	Computed Velocities, Pressures, Forces, Moments, Reference Lengths and Areas

Within each section, the output data will be printed in the following sequence.

Section I

- Input Data Listing
- Case Flow Condition
- Nominal Extent of Fine Embedded Grid Systems
- Quick-Geometry Model Error Diagnostic Information (BKOD = ±3 only)
- Configuration Position in Global Crude Grid System*
- Body Crude/Fine Grid Limiters (See Note #1, following page)
- Global Crude Grid Coordinates
- Fine Embedded Wing Grid Coordinates
- Pylon Limiters (PY > 0)
- Pod/Nacelle Limiters and Boundary Conditions (Pod > 0)
- TAG Grid System Coordinates (VER ≠ 0)
- Winglet Grid System Coordinates (VER > 0)
- Fine Embedded Body Grid Coordinates

---

* The configuration is positioned to prevent crude cartesian grid points from falling near the wing leading edge.

Section II

Phase 1 (Global Crude Grid Solution)

The following information is printed for each crude grid iteration.

A
- Iteration Count
- Maximum Correction to the Flow Field Potential ($\Delta\phi_{MAX}$)
- Grid Position of $\Delta\phi_{MAX}$
- Wing Spanwise Circulation (Γ) Distribution

NOTE #1

The body crude and fine grid limiters are the J and K values which define special grid points. These limiter values represent the first grid point relaxed beyond a fixed potential body boundary point. By using the J and K limiters listed, a sketch of the body boundary surface can be composed. A typical limiter listing can be found in the table below:

FINE GRID BODY BOUNDARY POINT LIMITERS

J	KUP	KLO	JSD
1	20	6	10
2	20	6	10
3	20	6	10
4	20	7	10
5	19	7	10
6	19	7	10
7	18	7	10
8	17	7	10
9	16	7	10
10	15	8	10

CRUDE GRID BODY BOUNDARY POINT LIMITERS

J	KUP	KLO	JSD
1	22	15	4
2	21	15	4
3	20	15	4
4	19	16	4

The body boundary surface points have been sketched below in Fig. A-3.

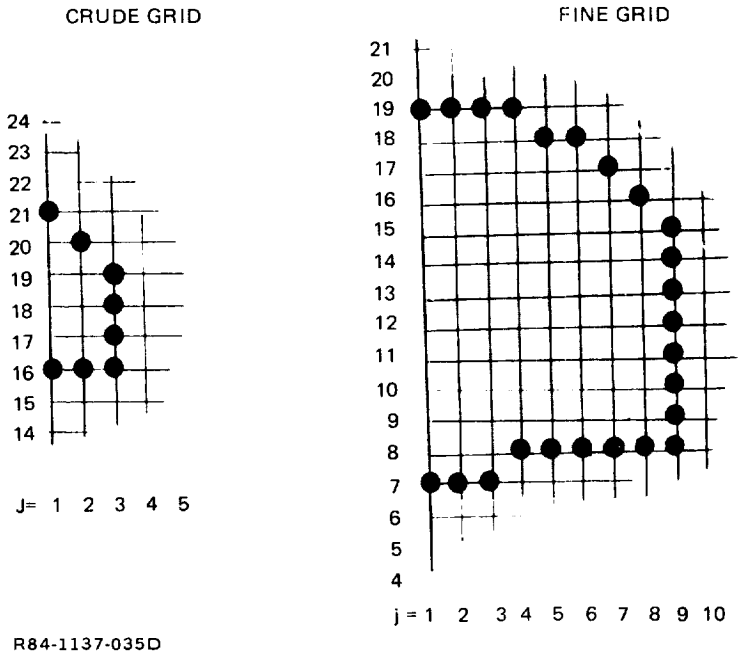

Figure A-3 Body Boundary Point Limiters

Following the body boundary point limiters, additional limiters will be listed if the embedded fine body grid option has been selected. The following figure indicates that IBGI, IBGL, JBG, KBGU and KBGL grid points represent the first crude point relaxed beyond the embedded fine grid boundary.

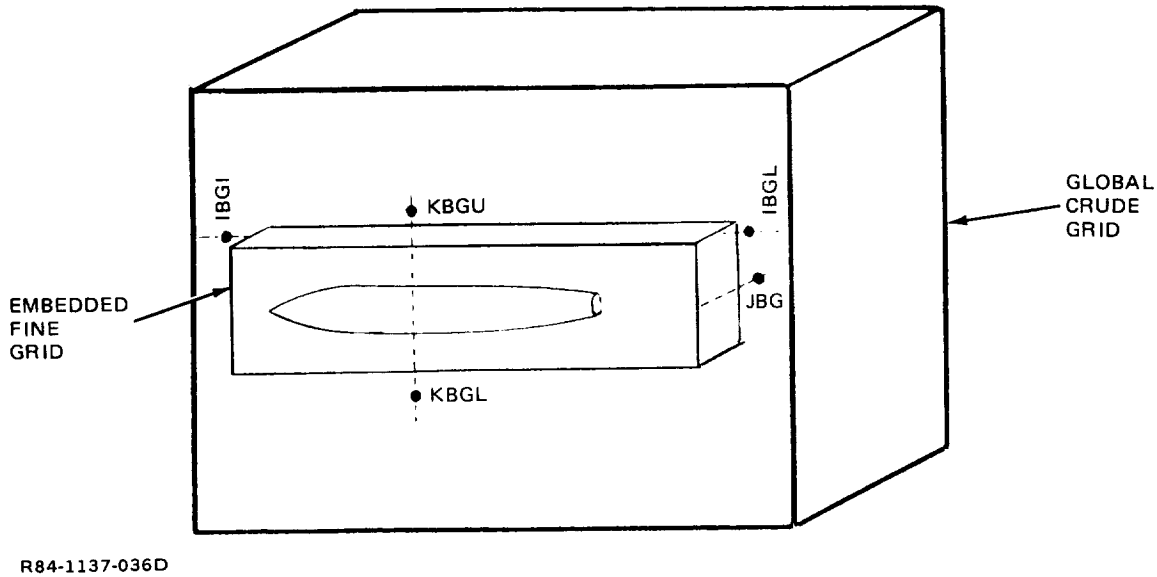

Figure A-4 Embedded Body Fine Grid Boundary Limiters

The following information is printed at the end of the Global Crude Grid Solution.

B
- Section Mach Chart (0 indicates subsonic flow)
  (1 indicates supersonic flow)
  (8 indicates wing section surface)
  (7 indicates wake surface)
- Span row number/η-position/local chord length, chord position, pressure coefficient, disturbance velocity, section circulation (Γ).

Phase 2 (Crude/Fine Grid Interactions)

The following information is printed for each crude/fine grid iteration cycle.

- Phase 1 (A) Output for Fine Embedded Wing Grid System
- Pylon Vertical Circulation Distribution (PY > 0)
- Phase I (A) Output For Fine Embedded Winglet Grid System (VER > 0)
- Phase I (A) Output For Fine Embedded Pod Grid System (FIFP > 0 Only)
- Phase I (A) Output For TAG (VER $\neq$ 0)
- TAG Circulation Distribution For Wing and Winglet
- Phase 1 (A) Output for Fine Embedded Body Grid System (for BKOD > 0 only)
- Phase 1 (A) Output for Global Crude Grid System
- Wing Spanwise Circulation (Γ) Distribution

For viscous interaction cases, the following information is printed every 20th cycle.

- Wing Upper/Lower Surface Boundary Layer Separation Point (x/c)
- Boundary Layer δ^* Slope Added to Wing Boundary Conditions.

Section III

The following information is printed at the end of the solution process.

- Phase 1 (B) Output for Wing Embedded Fine Grid System
- For (VISMOD = 2,3) Wing Upper/Lower Surface Boundary Layer Separation Point (x/c)

- Wing Section C_{ℓ_W}, C_{m_W}, C_{d_W}, C_{f_W}

  Note: C_{m_W} is section moment about local quarter chord position
- Spanwise Load, Moment, Drag Distributions
- Wing Exposed Area, Total Area, Aspect Ratio, Taper Ratio, Mean Aerodynamic Chord, Average Chord, X-position about which Moments are computed
- Total Wing $C_{L_{WING}}$, $C_{M_{WING}}$, $C_{D_{WING}}$
- Pylon Surface Pressures
- Phase I (B) Output For Winglet Embedded Fine Grid System
- Winglet Spanwise Load, Moment and Drag Distributions
- Winglet Area, Average Chord
- Winglet C_L, C_M, C_D, $C_{D_{FRICTION}}$
- Pod/Nacelle Pressure Coefficients (see Figure A-5 for angular argument sign conventions)

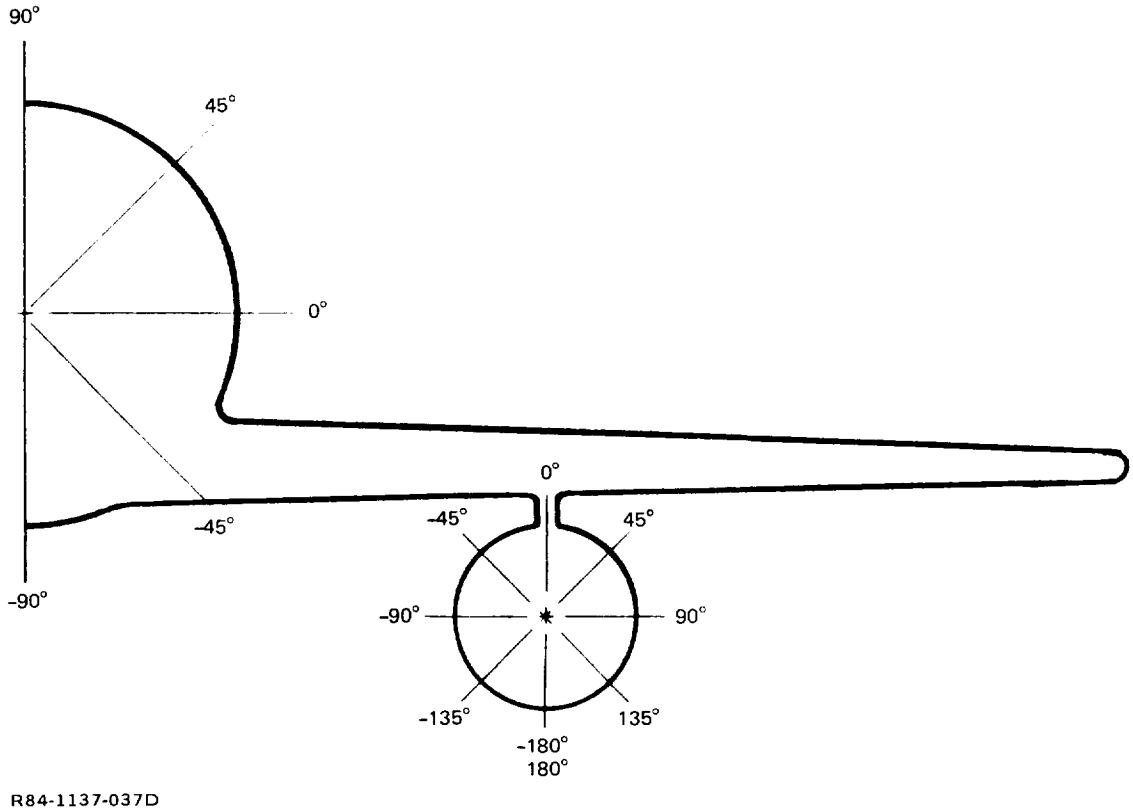

Figure A-5 Sign Convention for Angular Argument of Fuselage/Nacelle Pressure Output Stations

- Pod/Nacelle Surface and Projected Areas
- Pod C_L, C_M, C_D, $C_{D_{FRICTION}}$
- Pylon Surface Area and Friction Drag
- Wing Pressure Drag $C_{D_{P(w)}}$
- Wing Friction Drag $C_{F_{WING}}$
- Body Grid Mach Chart
- Body Angular Cut Pressure/Velocity Distribution
- Body Longitudinal Load and Drag Distribution
- Body Length, Wetted Area, Projected Area, Max. Cross-sectional Area, Reynolds Number based on body length
- Total Body $C_{L_{BODY}}$, $C_{M_{BODY}}$, $C_{D_{P(b)}}$
- Body Pressure Drag $C_{D_{P(b)}}$
- Body Friction Drag C_{F_B}
- Total Configuration C_L, C_M, C_D
- Wing-Body Wave Drag $C_{D_{WAVE}}$
- Wing-Body Friction Drag C_F
- Wing-Body Lift-Induced Drag C_{D_I}
- Wing-Body Spanload Efficiency Factor E

Plotted Output

The plot output can be divided into two separate sections.

Section I (Input Geometry Verification)

- Title/Case/Flow condition Label
- Body Cross-Sections
- Input Wing Sections
- Configuration Planview
- Configuration Head-On View

Section II (Computed Results)

- Superimposed wing pressure distributions (upper/lower surface) with total wing C_L, C_M, C_D label.
- Wing planform with section shapes at computed span stations.

- Detailed wing section pressure distributions with Section C_ℓ, C_m, C_d label.
- Detailed Winglet Pressure Distributions with Section C_ℓ, C_m, C_d label
- Detailed Pod/Nacelle Pressure Distributions
- Detailed body angular cut pressure distributions.
- Body longitudinal load plot with body C_{L_B}, C_{M_B}, C_{D_B} and wing-body C_L, C_M, C_D label.
- Wing-body spanload plot with span efficiency, lift-induced drag, wave drag, friction drag label.

INPUT GEOMETRY VERIFICATION

Coding for graphical inspection of input wing and body geometry has been included. Since the program requires considerable computer time and core storage to operate and some facility budgets may not provide for a number of error-filled submittals, it is recommended that the geometry verification mode of operation be used before submitting a complete and expensive relaxation solution. The graphic output coupled with printed output for geometry and grid systems should be sufficient to diagnose user input errors. In particular, it has been found advantageous to make the geometry check and perform a single crude and a single fine grid iteration (very cheap) to check code flow before a complete analysis is performed.

The body cross-section array is first to be plotted after case title and flow conditions are listed (see Figure A-6). In this case, an error in specifying a Z-coordinate of the canopy top centerline is apparent. In Figure A-7, an error in specifying a Y-coordinate of the windshield base is illustrated. Finally, Figure A-8 illustrates the corrected and final shape of the fuselage to be analyzed.

The defining wing chord sections are displayed after the body geometry (see Figure A-9). Each is plotted to a ten inch chord so errors in coordinates will become visible. It is important to note that there is no mapping involved in the present method; thus, no coordinate smoothing or manipulation is employed. Irregularities in input coordinates will cause oscillations in computed pressure distributions.

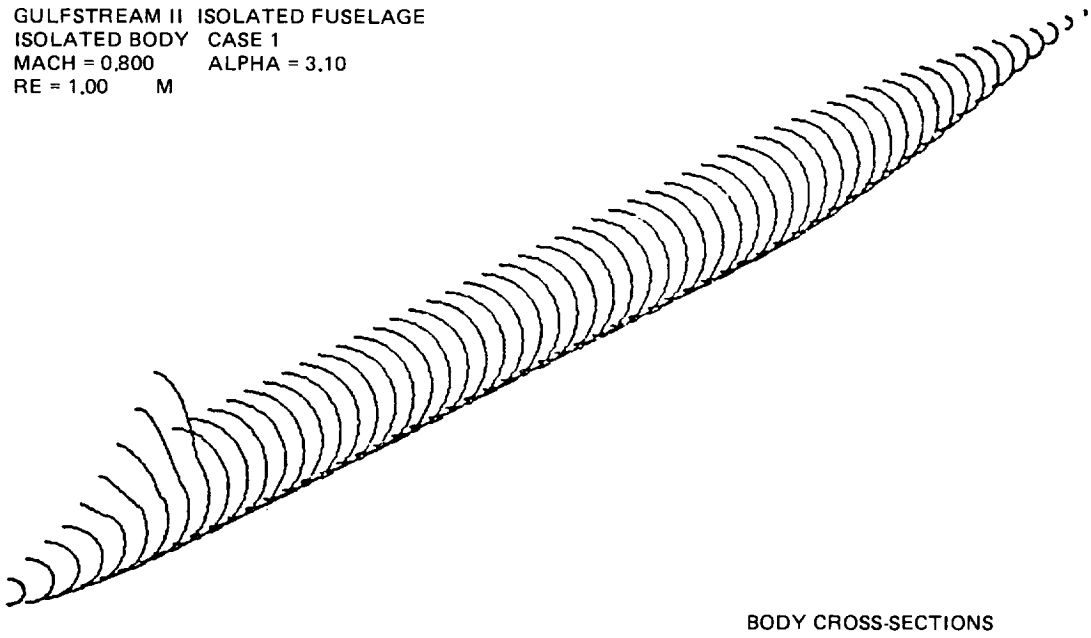

Figure A-6 Sample Input Geometry Verification Plot with Error in Z-Coordinate of Canopy Definition

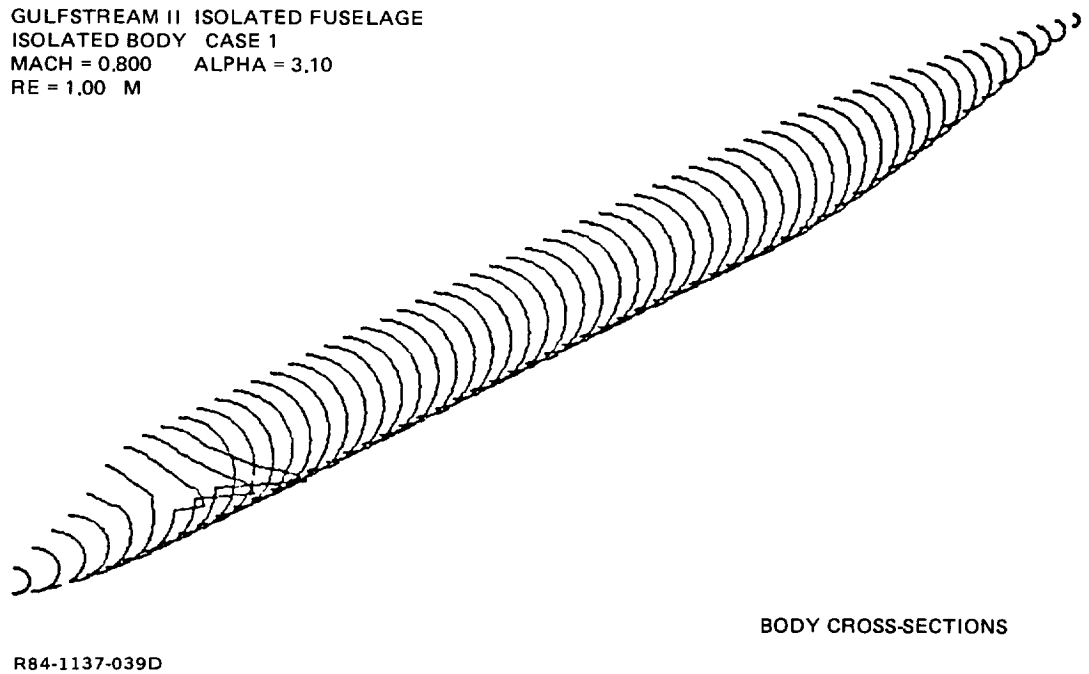

Figure A-7 Sample Input Geometry Verification Plot with Error in Y-Coordinate of Canopy Definition

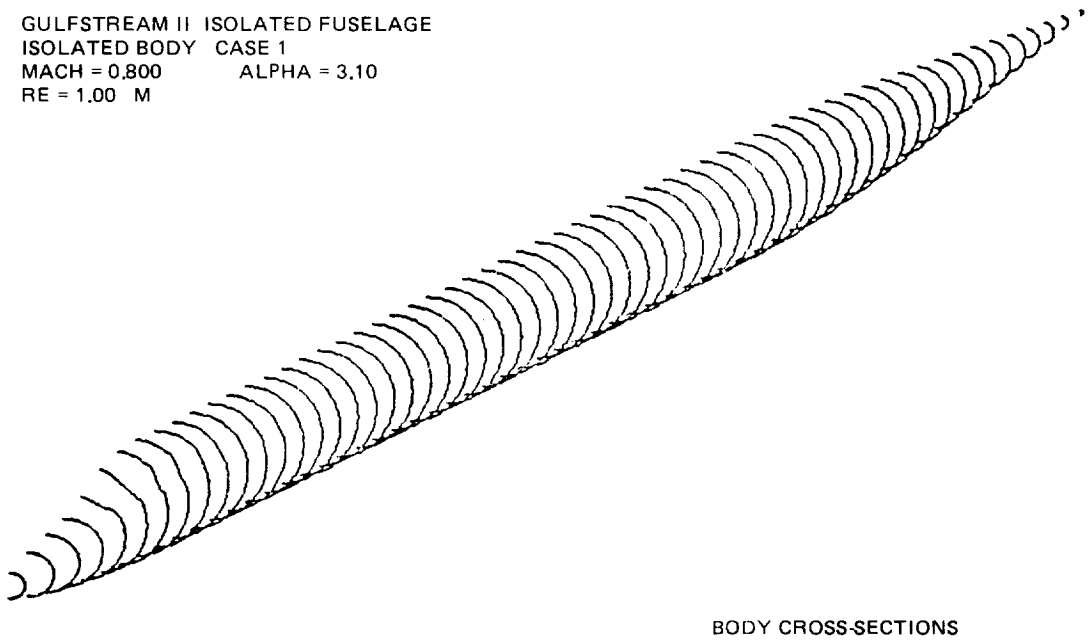

R84-1137-040D

Figure A-8 Sample Input Geometry Verification Plot for Fuselage

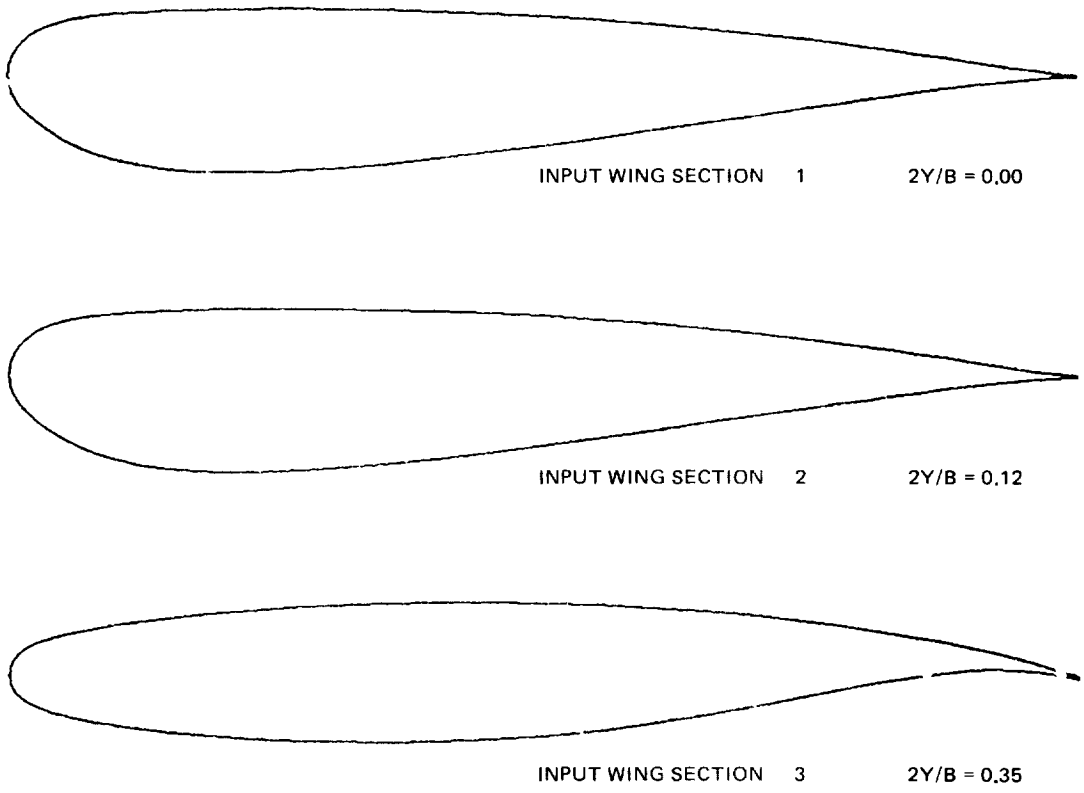

R84-1137-041D

Figure A-9 Sample Input Geometry Verification Plot for Wing Sections

A configuration plan-view will follow the wing section figures. This should be used to insure that the wing planform is properly defined and its placement on the fuselage is correct (see Figure A-10). Finally, a head-on view is plotted (see Figure A-11). Once again, check to see that the wing and body are indeed attached. Geometry verification plots which illustrate typical nacelle, pylon and winglet positioning checkouts can be seen in Figure A-12.

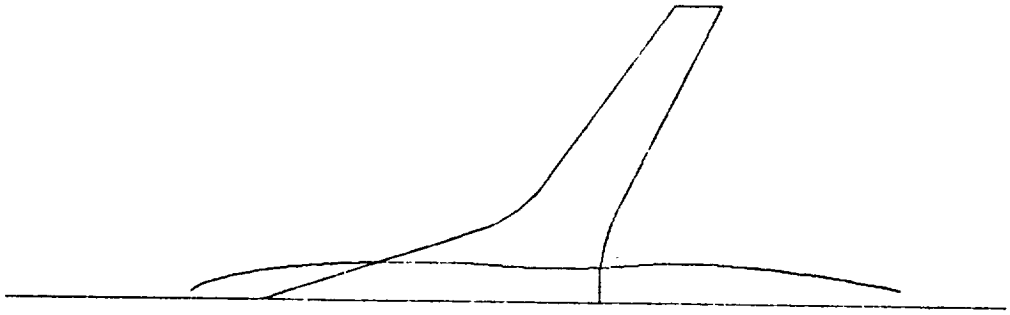

R84-1137-042D

Fig. A-10 Sample Input Geometry Verification Plot, Plan View

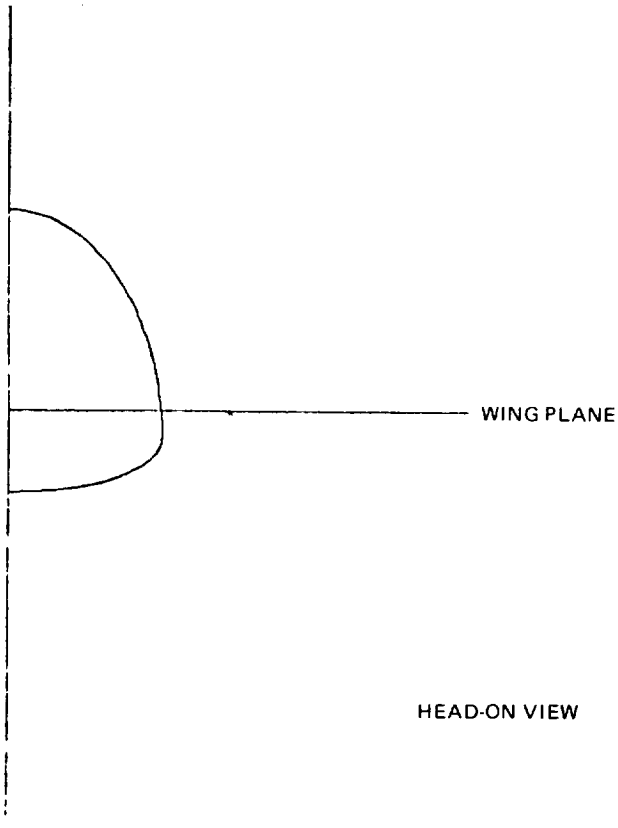

R84-1137-043D

Fig. A-11 Sample Input Geometry Verification Plot, Head-On View

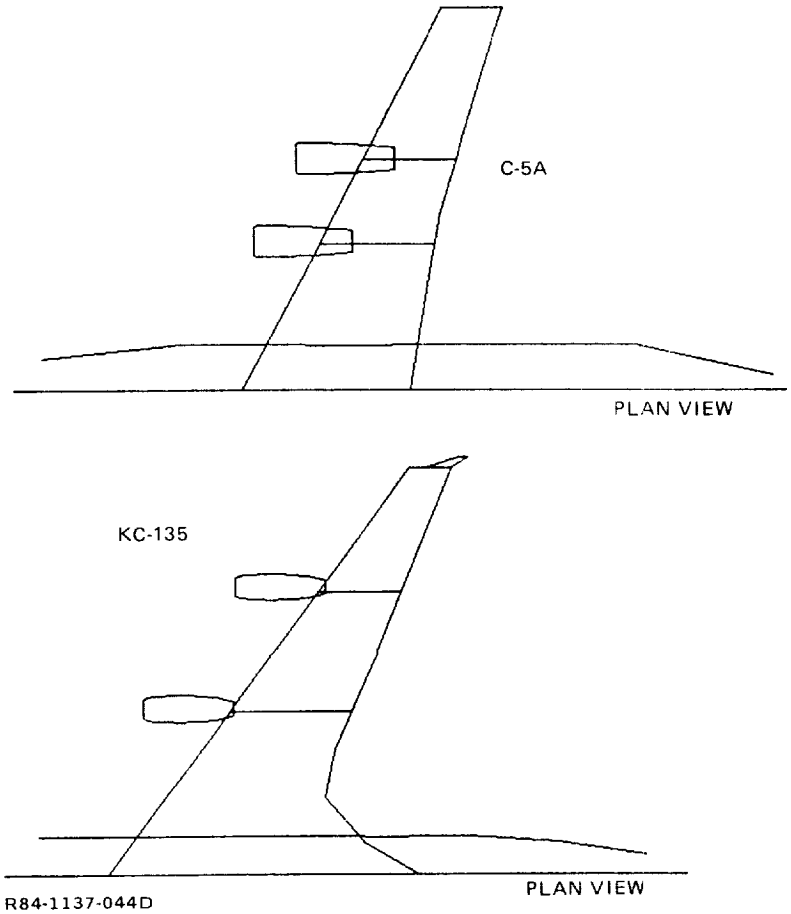

Fig. A-12 Sample Geometry Verification Plots for Configuration with Nacelles, Pylons and Winglets

SUBROUTINE CALL SEQUENCE

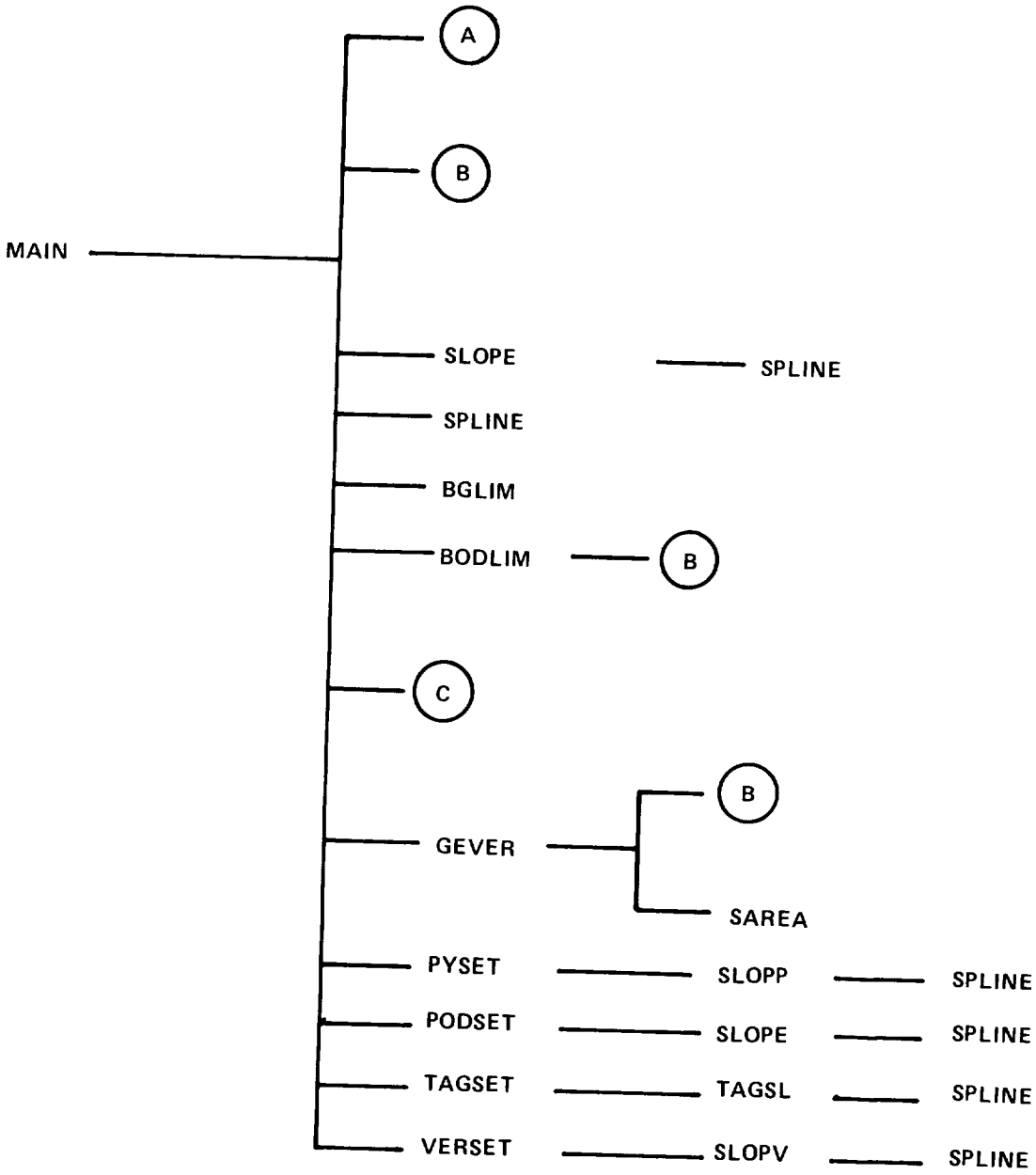

NOTE:

A FUSELAGE GEOMETRY DEFINITION

B FUSELAGE GEOMETRY INTERROGATION

C RELAXATION/BOUNDARY LAYER ROUTINES

SUBROUTINE CALL SEQUENCE (A)

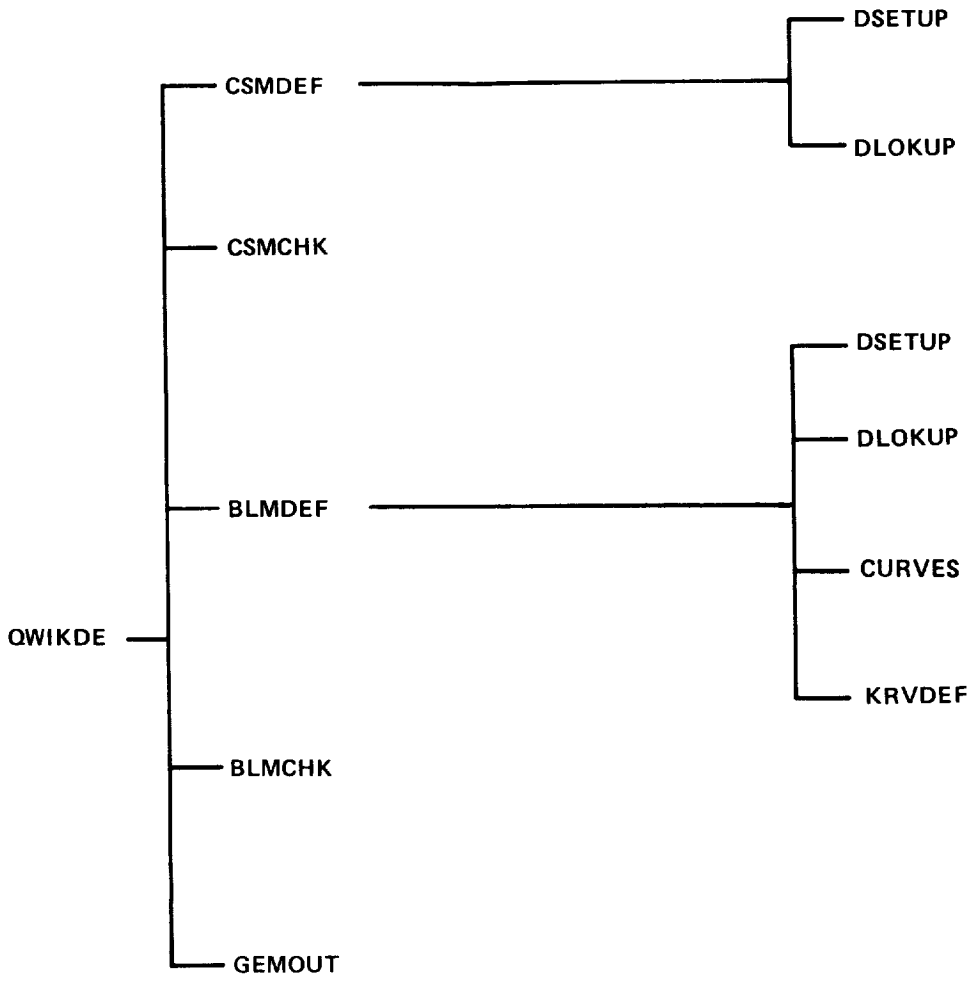

SUBROUTINE CALL SEQUENCE (B)

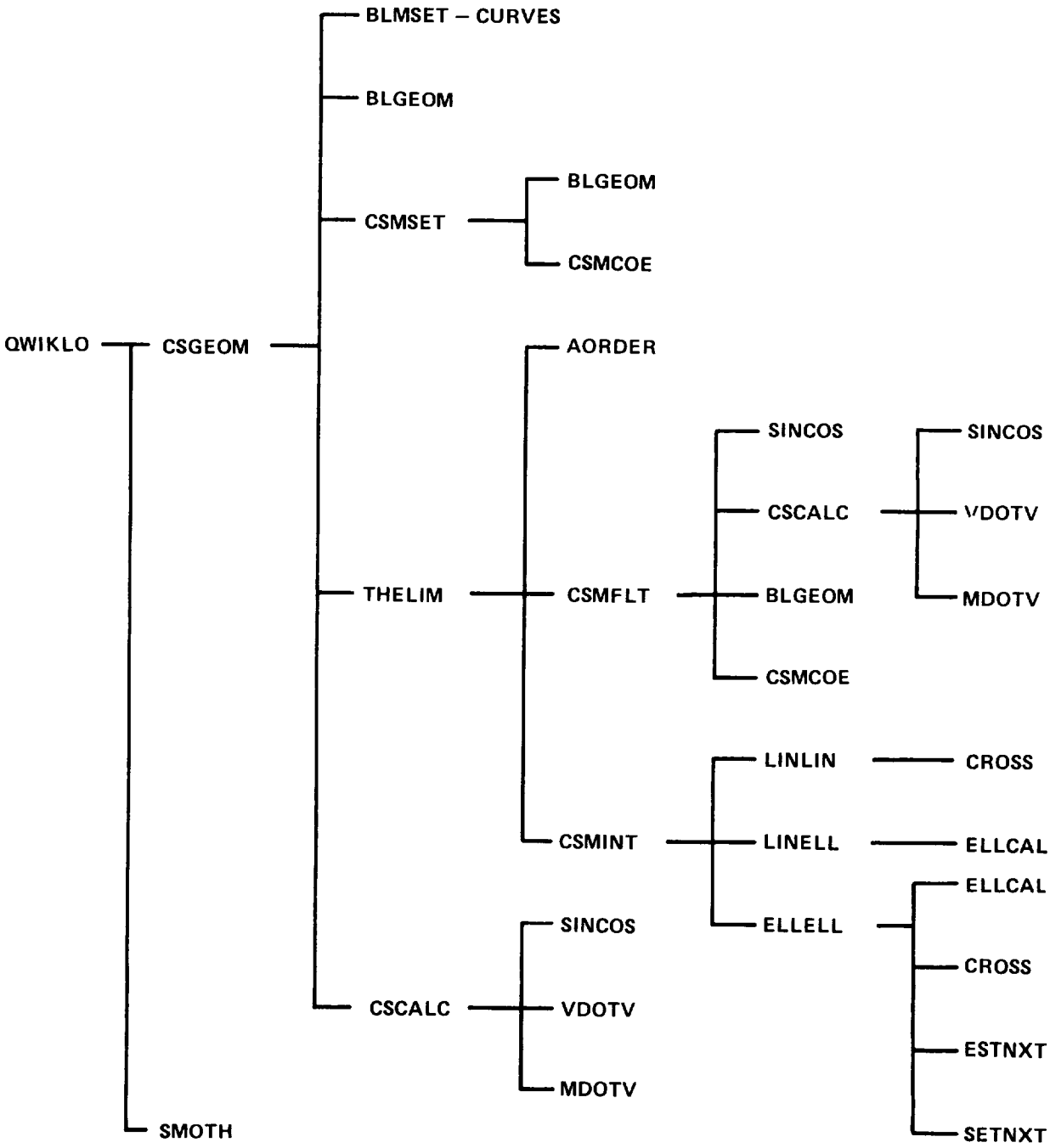

SUBROUTINE CALL SEQUENCE (C)

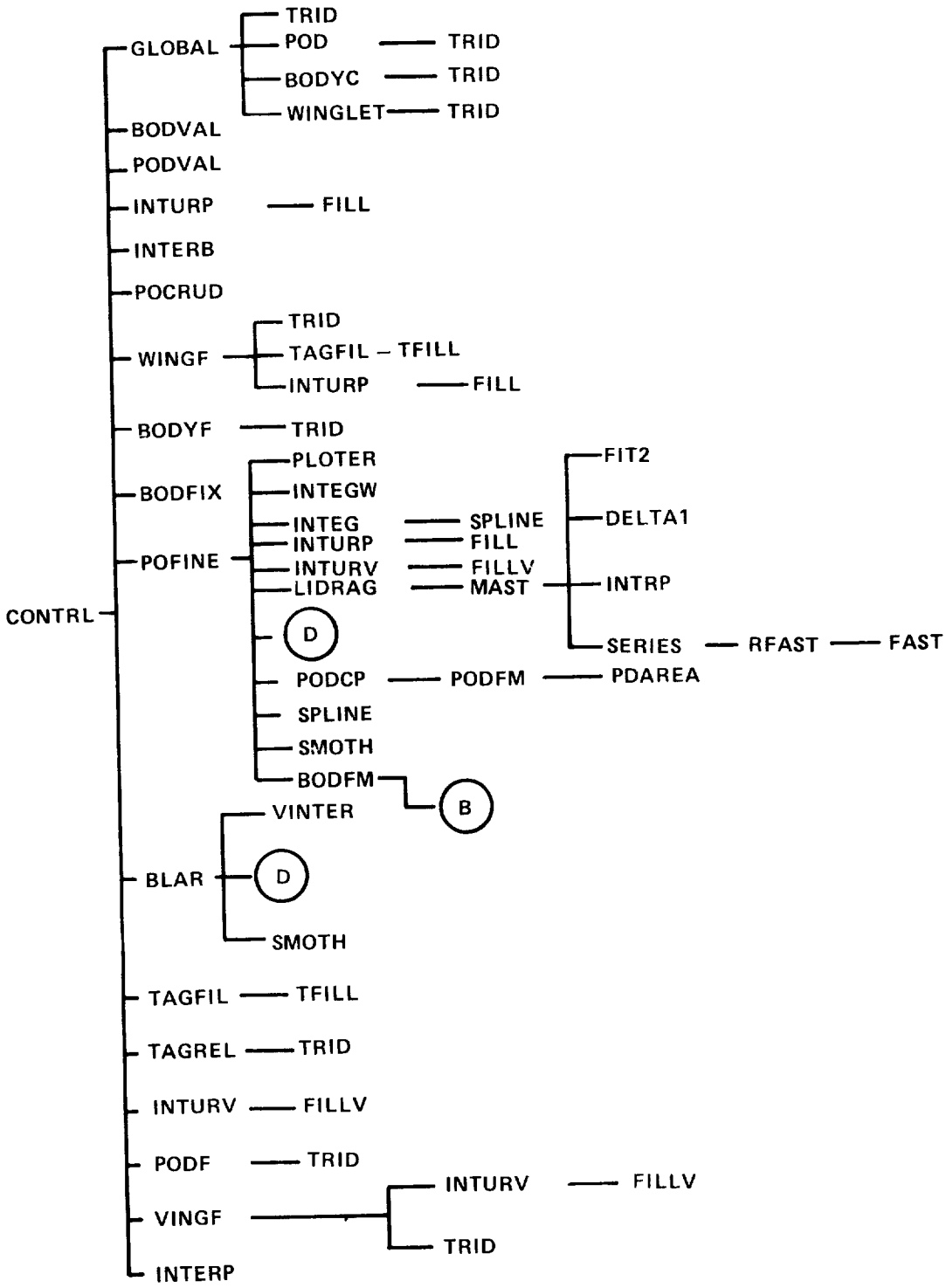

SUBROUTINE CALL SEQUENCE (D)

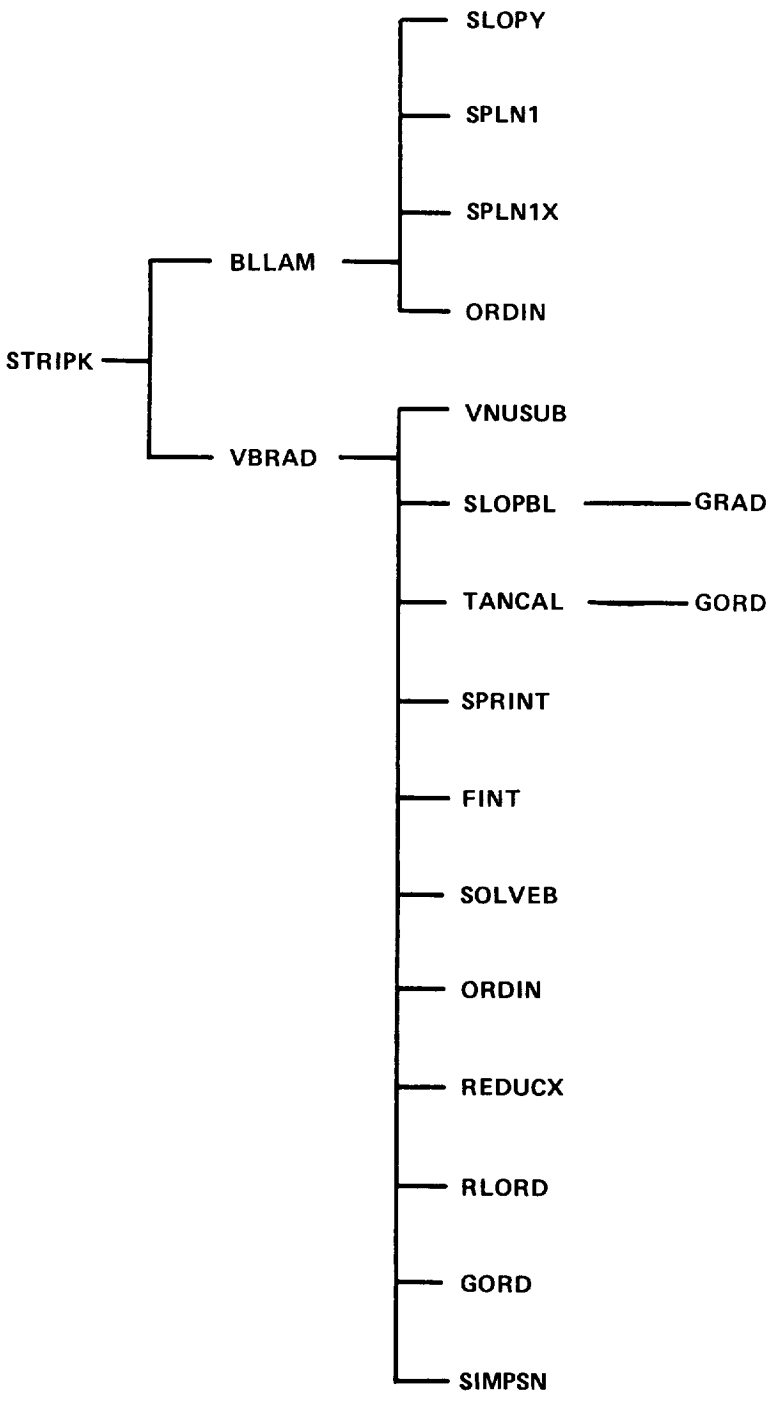

SUBROUTINE DESCRIPTION

AORDER	Orders a set of numbers by permutation index
BGLIM	Computes wing fixed potential surface limiters in fine embedded body grid
BLAR	Main control routine for laminar and turbulent modified chordwise boundary layer calculation. Computes boundary layer displacement thickness (δ^*) slope for viscous/inviscid interaction mode of operation
BLGEOM	Assigns body line model values and derivatives to control point coordinates
BLLAM	Computes Thwaites laminar boundary layer with Rott and Crabtree compressibility modification
BLMCHK	Correlates and checks the input data deck and the indices for the generated body line math models
BLMDEF	Defines body line models from the input data
BLMSET	Controls the determination values and first and second derivatives for all body line models at a given x-station
BODFIX	Computes potentials on fixed wing/wake surface in body fine grid given solution in fine wing grid and global crude grid
BODFM	Computes integrated body force and moment coefficients
BODLIM	Computes J and K limiters for body boundary in both crude and fine grid systems
BODVAL	Computes body boundary point potential values

BODYC	Finite difference approximations and relaxation solution for body boundary in crude grid
BODYF	Finite difference approximations and relaxation solution for fine body grid
CONTRL	Main control routine for relaxation solution of governing equation, interpolation, boundary layer analysis and printed/plotted output
CROSS	Solves for the intersection of two lines in a plane
CSCALC	Computes radial position and derivatives for specified cross-section model, arc, and θ'
CSGEOM	Is the main subroutine in the look-up portion of the QUICK System. It is called to establish $r' = f(\theta', x)$. It calls appropriate subroutines to evaluate body line values and construct cross-section geometry at a given x-station. It is used for all geometry model interrogation
CSMCHK	Correlates and checks the input data deck and the indices for the cross-sectional math model
CSMCOE	Composes the equations which are to define the cross-section geometry at a given station
CSMDEF	Logically defines the cross-section models from the input data
CSMFLT	Creates control point definitions to permit the insertion of a smooth fillet between cross-sectional arcs
CSMINT	Locates user specified intersections between cross-sectional arcs and adjusts their use-theta limits

CSMSET	Sets up the control point coordinate arrays used to define the cross-section geometry at a specified x-station
CURVES	Calculates values and first and second derivatives for individual curve fits
DELTA1	Interpolation routine for wing spanload
DLOKUP	Is a simple look-up routine. It assigns an index to match an input name to a codeword list, but is not capable of adding new items to that list
DSETUP	Is an adapting dictionary look-up routine. New items are added to a codeword list, an index (counter) is returned for the codeword, and an indicator (INEW) is set equal to 1 when a new item is encountered
ELLCAL	Set up for ellipse
ELLELL	Calculates intersection of two ellipses
ESTNXT	Estimates non-linear root by modified inverse quadratic
FAST	Fast Fourier transform of complex data
FILL	Performs interpolation controlled by INTURP
FILLV	Assists INTURV interpolation process
FINT	Simultaneous triple interpolation
FIT2	Determines cubic spline fit coefficients for input spanload distribution

GEMOUT	Ensures that all body lines required by a cross-sectional model are defined for the range of that model
GEVER	Controls geometry verification plotting
GLOBAL	Finite difference approximations and relaxation solution for global crude grid
GORD	Bradshaw's G function
GRAD	Slope of a function at its tabulated points
INTEG	Integrates wing load distributions for lift, moment and drag coefficients
INTEGW	Intergrates winglet section coefficients to obtain total lift, moment and drag
INTERB	Interpolation routine for body fine/global crude grid communication
INTERP	Interpolation for pod crude/fine grid interaction
INTRP	Converts input spanload distribution to a fine over spaced distribution
INTURP	Controls interpolation for filling fine mesh points using crude grid potential values. Updates crude mesh given fine solution. Updates fine mesh given crude solution
INTURV	Interpolation for winglet fine/TAG/crude interaction
KRVDEF	Calculates coefficients for the various curve fits associated with body line math models

LIDRAG	Main control routine for computing lift induced drag efficiency "E" using a Fourier analysis
LINELL	Solves for the intersection of a line and an ellipse
LINLIN	Solves for intersection of two lines
MAIN	Controls reading of input data and sets boundary and initial conditions. Sets up arrays and storage areas. Sets up crude and wing and body fine coordinate systems
MAST	Controls cubic spline fit for interpolation of input spanload distribution
MDOTV	Performs matrix multiplication of a vector
ORDIN	Linear interpolation
PDAREA	Computes pod surface and projected areas
PLOTER	Controls all graphic output (except input geometry verification)
POCRUD	Prints results in global crude grid; mach chart, wing upper/lower surface pressure coefficients
POD	Pod crude grid relaxation process
PODCP	Compute pod/nacelle pressure coefficients
PODF	Pod/nacelle fine grid relaxation process
PODFM	Computes pod/nacelle forces and moments
PODSET	Set up for pod/nacelle simulation. Pod geometry input

PODVAL	Computes pod/nacelle boundary condition for crude and fine grid
POFINE	Prints output results for fine grid arrays
PYSET	Set up for pylon surface simulation. Pylon geometry input
QWIKDE	Main control routine for Quick-Geometry definition and check out
QWIKLO	Main control routine for interrogation of Quick-Geometry math model
REDUCX	Performs interpolation to new grid
RFAST	Fast Fourier transforms of real data
RLORD	Bradshaw's L function
SAREA	Computes body surface area given an array of cross-sections
SERIES	Determines Fourier series coefficients
SETNXT	Reorders points for non-linear root finder
SIMPSN	Simpson's rule integration
SINCOS	Adjusts input interrogation angles for top and bottom dead center
SLOPP	Computes pylon boundary conditions
SLOPV	Computes winglet boundary conditions
SLOPBL	Slope of a tabulated function at an arbitrary point

SLOPE	Computes boundary conditions for wing surface and axisymmetric bodies
SLOPY	Computes wing surface slopes
SMOTH	Function for smoothing an array of values
SOLVEB	Solution of two simultaneous linear algebraic equations
SPLINE	Computes a cubic spline through a set of points
SPLN1	Computes continuous derivatives interpolation by means of a cubic fit
SPLN1X	Entry for special cases requiring extrapolation beyond ends of X and Y tables
SPRINT	Prints output of profile results
STRIPK	Starting condition setup and flow control for laminar/turbulent boundary layer prediction
TAGFIL	Interpolation for TAG/crude grid interaction
TAGSET	Set up for wing tip augmentation grid TAG
TAGSL	Computes wing boundary conditions for TAG
TAGREL	Relaxation process for TAG
TANCAL	Computes characteristic angles for use in B.L. solution (equation 21 of Bradshaw and Ferriss)
TFILL	Assists TAGFIL interpolation process

THELIM	Creates and controls use-theta arrays to establish continuity in the cross-section model
TRID	Solves tri-diagonal matrix
VBRAD	Computes Bradshaw compressible 2-D turbulent boundary layer simulating 3-D boundary layer on infinite yawed wing by Nash-Tseng modified chord technique
VDOTV	Computes a vector dot product
VERSET	Set up for winglet fine embedded grid system. Winglet geometry input
VINGF	Winglet fine embedded grid relaxation process
VINTER	Performs cubic δ^* fit for separated boundary layer in wing section cove regions
VNUSUB	Computes the Nash effective viscosity
WINGF	Finite difference approximations and relaxation solution for wing fine grid
WINGLET	Crude grid relaxation process for winglet in crude grid system

KEY VARIABLE DESCRIPTIONS

This description of key program variables and constants which are located in several common blocks will be useful in understanding flow logic.

VARIABLE	DESCRIPTION
AK	The value $1-M^2$
ALAM	Wing taper ratio (λ)
ALPHA	Angle-of-attack (radians)
AMAC	Wing mean aerodynamic chord (MAC)
AMACH	Mach number
AM2	The value M^2
AOA	Angle-of-attack (degrees)
AR	Wing aspect ratio (AR)
BAREA	Body wetted area
BCF	Body skin friction coefficient
BCL	Wing crude grid lower boundary slopes
BCLF	Wing fine grid lower boundary slopes
BCLP	Pylon outboard boundary condition
BCLT	Wing lower surfaee boundary condition in TAG
BCLV	Winglet outboard boundary condition

VARIABLE	DESCRIPTION
BCU	Wing crude grid upper boundary slopes
BCUF	Wing fine grid upper boundary slopes
BCUP	Pylon inboard boundary condition
BCUT	Wing upper surface boundary condition in TAG
BCUV	Winglet inboard boundary condition
BNOSE	X coordinate of body nose
BNOSEP	X coordinate of pod/nacelle nose (input as BNOSE 1)
BODCD	Body (integrated) drag coefficient
BODCL	Body (integrated) lift coefficient
BODCM	Body (integrated) moment coefficient
BPAREA	Body projected area
BS	Body plot scaling coefficient
BTAIL	X coordinate of body tail
BTAILP	X coordinate of pod/nacelle tail (input as BTAIL 1)
CA	Global crude grid stretching coefficient (ξ_x)
CAV	Wing average chord (C_{AV})
CAVW	Winglet average chord

VARIABLE	DESCRIPTION
CB	Global crude grid stretching coefficient (ξ_{xx})
CC	Global crude grid stretching coefficient (η_y)
CCT	TAG stretching coefficient (η_y)
CD	Global crude grid stretching coefficient (η_{yy})
CDI	Lift induced drag coefficient
CDINT	Wing section integrated drag
CDINW	Winglet section drag coefficients
CDT	TAG stretching coefficient (η_{yy})
CE	Global crude grid stretching coefficient (ζ_z)
CET	TAG stretching coefficient (ζ_z)
CF	Global crude grid stretching coefficient (ζ_{zz})
CFINT	Integrated wing section friction coefficient
CFT	TAG stretching coefficient (ζ_{zz})
CIR	Wing circulation (Γ)
CIRPC	Pylon circulation at crude grid vertical cuts
CIRPY	Pylon circulation at fine grid vertical cuts
CIRV	Winglet circulation at vertical span cuts

VARIABLE	DESCRIPTION
CIRVC	Winglet circulation at crude grid vertical cuts
CLINT	Wing section integrated lift
CLINW	Winglet section lift coefficients
CMINT	Wing section integrated moment
CMINW	Winglet section moment coefficients
CMLOC	Wing section integrated moment about local quarter chord
CMLOW	Winglet section local moment coefficients
CPL	Wing lower surface pressure coefficient
CPU	Wing upper surface pressure coefficient
CPUPOD	Pod pressure coefficients
CSCUT	Body x station for cross-sectional cut
DELSL	Wing boundary layer slopes for section lower surface
DELSU	Wing boundary layer slopes for section upper surface
DETA	Global crude grid mesh spacing in η direction
DIM	Configuration length for non-dimensionalizing maximum potential updates
DRDXC	Axisymmetric body slope distribution in crude grid

VARIABLE	DESCRIPTION
DRDXCP	Pod/nacelle boundary condition
DRDXF	Axisymmetric body slope distribution in fine grid
DRDXFP	Pod fine grid boundary condition
DXB	Fine body grid mesh spacing in X direction
DXBP	Fine pod grid mesh spacing in X direction
DXI	Global crude grid mesh spacing in ξ direction
DXV	Winglet fine grid mesh spacing in X direction
DXW	Fine wing grid mesh spacing in X direction
DYB	Fine body grid mesh spacing in Y direction
DYBP	Fine pod grid mesh spacing in Y direction
DYV	Winglet fine grid mesh spacing in Y direction
DYW	Fine wing grid mesh spacing in Y direction
DZB	Fine body grid mesh spacing in Z direction
DZBP	Fine pod grid mesh spacing in Z direction
DZETA	Global crude grid mesh spacing in ζ direction
DZW	Fine wing grid mesh spacing in Z direction

VARIABLE	DESCRIPTION
E	Wing spanload efficiency
ETA	η coordinates for global crude grid (transformed space)
ETAT	TAG η coordinates
FMFR	Nacelle inlet mass flow ratio
FNPR	Nacelle exhaust nozzle pressure ratio
G	The value $(\gamma+1)M^2$
H	The value $(\gamma-1)M^2$
IBGI	Crude grid I value of body grid inner overlap region forward boundary
IBGIP	Crude grid I value at pod fine grid forward boundary
IBGL	Crude grid I value of body grid inner overlap region aft boundary
IBGLP	Crude grid I value at pod fine grid aft boundary
IL	Crude grid wing leading edge I value
ILEF	Wing fine grid leading edge I value
ILEV	Fine grid winglet leading edge I value
ILT	TAG wing leading edge I value
ILV	TAG winglet leading edge I value
ILVC	Crude grid winglet leading edge I value

VARIABLE	DESCRIPTION
IMACH	Code for subsonic (0) or supersonic (1) flow at a grid point
IMAX	Maximum number of crude grid points in X direction
IMAXB	Maximum number of fine body grid points in X direction
IMAXBP	Maximum number of fine pod grid points in X direction
IMAXV	Maximum number of winglet fine grid points in X direction
IMAXW	Maximum number of fine wing grid points in X direction
INOSE	Fine body grid I value at body nose
INOSEC	Crude grid I value at body nose
INOSEP	Crude grid I value at pod nose
INOSPF	Fine grid I value at pod nose
IPTYPE	Nacelle type - closed body/hot jet/cold jet
IT	Crude grid wing trailing edge I values
ITAGI	Crude grid I limiter for forward TAG boundary
ITAGIT	On/off code for wing tip augmentation grid (TAG)
ITAGL	Crude grid I limiter for aft TAG boundary
ITAIL	Fine body grid I value at body tail
ITAILC	Crude grid I value at body tail

VARIABLE	DESCRIPTION
ITAILP	Crude grid I value at pod tail
ITALPF	Fine grid I value at pod tail
ITEF	Wing fine grid trailing edge I value
ITER	Iteration count
ITEV	Fine grid winglet trailing edge I value
ITMAX	Maximum number of TAG grid points in X direction
ITT	TAG I value of wing trailing edge
ITV	TAG I value of winglet trailing edge
ITVC	Crude grid I value of winglet trailing edge
JBG	Crude grid J value of body grid inner overlap region side boundary
JBGIP	Crude grid J value at pod fine grid inboard boundary
JBGLP	Crude grid J value at pod fine grid outboard boundary
JBY	Fine grid J value of winglet section plane
JMAX	Maximum number of crude grid points in Y direction
JMAXB	Maximum number of fine body grid points in Y direction
JMAXBP	Maximum number of fine pod grid points in Y direction
JMAXV	Maximum number of winglet fine grid Y-stations

VARIABLE	DESCRIPTION
JNOSEP	Crude grid J value at pod position
JROOT	Crude grid J value at wing root
JSD	Fine body grid J value at first influence of body boundary points
JSDC	Crude grid J value first influenced by body boundary point
JSDPL	Fine pod grid J limiter at pod side-left
JSDPR	Fine pod grid J limiter at pod side-right
JTAGI	Crude grid J limiter for inboard TAG boundary
JTAGO	Crude grid J limiter for outboard TAG boundary
JTIP	Crude grid J value at wing tip
JTIPT	TAG J value at wing tip
JTMAX	Maximum number of TAG grid points in Y direction
KBB	Fine body grid K value at wing plane
KBC	Crude grid K value at wing plane
KBGL	Crude grid K value of body grid inner overlap region (lower)
KBGLP	Crude grid K value at pod fine grid lower boundary
KBGU	Crude grid K value of body grid inner overlap region (upper)
KBGUP	Crude grid K value at pod fine grid upper boundary

VARIABLE	DESCRIPTION
KBOD	Code for body in crude grid (0) or fine embedded grid (1)
KBW	Fine wing grid K value at wing plane
KLOC	Crude grid K limiters for body surface (lower)
KLOF	Fine grid K limiters for body surface (lower)
KLOPF	Nacelle fine grid lower surface K limiters
KMAX	Maximum number of crude grid points in Z direction
KMAXB	Maximum number of fine body grid points in Z direction
KMAXBP	Maximum number of fine pod grid points in Z direction
KMAXW	Maximum number of fine wing grid points in Z direction
KNOSEP	Crude grid K value at pod position
KODB	Body option code...cylinder, axisymmetric, arbitrary body (input as BKOD)
KOPOD	Number of pods/nacelles (input as POD)
KOPY	Number of pylon surfaces (input as PY)
KOVER	Number of winglets (input as VER)
KPLO	Crude grid lower K limit of pylon surface
KT	TAG K value of wing plane

VARIABLE	DESCRIPTION
KTAGL	Crude grid K limiter for lower TAG boundary
KTAGU	Crude grid K limiter for upper TAG boundary
KTC	Crude grid K value at winglet tip
KTIPV	TAG winglet tip K value
KTMAX	Maximum number of vertical (Z) points in TAG
KUPC	Crude grid K limiters for body surface (upper)
KUPF	Fine grid K limiters for body surface (upper)
KUPPF	Nacelle fine grid upper surface K limiters
MAXIT	Maximum number of initial crude grid iterations (input as AXIT)
MAXITF	Maximum number of crude/fine grid cycles (input as AXITF)
MODV	Mode of operation for viscous effects (input as VISMOD)
NCASE	Case description...wing, body or wing-body case (input as CASE)
NINB	Number of ordinates defining axisymmetric body shape (input as BNIN)
NINBP	Number of pod ordinates defined (input as BNIN 1)
NINP	Number of ordinates defining each pylon section (input as PIN)
NINV	Number of ordinates defining each input winglet section (input as VIN)

VARIABLE	DESCRIPTION
NINW	Number of ordinates defining each wing section (input as ANIN)
NOSEB	Blunt/sharp nose body code (for spline fit)
NOSEBP	Sharp/blunt nose shape code for pods
NOSEW	Blunt/sharp nose wing code (for spline fit)
NOSP	Pylon sharp/blunt nose code
NOSW	Sharp/blunt winglet section nose shape code
NPOA	Number of fine X-grid points between leading and trailing edge of each wing section
NPOB	Number of fine body X-grid points between nose and tail of body
NPSEC	Number of defining pylon sections (input as PSEC)
NSECT	Number of defining wing sections (input as ASECT)
NTC	Number of points representing body cross-sections in crude grid
NTF	Number of points representing body cross-sections in fine body grid
NTOTAL	Total number of crude grid points in single X-Z plane
NTOTB	Total number of fine body grid points in single X-Z plane
NTOTV	Total number of fine winglet grid points in single X-Y plane

VARIABLE	DESCRIPTION
NTOTW	Total number of fine wing grid points in single X-Z plane
NVSEC	Number of winglet sections defined (input as VSEC)
NWPO	Code for print out of crude grid results for diagnostic purposes
PAREA	Pod surface area
PBL	Fine body grid wing/wake lower surface potentials
PC1	Global crude grid potential (ψ) arrays (Note: Only three planes are in core at one time)
PC2	Global crude grid potential (ψ) arrays (Note: Only three planes are in core at one time)
PC3	Global crude grid potential (ψ) arrays (Note: Only three planes are in core at one time)
PCF	Pod/nacelle skin friction coefficient
PCL	Crude grid wing/wake lower surface potentials
PF1	Fine embedded wing and body potential arrays. (Note: Only three planes are in core at one time)
PF2	Fine embedded wing and body potential arrays. (Note: Only three planes are in core at one time)
PF3	Fine embedded wing and body potential arrays. (Note: Only three planes are in core at one time)

VARIABLE	DESCRIPTION
PFL	Fine wing grid lower surface potentials
PI	π
PLTAG	TAG wing lower surface potential array
PODALF	Pod/nacelle incidence relative to fuselage
PODBET	Pod/nacelle yaw angle
PODCD	Pod/nacelle drag coefficient
PODCL	Pod/nacelle lift coefficient
PODCM	Pod/nacelle moment coefficient
PPAREA	Pod projected area
PTAG	TAG field potential (ϕ) array
PVCL	Winglet outboard surface potential (ϕ) array for crude grid
PVL	Winglet fine embedded grid outboard surface potential (ϕ) array
PVTL	Winglet TAG outboard surface potential (ϕ) array
PYAREA	Pylon surface areas
PYLO	Pylon fine grid outboard surface potential (ϕ) array
PYLOC	Pylon crude grid outboard surface potential (ϕ) array
RADIUS	Radius of body cylinder (input option)

VARIABLE	DESCRIPTION
RAVC	Crude grid average body radius for boundary condition calculation
RAVF	Fine grid average body radius for boundary condition calculation
RC	Axisymmetric body radius distribution in crude grid
RCP	Radii for pod surface after positioning
RE	Freestream Reynolds number
RF	Axisymmetric body radius distribution in fine grid
RFP	Pod radii in fine grid
RIN	Radial coordinates defining axisymmetric body (input option)
RINP	Radial coordinates defining axisymmetric pod
RMAX	Body maximum radius for computational body surface
RMAXP	Pod maximum radius
SDD	Wing spanwise drag coefficient $\frac{CC_d}{C_{AV}}$
SDW	Winglet spanwise drag coefficient $\frac{CC_d}{C_{AV}}$
SEXP	Wing exposed area

VARIABLE	DESCRIPTION
SFD	Wing spanwise friction coefficient $\frac{CC_f}{C_{AV}}$
SGRAD	Body side slope at wing-body juncture
SLD	Wing span load coefficient $\frac{CC_\ell}{C_{AV}}$
SLW	Winglet spanwise load coefficient $\frac{CC_\ell}{C_{AV}}$
SMD	Wing spanwise moment coefficient $\frac{CC_m}{C_{AV}}$
SMW	Winglet spanwise moment coefficient $\frac{CC_m}{C_{AV}}$
TCIR	Wing circulation at TAG wing span cuts
TDX	TAG Δ X spacing
TDY	TAG Δ Y spacing
TDZ	TAG Δ Z spacing
THETC	Body crude grid angular cuts
THETF	Body fine grid angular cuts
THETFP	Angular cuts for pod boundary points
TITLE	Case title for identifying graphic and printed output
TLE	Wing leading edge X value at TAG span cuts
TPIST	Pylon yaw incidence or twist

VARIABLE	DESCRIPTION
TSLOC	Wing local sweep angle at wing fine grid boundary points
TTE	Wing trailing edge X value at TAG span cuts
TVIST	Winglet section incidence angle or twist
TWIST	Wing twist (incidence) distribution
VANGL	Winglet cant angle, measured from wing plane
VAREA	Winglet area
VCD	Winglet drag coefficient
VCL	Winglet lift coefficient
VCLE	Crude grid X value of winglet leading edge
VCM	Winglet moment coefficient
VCTE	Crude grid X value of winglet trailing edge
VLE	Winglet leading edge X value after positioning
VTE	Winglet trailing edge X value after positioning
W	Relaxation factor ω
WAREA	Wing area S_W
WCD	Wing drag coefficient

VARIABLE	DESCRIPTION
WCF	Wing friction drag coefficient
WCL	Wing lift coefficient
WCM	Wing moment coefficient
WCORD	Wing section local chord length
WS	Wing plot scaling coefficient
X	X coordinate for global crude grid (physical space)
XBF	X coordinate for body fine grid
XBFP	Fine pod grid X array
XI	ξ coordinate for global crude grid (transformed space)
XILE	ξ coordinate of local wing section leading edge
XINB	X coordinates defining axisymmetric body (input option)
XINBP	X coordinates defining axisymmetric pod
XINP	X ordinates defining pylon
XINV	X ordinates defining winglet section
XINW	X ordinates defining wing section
XITE	ξ coordinate of local wing section trailing edge
XLE	X coordinate of local wing section leading edge
XLET	X coordinate of wing tip leading edge

VARIABLE	DESCRIPTION
XMOM	Position about which configuration moments are computed
XNC	Body normal vector X direction at crude grid body points
XNCP	Pod normal vector X direction at crude grid points
XNF	Body normal vector X direction at fine grid body points
XNOSE	X coordinate of body nose repositioned in crude grid
XOL	Non-dimensional distance along body length and wing chord
XOLP	X stations for pod surface after positioning
XPL	X coordinate of input wing section leading edge
XPT	X coordinate of input wing section trailing edge
XSF	X coordinate defining wing section at each fine grid plane points
XTAG	TAG grid X array
XTAIL	X coordinate of body tail repositioned in crude grid
XTE	X coordinate of local wing section trailing edge
XTET	X coordinate of wing tip trailing edge
XVF	Winglet fine grid X array
XVL	X value of winglet leading edge at input stations

VARIABLE	DESCRIPTION
XVT	X value of winglet trailing edge at input stations
XWF	Fine embedded wing grid X coordinate
Y	Y coordinate for global crude grid (physical space)
YBF	Y coordinate for body fine grid
YBFP	Fine pod grid Y array
YBODYP	Y coordinate of pod/nacelle axis (input as YBODY 1)
YINL	Y ordinates defining lower wing section
YINLP	Y ordinates defining pylon outboard surfaces
YINLV	Y ordinates defining winglet outboard surface
YINU	Y ordinates defining upper wing section
YINUP	Y ordinates defining pylon inboard surfaces
YINUV	Y ordinates defining winglet inboard surface
YNC	Body normal vector Y direction at crude grid body points
YNCP	Pod normal vector Y direction at crude grid points
YNF	Body normal vector Y direction at fine grid body points
YOB	Wing span station (2Y/b)
YP	Y coordinate of input wing section trailing edge

VARIABLE	DESCRIPTION
YSF	Y coordinate defining wing section at each fine grid plane
YTAG	TAG grid Y array
YTIP	Y coordinate of wing tip
YV	Y value of winglet input stations
YVF	Winglet fine grid Y array
Z	Z coordinate for global crude grid (physical space)
ZBF	Z coordinates for body fine grid
ZBFP	Fine pod grid Z array
ZBODYP	Z coordinate of pod/nacelle axis (input as ZBODY1)
ZETA	ζ coordinate for global crude grid (transformed space)
ZETAT	TAG ζ coordinates
ZNC	Body normal vector Z direction at crude grid body points
ZNCP	Pod normal vector Z direction at crude grid points
ZNF	Body normal vector Z direction at fine grid body points
ZOB	Winglet span station (y/b)
ZTAG	TAG grid Z array
ZWF	Fine embedded wing grid Z coordinate
ZWING	Wing height relative to center of body

APPENDIX B

USAGE/MODIFICATIONS FOR LaRC CDC/VPS-32 VERSION

The LaRC VPS-32 version of the WIBCO-PPW code, using VSOS 2.1.5 (opt = E) requires less than 1 million$_{10}$ storage for load and execution. Differences are noted as follow:

1. FILES USAGE

Thirteen (13) disk units are used, including one for a solution save/restart. The planar potential arrays are set up and accessed as table lookup in a large labeled common block, eliminating disk units 2, 3, 4, and 5 (units 12, 13, 14, and 15 of IBM code) by dummy READMS, WRITMS referencing. Several options are available for the solution save/restart capability, using unit 7 (unformatted data). Data needed by a separate plot program are saved on units 80, 82, 83, 87, 88 (all unformatted) and unit 9 (formatted).

2. UNIT 1 DATA INPUT

Through use of unit 1 data input the user can redefine certain key parameters that have been code-defined (hard coded). These code-defined values should be used initially to enhance the probability of proper execution for input geometry. Parameter values revert to default settings if keys for changes are not activated. Unit 1 data referenced in the information which follows use 8-field 10-digit format (8F10.0) with decimal point required. Default values for variables are included in the description for variables. The changes allowed are:

a) Number of fine x-grid points at wing tip is specified on Card 1-W rather than Card 2-W.

b) Save/restart of solution in the crude/fine grid only.

c) Redefinition of wing fine grid boundaries.

d) Redefinition of transition location at all span stations for viscous flow.

e) Redefinition of relaxation factors and interaction frequency in the general solution process.

The notation of appendix A for configuration indentification is used to indicate the card image modifications and additions for these allowed changes. Note that only the variables redefined from appendix A are included here.

CARD NUMBER	CARD COLUMN	VARIABLE NAME	DESCRIPTION
Card 2-A	1-10	CASE	|CASE| Key describing the type of configuration.
			CASE = 1. Isolated Body (omit cards -W).
			CASE = 2. Isolated Wing (omit cards -B).
			CASE = 3. Wing-Body.
			SGN (CASE) Trigger to control relaxation factors and interaction frequencies in general solution process.
			CASE > 0. Same as original input, no additional input required on Card 2-A-2.
			CASE < 0. Read additional input, Card 2-A-2.
	. . .		
	61-70	VISMOD	|VISMOD| Key describing extent of viscous effects.
			VISMOD = 1. No viscous effects.
			VISMOD = 2. Viscous effects computed at end of inviscid analysis.
			VISMOD = 3. Inviscid/viscous interaction.
			SGN (VISMOD) Trigger to redefine transition location, x/c, for viscous flow.
			VISMOD > 0. Same as original code-- no additional input required on Card 6-W.
			VISMOD < 0. Read additional input, Card 6-W.

CARD NUMBER	CARD COLUMN	VARIABLE NAME	DESCRIPTION	
Card 2-A (contd)	71-80	START	START = 0.	Conventional independent run (default).
			START = 1.	Save final solution at end of current AXITF iteration cycles.
			START = 2.	Restart solution at previous AXITF+1 iterations; do not save final solution.
			START = 3.	Restart solution at previous AXITF+1 iterations; save final solution at end of current AXITF iteration cycles.
			START = 4.	Save solution at end of a specified crude/fine iteration cycle during a conventional independent run. This option requires additional data, Card 2-A-1.

NOTE: Card 2-A-1 required only for START = 4.

Card 2-A-1	1-10	AXITF2	Crude/fine iteration cycle at which solution is saved during a conventional run. (AXIT+1 < AXITF2 < AXITF)

NOTE: Card 2-A-2 required only for CASE < 0.

Card 2-A-2	1-10	RFSUB	Subsonic relaxation factor (default = 1.5).
	11-20	RFBL	Relaxation factor for boundary layer (default = 0.6).
	21-30	XITBLI	Crude/fine iteration cycle at which boundary layer is initially relaxed (default = 5.0).
	31-40	XITBLF	Frequency of boundary-layer relaxation in crude/fine solution (default = 20.0).
	41-50	XITFBB	Frequency of fine body (pod) boundary value potential update in crude/fine solution (default = 10.0).

(Note: Any variable set = 0.0 is assigned default value.)

CARD NUMBER	CARD COLUMN	VARIABLE NAME	DESCRIPTION
Card 1-W	1-10	ASECT	|ASECT| Number of streamwise sections defining wing planform ($1 \leq$ ASECT ≤ 20).
			SGN (ASECT) Trigger to redefine wing fine grid boundaries
			ASECT $> 0.$ Same as original code, no additional input required on Card 1-W-1.
			ASECT $< 0.$ Read additional data, Card 1-W-1.
	. . .		
	71-80	AQXFG	AQXFG = -1. Code sets 100 fine x-grid points at wing tip station (default).
			AQXFG = 0. Code determines the number of fine x-grid points at wing tip station.
			AQXFG = other. Number of fine x-grid points at wing tip station. ($10. \leq$ AQXFG $\leq 99.$)

NOTE: Card 1-W-1 required only for ASECT $< 0.$

Card 1-W-1	1-10	AWLE	Percent of wing fine grid in front of leading edge (default = 20.).
	11-20	AWTE	Percent of wing fine grid behind trailing edge (default = 10.).
	21-30	AWLS	Percent of wing fine grid below wing (default = 10.).
	31-40	AWUS	Percent of wing fine grid above wing (default = 30.).

(Note: Any variable set = 0.0 is assigned default value.)

CARD NUMBER	CARD COLUMN	VARIABLE NAME	DESCRIPTION
Card 2-W			
	.		
	.		
	.		
	51-60		Field unused.

NOTE: Card 6-W required only for VISMOD < 0.

Card 6-W	1-80	ATRIP	Transition location, x/c, at every wing span station for viscous flow. Specify from inboard to outboard for 18 upper surface values, 18 lower surface values, respectively. (Default values assigned, .05, at all wing span stations.)

APPENDIX C
GENERAL RECOMMENDATIONS FOR CODE USAGE

The computer program described herein has been implemented by a number of investigators. To date, over 75 different configurations (see Table C-1) have been modeled and analyzed. Because of problem three-dimensionality and inherent code flexibility, however, it is impossible to verify the computer program for all of the possible option combinations, shape variations or flow conditions that might be of interest. Despite this, good results should be obtained if the user is aware of the following recommendations.

1. PRACTICE

There are several factors that combine to foil initial attempts by new users performing transonic aircraft analysis. These factors are listed below.

- Complex geometry input/definition
- Complexity/sensitivity of transonic flow fields
- Character of finite-difference relaxation process.

Experience indicates that input and checkout of a complex geometric shape such as a fuselage can be a difficult task when setting up for a subsonic panel code analysis. For transonic analyses, the problem is aggravated further by the complexity of the flow field and sensitivity to what may appear as minor surface irregularities. Experience with subsonic "panel" methodology does not prepare the user for transonic code applications.

The problem is compounded by the nature of finite-difference relaxation processes which require a computational grid system. A surface definition discrepancy may, in addition to causing erroneous computed pressures, result in generation of an improper grid system.

As a result, it is recommended that the user become familiar with the computer code by first analyzing simple shapes such as isolated wings and

AIRFOILS (2-D)
NACA 0012
NASA LS(1)
NASA TRANSPORT AIRFOIL

WINGS
ONERA M-6
RAE 101
NACA WING (RM A9K01)
LOCKHEED/AFOSR (3 CONFIGS)
LTV SKEWED CAMBER WING

ISOLATED BODIES
NACA SHARP NOSE BODY (RM L53H04, 2 CONFIGS)
NASA BLUNT NOSE BODY (TN D-7331)
GRUMMAN GULFSTREAM II FUSELAGE
STORE CALIBRATION BODY
DOUGLAS A-4 FUSELAGE
NIELSEN STORE
EA-6B TAIL POD
NTF 5° CALIBRATION CONE
PATHFINDER I FUSELAGE
NACA BODY OF REVOLUTION (RM A9I26)

WING-BODY/WING-FUSELAGE
GRUMMAN F-14 (3 CONFIGS)
NACA RESEARCH MODEL (RM L51F07)
NASA RESEARCH MODEL (TM X-3431)
GENERAL DYNAMICS F-16
GENERAL DYNAMICS F-111/TACT
LAVI FIGHTER
LTV A-7 SUPERCRITICAL WING CONFIG
DOUGLAS TRANSPORT MODEL
GRUMMAN X-29A FORWARD SWEPT WING DEMONSTRATOR*
BOEING 747-200
BOEING 747-SP
NASA F-8 RESEARCH CONFIG
ROCKWELL HiMAT CANARD DESIGN
NASA USB TRANSPORT
GRUMMAN/AIR FORCE STAC/CDAF CONFIGS
BOEING B-52
NASA TAILOR-MATE (2 CONFIGS)
NASA ENERGY EFFICIENT TRANSPORT
ROCKWELL CANARDED RESEARCH FIGHTER CONFIG.
GRUMMAN ATF-RESEARCH FIGHTER CONFIG
BEECH TRANSPORT
NACA SKEWED WING RESEARCH MODEL (RM A58C03)
NTF-PATHFINDER II FIGHTER

COMPLEX CONFIGURATIONS (NACELLES/PODS, PYLONS, WINGLETS)
SPACE SHUTTLE (LAUNCH CONFIG)
LOCKHEED L-1011
GULFSTREAM AEROSPACE G-III
BOEING KC-135
DOUGLAS WING-BODY-NACELLE-PROP SLIPSTREAM
LOCKHEED C-141
BOEING 767 WINGLET STUDY
DOUGLAS DC-10 WINGLET STUDY (2 CONFIGS)
LOCKHEED C-5A
BOEING 747 WINGLET STUDY
GRUMMAN A-6F PYLON STUDY
GRUMMAN DESIGN 698 TILT-NACELLE V/STOL
FUJI TRAINER (3 CONFIGS)
GRUMMAN VTX WING/WINGLET DESIGN
GRUMMAN E-2 WINGLET STUDY
ARA MODEL M-64 RESEARCH CONFIGURATION
NASA EET NACELLE/PYLON STUDY (2 CONFIGS)
ROCKWELL HIMAT
NTF-PATHFINDER I TRANSPORT
GULFSTREAM AEROSPACE G-IV WING
GRUMMAN DESIGN 623 V/STOL AERO-PROPULSION INTEG STUDY
NASA POD-IN-WING CONFIG
NASA PROP-FAN SIMULATOR

R84-1137-046D

Table C-1 Configurations Analyzed Using Transonic Wing-Body Code

isolated bodies at transonic conditions. Complex aircraft shapes should be attacked after a basic knowledge of 1) the computer code, and 2) the character of transonic flow fields is in hand. Then, when a problem surfaces, the user can determine whether the computer code is at fault, the input data is in error, or the flow condition is unreasonable.

2. NON-POTENTIAL PHENOMENA

In general, most aircraft operate in a low-gradient or "small disturbance" world. Flight efficiency degrades rapidly if disturbances are large. As a result, the present small-disturbance formulation has been found to be applicable to many different configurations over an extraordinary range of flow conditions. The user should be aware, however, that there are many cases for which the code can not be expected to provide a good flow simulation. If geometry and flow conditions combine to produce severe flow gradients, flow separation will occur. If the separation region is large (i.e., ~10% chord on the wing) the computational and physical flows will not agree. In addition, if vortices generated at the wing leading edge or by configuration components interact with surfaces that are of interest, flow predictions will be compromised.

3. DRAG PREDICTION

Consistent prediction of absolute and incremental drag values is not possible with today's 3-D computational methods. This program is not the exception. Some useful incremental drag predictions have been obtained during project applications, but good results have not been obtained with sufficient regularity to recommend usage. In general, the simpler the shape, the higher the probability that drag predictions will be useful.

4. LIFT CONVERGENCE

All of the 3-D computations included in this report were generated using 100 crude grid iterations and 80 cycles in the fine/crude system. Experience indicates that the resulting convergence level is sufficient for most engineering applications. In other words, the accuracy vs cost ratio is high. For some high aspect ratio transport wings, however, this level of convergence may

cause a portion of the wing lift to be lost. One way to compensate for this effect is to analyze the configuration at 1/2 degree greater incidence than that of the experiment. This was done for the C-141 and C-5 comparisons shown in the results section.

For some specialty applications or for cases where computing costs are not a concern, excellent results have been obtained by using 150 crude iterations followed by 150 cycles in the crude/fine system. Other investigators have improved flow simulations by increasing the relaxation factor from $\omega = 1.5$ to $\omega = 1.75$. The new user should begin by using standard cycle/factor values and experiment upward if convergence or comparisons are not satisfactory.

5. WING TIP DIVERGENCE

Analyses performed on highly loaded wings with severe taper and high sweep indicate that occasionally a diverging numerical condition can develop at the wing tip. It occurs only when very strong shock waves form at the wing tip and experience indicates that occurrences are close to conditions for which the flow separates. The numerical condition is caused by improper zones of dependence and/or unfavorable wing tip mesh cell aspect ratios. A rotated difference scheme is now under development. The new scheme eliminates this problem but requires additional refinements and an extensive check-out effort. A simpler "fix" has been achieved by automatically reducing wing tip mesh resolution. This resolution reduction scheme has been automated by computing a "probability of divergence" factor which is based on Mach number, incidence, wing thickness, and planform taper. Occasionally, an application might surface for which the automatic system fails. For these cases, the user can specify the number of fine mesh points at the wing tip (the input variable AQXFG). The highest resolution possible without divergence indicators (pressure "wiggles", increasing $\Delta\phi_{MAX}$) should be sought.

6. COMPARISONS IN HIGH SPANWISE GRADIENT REGIONS

At transonic speeds, flow gradients might be high in the wing spanwise direction. This is particularly noticeable near wing-fuselage junctures, wing-winglet junctures, or mid-wing regions where multiple shock wave sys-

tems coalesce. The computational method predicts chordwise pressure distributions at a number of spanwise locations. These "output" stations may not be aligned with experimental data stations or locations where output is required. Since small span position discrepancies might result in significant pressure differences, some applications may require that output data be interpolated or extrapolated.

On a related matter, it should be noted that the fuselage side is modeled by mesh points positioned along a wing span cut. Depending on the wing/fuselage spacial relationship, the "physical" body side might be as much as 1/2 mesh cell away from the "computational" body side. This presents no problem for most applications, but for some cases where exact juncture pressures are required, and the 1/2 mesh cell shift occurs, the flow simulations may be compromised.

7. GRID GENERATION

The computational method has been developed with the philosophy that engineering users should not have to modify grid systems for most applications. Instead, the systems should be constructed in the same consistent manner for each case. It can be seen by studying the input data format that only the configuration geometry and flow conditions are input. Grid generation has been automated. A knowledgeable user might modify the coordinate systems for special applications, but this requires sufficient familiarity with the coding to make changes to the FORTRAN.

This automated grid philosophy does not guarantee that an "optimum" system will always be generated, particularly for complex configurations with many components. For example, a transport might feature two nacelles positioned below each wing at different heights. The code in its present form is capable of representing only a single height or position for both nacelles. Thus it may be necessary to perform two different analyses to obtain results for each component at its proper position.

An attempt has been made to insure that a nacelle or pod is modeled at its proper distance from the wing by adjusting the grid so that grid points

representing the nacelle centerline are positioned at the requested nacelle location. This does not insure, however, that the computational nacelle wing gap will equal the physical gap. This is an important aspect of many flow simulations. The user should observe what the computational gap is between the points which represent the side of the nacelle facing the wing and the points which represent the wing plane. If this gap is not equal to the physical space between the components, the nacelle height variable should be adjusted until a match is obtained.

8. SUPERCRITICAL AIRFOIL/WING COVE SEPARATION

The boundary layer method incorporated is of the finite difference type which terminates once separation is encountered. The viscous analysis is initiated after an initial inviscid pressure field is generated. For super critical-type sections the initial severe unfavorable pressure gradient found in the cove or lower surface trailing edge region tends to induce a premature separation. A temporary displacement thickness (δ^*) must be "fit" for the cove region to allow the solution process to continue. This fitting process is quite crude and often a true, computed, attached flow boundary layer is never achieved despite the fact that experimental data indicates the flow is attached.

It has also been noted that the code tends to predict supercritical section cove pressures that are higher than experimental values. Predicted wing section lift levels might be several percent too high with an attendant nose down pitching moment increment.

9. SURFACE SHAPE IRREGULARITIES

The present method does not employ conformal mappings for wing sections and no smoothing operation is performed on wing section ordinates which are input. No attempt should be made to "smooth" surface breaks caused by control surface deflections or irregularities resulting from poor manufacturing processes. Experience indicates that the code will simulate the resulting pressure disturbances quite well. For some applications, these predictions will be useful.

10. WINGS WITH STRONG VISCOUS INTERACTIONS

Some applications might feature wing contours for which viscous effects are quite severe. Good agreement can be obtained for these cases, but the total number of iterations may have to be increased by a factor of 3 or 4.

REFERENCES

1. Murman, E. M., and Cole, J. D.: "Calculation of Plane Steady Transonic Flow," AIAA J., vol. 9, Jan. 1971, pp. 114-121.

2. Bailey, F. R.; and Steger, J. L.: "Relaxation Techniques for Three-Dimensional Flow about Wings," AIAA J., vol. 11, Mar. 1973, pp. 318-325.

3. Keller, J. D.; and South, J. C., Jr.: "RAXBOD: A Fortran Program for Inviscid Transonic Flow over Axisymmetric Bodies," NASA TM X-72831, Feb. 1976.

4. Jameson, Antony; and Caughey, D. A.: "A Finite Volume Method for Transonic Potential Flow Calculations." A Collection of Technical Papers - AIAA 3rd Computational Fluid Dynamics Conference, June 1977, pp. 35-54. (Available as AIAA Paper 77-635.)

5. Boppe, C. W.; and Stern, M. A.: "Simulated Transonic Flows for Aircraft with Nacelles, Pylons, and Winglets," AIAA Paper 80-0130, Jan. 1980.

6. Boppe, C. W.: "Transonic Flow Field Analysis for Wing-Fuselage Configurations," NASA CR-3243, May 1980.

7. Hesse, W. J.; and Mumford, N. V. S.: Jet Propulsion for Aerospace Applications, Pitman Corp., NY, 1964, p. 128.

8. Liepmann, H. W.; and Roshko, A.: Elements of Gas Dynamics, John Wiley and Sons, Inc., NY, 1967, p. 53.

9. Freuler, R. J.; and Gregorek, G. M.: "An Evaluation of Four Single Element Airfoil Analytic Methods," Advanced Technology Airfoil Research Conference, NASA CP-2045, vol. I, part 1, Mar. 1978, pp. 133-162.

10. deKuyper, R. E.: "Wind Tunnel Tests of a 1/8.8 Scale Reflection Plane Model of the Grumman Gulfstream III Airplane," CALSPAN Report No. AA-4001-W-26, Nov. 1977.

11. Flechner, S. G.; and Patterson, J. C., Jr.: "Tabulated Pressure Measurements on a Large Subsonic Transport Model Airplane with High-Bypass-Ratio, Powered, Fan-Jet Engines," NASA TM X-2530, May 1972.

12. Montoya, L. C.; Flechner, S. G.; and Jacobs, P. F.: "Effect of Winglets on a First-Generation Jet Transport Wing, II - Pressure and Spanwise Load Distributions for a Semispan Model at High Subsonic Speeds." NASA TN D-8474, July 1977.

1. Report No.	2. Government Accession No.	3. Recipient's Catalog No.
NASA CR-4066		

4. Title and Subtitle	5. Report Date
Aerodynamic Analysis for Aircraft With Nacelles, Pylons, and Winglets at Transonic Speeds	April 1987
	6. Performing Organization Code
7. Author(s)	8. Performing Organization Report No.
Charles W. Boppe	
	10. Work Unit No.
9. Performing Organization Name and Address	11. Contract or Grant No.
Grumman Aerospace Corporation Bethpage, NY 11714	NAS1-14732
	13. Type of Report and Period Covered
12. Sponsoring Agency Name and Address	Contractor Report
National Aeronautics and Space Administration Washington, DC 20546-0001	14. Sponsoring Agency Code 534-02-13-13

15. Supplementary Notes

Langley Technical Monitor: Perry A. Newman
Final Report, Part I

16. Abstract

A computational method has been developed to provide an analysis for complex realistic aircraft configurations at transonic speeds. Wing-fuselage configurations with various combinations of pods, pylons, nacelles, and winglets can be analyzed along with simpler shapes such as airfoils, isolated wings, and isolated bodies. The flexibility required for the treatment of such diverse geometries is obtained by using a multiple nested grid approach in the finite-difference relaxation scheme. Aircraft components (and their grid systems) can be added or removed as required. As a result, the computational method can be used in the same manner as a wind tunnel to study high-speed aerodynamic interference effects. The multiple grid approach also provides high boundary point density/cost ratio. High resolution pressure distributions can be obtained. Computed results are correlated with wind tunnel and flight data using four different transport configurations. Experimental/computational component interference effects are included for cases where data are available. The computer code used for these comparisons is described in the appendices.

17. Key Words (Suggested by Author(s))	18. Distribution Statement
Transonic Flow Computational Aerodynamics Flow Simulations Finite Difference Relaxation Interference Effects	Unclassified—Unlimited Subject Category 02

19. Security Classif. (of this report)	20. Security Classif. (of this page)	21. No. of Pages	22. Price
Unclassified	Unclassified	154	A08

For sale by the National Technical Information Service, Springfield, Virginia 22161

NASA-Langley, 1987